Electron acceleration in relativistic laser-matter interaction

Inaugural-Dissertation

zur

Erlangung des Doktorgrades der
Mathematisch-Naturwissenschaftlichen Fakultät
der Heinrich-Heine-Universität Düsseldorf

vorgelegt von

Vasily Seredov
aus St.Petersburg

Düsseldorf

2008

Printed with permission of the Faculty of Mathematics and Natural Sciences
of Heinrich-Heine University of Duesseldorf

Referee: Prof. Dr. A. Pukhov
Co-referee: Prof. Dr. Georg Pretzler

The day of public defense:

Abstract

The acceleration of charged particles is one of the fundamental problems in high energy physics. The conventional accelerator technology has nearly reached its natural limit because the maximum available electric field is bounded by destruction of the accelerating structures. This fundamental limit on the electric field leads to the monstrous sizes of the modern accelerators. The main advantage of plasma based accelerators is the possibility to increase the electric field and consequently the accelerating rate by several orders of magnitude compared to the conventional technology. One of the most promising ways to employ the plasma acceleration is to use high intensity ultra-short laser pulses to excite the plasma wake field. The physics of relativistic laser plasma is highly nonlinear and requires extensive multi-dimensional computer simulations.

The present work is dedicated mainly to the problem of electron acceleration in the so-called "bubble" regime. The advantage of the bubble regime is the possibility to generate quasi-monoenergetic electron bunches. The bubble regime was first discovered in three dimensional particle-in-cell (PIC) simulations. Recently, it was observed in a number of laser-plasma experiments. One of the central questions in the physics of the bubble is the problem of particle trapping and trajectories of the relativistic electrons during the acceleration stage. Because the bubble structure has not only the longitudinal - accelerating - electric field, but also transverse fields, the electrons runs at curved trajectories and emit strong betatron radiation in x-ray range. The angular distribution of these x-rays allows to draw conclusions on the particle trajectories. In this work, a simplified analytic description of particle trajectories in the bubble fields is suggested. Further, the bubble is simulated using the 3D PIC code VLPL (Virtual Laser Plasma Laboratory). The code VLPL has been further developed to allow individual marking for each particle. Thus, trajectories of individual particles trapped in the bubble can be traced over the full interaction length.

A simulation done for realistic laser-plasma parameters has shown a reasonable agreement between the simplified theory and the simulations. It is shown that in some cases the electron trajectories have the form of a helix around the axis of the laser pulse propagation. In addition, we have stored initial positions of all the trapped particles. This analysis revealed that the electron trapping in the bubble is not steady, but rather contains striations. We have discussed the capture of electrons in the bubble for linear and circular polarization cases. It was shown that the shape of the area of electrons capture directly depends on the laser pulse polarization.

Finally, the new analytic model for an ultra-short laser beam has been developed. Although there is a well-known model for an infinite focused laser pulse, it becomes inexact when applied to an ultra-short laser. The reason is that the ultra-short pulse contains many frequencies. The analytic model has been implemented in the VLPL3D code and used to study dependence of electron acceleration by an ultra-short laser pulse as a function of the focal position in plasma.

Contents

Chapter 1

Introduction

1.1 Overview

The development of the chirped pulse amplification (CPA) [1] technology allows to reach intensities of the laser pulse up to $\sim 10^{21}$ W/cm^2. At these energies the corresponding electric field is $E_f \sim 10^3$ GV/cm. This laser field is much stronger than atomic fields, and in laser matter interaction any material is immediately ionized creating plasma. Then with inevitability any discussion about laser matter interaction comes to laser plasma interaction.

During the propagation of the laser pulse in underdense plasma, electrons are accelerated, wakefields waves are excited, and in some cases a so-called bubble can be formed. The characteristic picture of interaction is the consequence of the correlation of many parameters, particularly, laser pulse intensity, plasma density, plasma frequency, some geometric conditions etc.

Generally at this scale of the pulse intensity electrons gain relativistic energies. Physics of relativistic plasma is highly non-linear and kinetic. Relativistic laser-plasma interactions with short laser pulses lead to important physical phenomena appearing in this regime of high intensity : high acceleration gradient of charged particles, non-linear evolution of the laser pulse and high harmonics generation. These effects are expected to have a great impact on a number of applications in high energy nuclear physics, in material science, ultra fast chemistry, in molecular biology, etc. Particularly accelerated electrons can be very useful for applications in X-ray microscopy, so-called XFEL (x-ray free electrons laser) etc. In most of applications accelerated electrons are used indirectly through synchrotron radiation. As known, charged objects, moving with acceleration, radiates electromagnetic waves, therefore it is simply enough to curve trajectory of these electrons by magnetic fields, for producing radiation in X-ray diapason.

However, the using of laser electric field is not straightforward, as the field is fast oscillating and is perpendicular to the direction of wave propagation. A way to use *longitudinal* plasma waves excited by laser beams to accelerate electrons, was proposed by Tajima and Dawson [4]. When a relativistic intense laser pulse propagates in plasma, ponderomotive force expels plasma electrons from the regions of the largest intensity.

This initiates the plasma oscillations, the *wake field*. Charged particles can be accelerated by the electric field of this plasma wave.

The main advantage of the acceleration of electrons by laser is extremely large acceleration gradients. The natural limit for the amplitude of an electron plasma wave is given by *wavebreaking*. Parameters of *wavebreaking* field has been calculated by Akhiezer and Polovin [5, 6] and is approximately $E_{WB}[\mathrm{V/cm}] \approx 0.96 N_e^{1/2}[\mathrm{cm}^{-3}]$, where N_e is the electron density.

To gain energy from the plasma wave, a highly relativistic electron must move along with the wave at the same speed for increase the time of interaction with this wave. Recently, 3D acceleration mechanisms were proposed, with the advantage in narrow energy spread of accelerated electrons[7].

At present on the grounds of experiments [8, 9, 10, 11, 12, 26]are known three most effective mechanisms of electron acceleration in laser plasma interaction.

- *Plasma Beat-Wave Accelerator* (PBWA)

  The PBWA was the first method, confirmed experimentally, because it can be done using less powerful lasers, than lasers required in other methods. It was proposed in [4] as the alternative of LWFA in the absence of technologies able to provide ultrashort pulses. In PBWA two long laser pulses with two slightly different frequencies are used. The interference ("beating") of these laser beams corresponds to a modulation of the electromagnetic wave envelope, which can act resonant on the plasma.

  If one selects the lasers frequencies ω_1 and ω_2 in such a way, that they satisfy the resonance condition ω_1 - $\omega_2 \approx \omega_p$ where ω_p is the plasma frequency, then a high amplitude plasma wave will be excited.

  The first experimental observation of plasma wave generation using PBWA-method was reported by Clayton et al. [14], and the same group was successful in injected particles acceleration from 2 MeV to 30 MeV, which corresponds to 3 GV/m acceleration gradient [15, 11]. The electrons acceleration to $10MeV$ without injection (from thermal background) was reported in [16].

- *Laser Wakefield Acceleration* (LWFA)

  In this way the plasma waves are excited by a single ultrashort laser pulse. The condition for optimum energy transfer from the pulse to the plasma wave is $L = \lambda_p$ where L is the pulse length and $\lambda_p = 2\pi c/\omega_p$ is the plasma wavelength, and $\omega_p = \sqrt{4\pi N_e e^2/m}$ is the plasma frequency. The LWFA was proposed by Tajima and Dawson [4]. However this experimental demonstration required high laser intensity with subpicosecond pulse lengths. The first evidences of plasma wave excitation via LWFA mechanism were reported in [17, 18], and accelerated electrons were first observed in [27].

- *Self-modulated LWFA* (SM-LWFA)

In the self-modulated LWFA regime, an initially long laser pulse, $L > \lambda_p$, breaks on a series of short pulses [12, 26]. This break is caused by the forward Raman scattering (FRS) and the so-called "sausaging" of the pulse envelope [20, 21, 22, 23]. The FRS instability can grow from the noise. Density perturbations are caused by the group velocity variations, which lead to a longitudinal bunching of the pulse. In that way the pulse is dividing on a series of short pulses, with the characteristic length $\sim \pi c/\omega_p$. Each of these small pulses can be considered as an individual plasma wave driver (and it satisfies with resonant condition). Such pulse self-modulation allows to use higher plasma densities, than the standard LWFA.

The first experimental evidence of the self-modulated LWFA has been given in the work [24], where FRS forward scattering and the electrons acceleration up to 2 MeV were observed. The possibility of electrons acceleration was demonstrated in the series of experiments [12, 26, 25]. In [26] the observation of background electrons acceleration to 30 MeV was reported.

There is a significant physical difference between these three regimes of the wake field acceleration. The SM-LWFA relies on an instability (the stimulated forward Raman scattering) for an efficient plasma wave excitation. The PBFA regime also employes a long laser pulse that is subject of Raman instabilities. In the LWFA regime, however, the laser pulse is shorter than the plasma period and thus is free from any Raman instability. It is expected that the LWFA regime will finally lead to a practically useful plasma-based accelerator.

However, to use the LWFA regime, one needs a very short and relativistically powerful laser pulse. It appears that relativistic plasma itself can be considered as a nonlinear medium suitable for laser pulse compression and short pulse generation.

1.2 Electrons in electromagnetic wave

1.2.1 Plane wave case

We start with some basic definition of the light field, dimensionless amplitude a with relativistic threshold of intensity $a = 1$. A plane light wave can be described by follow vector potential

$$\mathbf{A}(\mathbf{r}, t) = \mathrm{Re}\left\{\mathbf{A_0} \exp i\psi\right\} \ , \tag{1.1}$$

where $\mathbf{r}$ and t is the space and time coordinate, the laser amplitude $\mathbf{A_0} = A_0(\hat{e}_y \pm \hat{e}_z)$ for circular polarization with + and - for right- and left-circular polarization correspondingly, and $\mathbf{A_0} = A_0\hat{e}_y$ for linear polarization, $\psi = \mathbf{kr} - \omega t$ is the phase. The dispersion relation in vacuum is

$$\omega = kc \ , \tag{1.2}$$

where $k = |\mathbf{k}| = 2\pi/\lambda$, where $\lambda = cT = 2\pi c/\omega$ and c is the speed of light. Using the standard *Coulomb gauge*

$$\text{div } \mathbf{A} = 0 \ . \tag{1.3}$$

The expressions for electric field $\mathbf{E}$ and magnetic field $\mathbf{B}$ take the form

$$\mathbf{E} = -\frac{1}{c}\frac{\partial \mathbf{A}}{\partial t} \ , \tag{1.4}$$

$$\mathbf{B} = \text{rot } \mathbf{A} \ . \tag{1.5}$$

Using the substitution rules for derivatives: $\partial/\partial t \to -i\omega t$, $\partial/\partial \mathbf{r} \to i\mathbf{k}$, they can be rewritten as

$$\mathbf{E} = \text{Re}\left\{\frac{i\omega}{c}\mathbf{A_0}e^{i\psi}\right\} \ , \tag{1.6}$$

$$\mathbf{B} = \text{Re}\left\{i\mathbf{k} \times \mathbf{A_0}e^{i\psi}\right\} \ . \tag{1.7}$$

Calculating Poynting vector

$$\mathbf{S} = \frac{c}{4\pi}\mathbf{E} \times \mathbf{B} \ , \tag{1.8}$$

one obtains the formula for intensity of the light:

$$I(\psi) = |\mathbf{S}| = \frac{\omega k}{8\pi}A_0^2(1 - \cos 2\psi) \qquad \text{for linear polarization} \tag{1.9}$$

and

$$I(\psi) = |\mathbf{S}| = \frac{\omega k}{4\pi}A_0^2 \qquad \text{for circular polarization,} \tag{1.10}$$

what can be written in the form

$$I(\psi) = |\mathbf{S}| = \frac{\omega k}{8\pi}A_0^2 \cdot \zeta \tag{1.11}$$

where

$$\zeta = \begin{cases} (1 - \cos 2\psi) & \text{for linear polarization ,} \\ 2 & \text{for circular polarization .} \end{cases} \tag{1.12}$$

When the phase ψ is changed on 2π, the intensity for linear polarization oscillates twice, but it does not depend on phase for circular polarization. For practical reasons one usually introduce the intensity averaged over phase:

$$I = \frac{1}{2\pi}\int_0^{2\pi} I(\psi)d\psi = \bar{\zeta} \cdot \frac{\omega k}{8\pi}A_0^2 \ . \tag{1.13}$$

The factor $\bar{\zeta}$ is different for linear polarization and circular polarization:

$$\bar{\zeta} = \begin{cases} 1 & \text{for LP ,} \\ 2 & \text{for CP .} \end{cases} \tag{1.14}$$

Using Eq. (1.13) and the expression for wave vector, the averaged intensity can be written as

$$I\lambda^2 = \bar{\zeta} \cdot \frac{\omega k \lambda^2}{8\pi} A_0^2 = \bar{\zeta} \cdot \frac{\pi}{2} c A_0^2 \ . \tag{1.15}$$

Also for particles of selected specie with known mass m and charge q, let we introduce the *relativistic normalized vector potential*

$$\boldsymbol{a} = \frac{q\mathbf{A}}{mc^2} \ . \tag{1.16}$$

The *dimensionless amplitude* is

$$a_0 = |\boldsymbol{a}_0| = \frac{|q| A_0}{mc^2} \ . \tag{1.17}$$

Using this notation we can rewrite Eq. (1.15) as:

$$I\lambda^2 = \bar{\zeta} \cdot \frac{\pi}{2} \frac{m^2 c^5}{q^2} a_0^2 \ . \tag{1.18}$$

The amplitudes of electric and magnetic fields are correspondingly:

$$E_0 = \frac{mc\omega}{|q|} a_0 \ , \quad B_0 = \frac{mc\omega}{|q|} a_0 \ . \tag{1.19}$$

For electrons: $q = -e$, $m = m_e$ and we have:

$$a_0 = \frac{eA_0}{m_e c^2} \ , \tag{1.20}$$

$$I_0 \lambda^2 = \bar{\zeta} \cdot \left[1.37 \times 10^{18} \frac{W}{cm^2} \mu m^2 \right] a_0^2 \ . \tag{1.21}$$

1.2.2 Relativistic electrons case

Initially let us consider relativistic invariants in the electrons motion in plane wave. The Lagrange function of particle with the mass m and the charge q in prescribed electromagnetic field with potential ϕ and vector-potential $\mathbf{A}$ is

$$L(\mathbf{r}, \mathbf{v}, t) = -mc^2 \sqrt{1 - \frac{v^2}{c^2}} + \frac{q}{c} \mathbf{v} \cdot \mathbf{A} - q\phi \ . \tag{1.22}$$

Using the Euler-Lagrange equation

$$\frac{d}{dt} \frac{\partial L}{\partial \mathbf{v}} - \frac{\partial L}{\partial \mathbf{r}} = 0 \ , \tag{1.23}$$

we obtain the relativistic equation of motion for the particle

$$m \frac{d\mathbf{p}}{dt} = q \left(\mathbf{E} + \frac{\mathbf{v}}{c} \times \mathbf{B} \right) \ . \tag{1.24}$$

Where $\mathbf{p} = \gamma m \mathbf{v}$, is the particle momentum and gamma-factor is given by formula

$$\gamma = \frac{1}{\sqrt{1 - v^2/c^2}} \ . \tag{1.25}$$

The canonical momentum

$$\mathbf{p}^{can} = \frac{\partial L}{\partial \mathbf{v}} = m\gamma\mathbf{v} + \frac{q\mathbf{A}}{c} = \mathbf{p} + \frac{q}{c}\mathbf{A} = m(\gamma\mathbf{v} + c\boldsymbol{a}) \ . \tag{1.26}$$

For a plane light wave, there are exist two symmetry which provide two constants of motion. Planar symmetry implies $\partial L/\partial \mathbf{r}_\perp = 0$ and therefore the conservation of canonical momentum in transverse direction

$$\partial L/\partial \mathbf{v} = \mathbf{p}_\perp + \frac{q}{c}\mathbf{A}_\perp = const \ . \tag{1.27}$$

Second invariant derives from the wave form of $\mathbf{A}(t - x/c)$, means the laser pulse propagates with the constant velocity v_{ph} which in vacuum is equival to c. Making use the relation $dH/dt = -\partial L/\partial t$ for the Hamilton function $H(\mathbf{x}, \mathbf{p}, t) = E(t)$ (e.g. Landau, Lifshitz, 1964), which express time-dependent energy of the particle, one obtains

$$\frac{dE}{dt} = -\frac{\partial L}{\partial t} = v_{ph}\frac{\partial L}{\partial x} = v_{ph}\frac{d}{dt}\frac{\partial L}{\partial v_x} = v_{ph}\frac{dp_x^{can}}{dt} = v_{ph}\frac{dp_x}{dt} \ , \tag{1.28}$$

taking into account that $A_x = 0$ for plane light wave. From this we obtain second invariant

$$E - v_{ph}p_x = const \ . \tag{1.29}$$

Then for electrons initially at rest the kinetic energy is

$$E_{kin} = E - mc^2 = v_{ph}p_x \ . \tag{1.30}$$

In combination with $E = mc^2\gamma = \sqrt{(mc^2)^2 + p_\perp^2 c^2 + p_x^2 c^2}$, this leads to

$$E_{kin} = \frac{p_\perp^2}{2m} = p_x c = mc^2(\gamma - 1) \ . \tag{1.31}$$

From Eq. (1.27) we have

$$\mathbf{p}_\perp = -\frac{q}{c}\mathbf{A}_\perp = -mc\mathbf{a}_\perp \ , \tag{1.32}$$

and finally kinetic energy in terms of relativistic normalized vector potential

$$E_{kin} = \frac{p_\perp^2}{2m} = \frac{a^2}{2}mc^2 \ . \tag{1.33}$$

From Eq. (1.33) we can see that $E_{kin} \sim mc^2$ for $a_0 \sim 1$. The intensity I_0 which corresponds to $a_0 = 1$ usually is considered as a relativistic threshold for specified sort of particles. If we consider the motion of electrons, the amplitude $a_0 = 1$ corresponds to the laser intensity

$$I_0\lambda^2 = 1.37 \times 10^{18} W cm^{-2} \mu m^2. \tag{1.34}$$

1.2.3 Trajectory of relativistic particles in plane wave

For an electron in a plane light wave of the finite duration, relativistic equation of motion can be integrated exactly. For an electron initially at rest, the constants of motion give

$$\mathbf{a} = \frac{e\mathbf{A}_\perp}{mc^2} \ , \tag{1.35}$$

$$\hat{\mathbf{p}}_\perp = \frac{\mathbf{p}_\perp}{mc} = \mathbf{a} = (0, a_y, a_z) \ , \tag{1.36}$$

$$\hat{E}_{kin} = \frac{E_{kin}}{mc^2} = \gamma - 1 = \hat{p}_x = \frac{\hat{p}_\perp^2}{2} = \frac{a^2}{2} \ . \tag{1.37}$$

An immediate and very important observation at this point is that E_{kin} is directly coupled to the light amplitude a and falls back to zero as soon as the electron leaves the light field. The electron cannot gain net energy in a plane light wave. It needs breaking of planar symmetry for net energy gain. This typically occurs in experimental configuration, e.g. due to finite beam radius or additional interactions.

From Eq. (1.35) we obtain the equations of motion

$$\hat{p}_x = \gamma\beta_x = \frac{\gamma}{c}\frac{dx}{dt} = a^2/2 \ , \tag{1.38}$$

$$\hat{p}_y = \gamma\beta_y = \frac{\gamma}{c}\frac{dy}{dt} = a_y \ \ , \tag{1.39}$$

$$\hat{p}_z = \gamma\beta_z = \frac{\gamma}{c}\frac{dz}{dt} = a_z \ . \tag{1.40}$$

Since $\gamma = 1 + a^2/2$, we obtain for $a \gg 1$

$$\beta_x = \tfrac{a^2/2}{1+a^2/2} \to 1, \beta_y = \tfrac{a_y}{1+a^2/2} \to 0, \beta_z = \tfrac{a_z}{1+a^2/2} \to 0,$$

and also $\tan\theta = p_\perp/p_\parallel \to 0$. This means that the electron, though oscillating transversely for low field srength $|\mathbf{a}| \ll 1$, moves more and more in the direction of light propagation for relativistic laser intensity with $|\mathbf{a}| \gg 1$.

Integration Eq. (1.38) for a given light pulse $\mathbf{a}(t - x/c)$ is straightforward in the variable $\tau = t - x(t)/c$, for which

$$\gamma\tfrac{d}{dt} = \gamma\tfrac{d\tau}{dt}\tfrac{d}{d\tau} = \gamma(1 - \tfrac{1}{c}\tfrac{dx}{d\tau})\tfrac{d}{d\tau} = (1 + \tfrac{a^2}{2} - \tfrac{a^2}{2})\tfrac{d}{d\tau} = \tfrac{d}{d\tau},$$

and therefore $d\tau = dt/\gamma$, such that the equations of motion obtain the simple form

$$\frac{dx}{d\tau} = c\frac{a^2}{2} \ , \tag{1.41}$$

$$\frac{dy}{d\tau} = ca_y \ , \tag{1.42}$$

$$\frac{dz}{d\tau} = ca_z \ . \tag{1.43}$$

For circular polarization with

$$\mathbf{a}(\mathbf{r},t) = \mathrm{Re}\left\{a_0(\hat{e}_y \pm \hat{e}_z)e^{-i\omega t}\right\}$$

the electron motion is of particular simplicity. Since $a^2 = a_y^2 + a_z^2 = a_0^2/2, \gamma = 1 + a_0^2/2$ and therefore $E_{kin} = a_0^2/2$ depends on time only through the envelope function $a_0(\tau)$, but not through the rapidly oscillating phase $\psi = -\omega\tau$ of the laser pulse. For constant a_0, we obtain from Eq. (1.41) with $\tau = t/\gamma$ the trajectory

$$x(t) = \left(ca_0^2/2\right)\tau = \frac{a_0^2/2}{1 + a_0^2/2}ct \ , \tag{1.44}$$

$$y(t) = \frac{ca_0}{\omega}\sin\left(\omega t/\gamma\right) \ , \tag{1.45}$$

$$z(t) = \mp\frac{ca_0}{\omega}\cos\left(\omega t/\gamma\right) \ ; \tag{1.46}$$

it describes an electron moving with constant speed on a helix.

For linear polarization, electron motion is more complex. Considering a box-shaped pulse with $a_y = a_0\cos(\omega t)$ for $0 < \tau < N(2\pi/\omega)$, $a_z \equiv 0$, $a^2 = a_y^2 = a_0^2\cos^2(\omega\tau)$ and an electron initially at rest and located at $x = y = z = 0$, the trajectories obtained in the form

$$x(t) = \frac{ca_0^2}{2}\int_0^\tau \cos^2\left(\omega\tilde{\tau}\right)d\tilde{\tau} = \frac{ca_0^2}{4}\left[\tau + \frac{1}{2\omega}\sin\left(2\omega\tau\right)\right] \ , \tag{1.47}$$

$$y(t) = ca_0\int_0^\tau \cos\left(\omega\tilde{\tau}\right)d\tilde{\tau} = \frac{ca_0}{\omega}\sin\left(\omega\tau\right) \ , \tag{1.48}$$

where parameter τ is determined implicitly by $\tau = t - x(t)/c$. Apparently, the motion consists of an overall drift in x-direction:

$$x_d(t) = \frac{a_0^2}{a_0^2 + 4}ct \ , \tag{1.49}$$

and superimposed a figure-8 trajectory in the drift frame:

$$ky = a_0\sin\left(\omega\tau\right), k(x - x_d) = \frac{a_0}{8}\sin\left(2\omega\tau\right) \ . \tag{1.50}$$

The self-similar electron trajectory shows that the transverse oscillation amplitude is proportional to the laser amplitude a_0, while the longitudinal scale is proportional to a_0^2. Thus, with small amplitude $a_0 \ll 1$, the electron moves mainly in transverse direction, while for relativistic amplitudes $a_0 \gg 1$, the motion occurs predominantly in

laser direction. It should be understood that the electron can gain energy from laser field only through the transverse electric field and that the role of magnetic $\mathbf{v} \times \mathbf{B}$ force consist in the turning the orbit into forward direction without adding energy.

1.2.4 Non-plane electromagnetic waves

As it is well known, if relativistic particle is interacting with infinite electromagnetic wave in vacuum, if one neglects non-linear effect, the total particle acceleration is null (Lawson-Woodward theorem [28, 29]).

In real experiments the laser pulse cannot be described by plane wave by the reason that it is focused. But at a first approximation we can use relations obtained above even for a finite laser beam. Using Eq. (1.31), (1.33) we can estimate the scattering angle for a single electron outgoing from the laser focus:

$$\tan^2\theta = \frac{p_\perp^2}{p_\parallel^2} = \frac{2}{\gamma - 1} \ . \tag{1.51}$$

This result has been verified experimentally in [30].

For the next oder of approximation, near the focal plane we can write:

$$\mathbf{A} = \mathbf{A}(\psi_g, \mathbf{r}) \exp(k\psi_{ph}) \ , \tag{1.52}$$

where

$$\psi_{ph} = z - v_{ph}t \ , \quad \psi_{gr} = z - v_{gr}t \ . \tag{1.53}$$

The phase velocity $v_{ph} > c$ and the group velocity $v_{gr} < c$. Using the Coulomb gauge condition Eq. (1.3), we can conclude, that focused electromagnetic wave has the longitudinal component $\mathbf{A}_\parallel$:

$$\partial_z A_z = -\nabla_\perp \mathbf{A}_\perp \ . \tag{1.54}$$

There is no exact analytical theory for particles motion in the focused pulse. But if we suppose that the wave amplitude varies slowly respectively to the phase averaged over fast oscillations it can be performed. If we consider particle momentum, averaged over laser period $\bar{\mathbf{p}}$ for low intensity $a \ll 1$, the *relativistic ponderomotive force* can be introduced:

$$\mathbf{f}_{pond} = \frac{d\bar{\mathbf{p}}}{dt} = -mc\nabla\frac{\bar{a}^2}{2} \ , \tag{1.55}$$

(see for details [31]).

From Eq. (1.55) we can see that particles should be expelled from the region of high intensity. One can also observe that the relativistic ponderomotive force is proportional to $\propto \nabla\bar{a}^2/2$ and does not depends from the laser polarization. In [32, 33] it was shown that the relativistic ponderomotive force model is still valid even for higher a and Eq. (1.55) takes the form:

$$\frac{d\bar{\mathbf{p}}}{dt} = -\frac{mc^2}{\bar{\gamma}}\nabla\bar{\gamma} \ . \tag{1.56}$$

In [33] it was shown that the scattering picture depends on dimensionless parameter $\alpha = k\sigma/(1 - v_z/c)$. If $\alpha \ll 1$ the scattering is ponderomotive. If $\alpha > 1$ the particle motion is more complicated and polarization asymmetries appear.

Also the laser pulse can be described as pulsed Gaussian beam. Let we start the considering with a light beam of the form

$$\mathbf{a}(\mathbf{r}, t) = \mathrm{Re}\left\{\mathbf{a_0}(\mathbf{r}, t) \exp\left[i(\mathbf{kr} - \omega t)\right]\right\} \ , \tag{1.57}$$

and let us assume that the amplitude $\mathbf{a_0}(\mathbf{r}, t)$ varies much less with $\mathbf{r}$ and t than the phase factor, i.e.

$$|\partial a_0/\partial t| \ll |\omega a_0|, \quad |\partial a_0/\partial z| \ll |k a_0| \ . \tag{1.58}$$

The wave equation in vacuum $(\nabla^2 - (1/c^2)\partial^2/\partial t^2)\mathbf{a} = 0$ can then be reduced to the envelope equation

$$(\nabla_\perp^2 + 2ik\partial/\partial z)a_0(r, z) = 0 \ , \tag{1.59}$$

where we have neglected second derivative relative to first derivative terms and have used the dispersion relation $\omega^2 = k^2c^2$. Also we have restricted ourselves to an infinitely long, cylindrical beam. The radial coordinate is r with $\nabla_\perp^2 = \partial^2/\partial r^2 + (1/r)\partial/\partial r$, and the axial coordinate z is chosen to comove with the pulse such that the envelope function is independent of time.

For a Gaussian beam with $a_0(r, z) = \exp\left(P(z) - Q(z)(r/r_0)^2\right)$ it is straightforward to derive the functions $P(z)$ and $Q(z)$ satisfying the envelope equation, and one obtains

$$a_0(r, z) = \frac{e^{-r^2/(r_0^2(1+z^2/L_r^2))}}{\sqrt{1 + z^2/L_r^2}} \exp\left\{-i \arctan\left(\frac{z}{L_r}\right) + i\left(\frac{r}{r_0}\right)^2 \frac{z/L_r}{1 + z^2/L_r^2}\right\} \ . \tag{1.60}$$

Here the front factor describes a hyperbolic envelope, where r_0 is the focus radius at $z = 0$ and $L_r = kr_0^2/2$ is the Rayleigh length, determining the length of the focal waist. The phase factor describes spherical phase fronts of the incoming and outgoing wave with a phase jump of π when passing focus.

1.3 Waves in plasma

1.3.1 Electromagnetic waves in plasma

The interaction of very intensive laser pulses with dense matter is a much more complicated problem than the interaction with single particles. At the intensity of $10^18 W/cm^2$ and more, the material ionized within one laser cycle, and a dense electron plasma formed which interacts collectively with the laser fields. The time scale of the electron dynamics is set by the plasma frequency

$$\omega_p^2 = 4\pi e^2 N_0/m \ , \tag{1.61}$$

which is comparable to frequency of light, while ions are almost static because of their higher mass and can be viewed as a uniform background with charge density $ZN_i = N_0$. To the extent that the light can penetrate the plasma, all plasma electrons acquire relativistic energies and as a consequence collision cross-section become negligible, at least during the subpicosecond interaction times. Plasma interactions then occur exclusively through E and B filds, those of the laser light, but also huge plasma field generated due to charge separation and laser-driven electric currents. Thermal pressure forces then can be neglected compared to ponderomotive forces, and this leads to the *cold plasma* approximation.

The *cold plasma* equations describe the plasma essentially as zero temperature electron fluid for which density $N(\mathbf{r}, t)$ and velocity $\mathbf{u}(\mathbf{r}, t)$ are functions of space and time. The current density is given by $\mathbf{J} = -eN\mathbf{u} = -eN\mathbf{P}/m\gamma$, where $\mathbf{P} = m\gamma\mathbf{u}$ is the momentum and $\gamma = \sqrt{1+p^2}$ the relativistic factor. Here and following, we use dimensionless variables:

$$\mathbf{a} = \frac{e\mathbf{A}}{mc^2}, \quad \varphi = \frac{e\phi}{mc^2}, \quad \mathbf{p} = \frac{\mathbf{P}}{mc}, \quad n = \frac{N}{N_0} \ . \tag{1.62}$$

The wave equation describing the light propagation in plasma is then obtained from Maxwell's equations in the form

$$\begin{gathered} \nabla^2\mathbf{a} - (1/c^2)\partial^2\mathbf{a}/\partial t^2 = (1/c)\partial\nabla\varphi/\partial t + (\omega_p^2/c^2)n\mathbf{p}/\gamma \ , \\ \nabla^2\varphi = (\omega_p^2/c^2)(n-1) \ . \end{gathered} \tag{1.63}$$

Here the source terms on the right-hand side consist of time-dependent space charge fields, expressed by the electrostatic potential φ and currents. The equation of motion for cold plasma is taken as

$$\frac{d}{dt}\mathbf{P}(\mathbf{r}, t) = -e(\mathbf{E} + \frac{\mathbf{u}}{c} \times \mathbf{B}) \ , \tag{1.64}$$

where pressure terms proportional to plasma temperature are neglected. With

$$\mathbf{B} = \nabla \times \mathbf{A} \ , \tag{1.65}$$

$$\mathbf{E} = -\nabla\phi - (1/c)\partial\mathbf{A}/\partial t \ . \tag{1.66}$$

the Coloumb gauge $\nabla \cdot \mathbf{A} = 0$ and the time derivative $d/dt = \partial/\partial t + \mathbf{u} \cdot \nabla$, we find from Eq. (1.64)

$$\left(\frac{\partial}{\partial t} + \mathbf{u} \cdot \nabla\right)\mathbf{P} = -e\left[-\frac{1}{c}\frac{\partial\mathbf{A}}{\partial t} - \nabla\phi + \frac{\mathbf{u}}{c} \times (\nabla \times \mathbf{A})\right] \ . \tag{1.67}$$

Switching to dimensionless variables and making use of the relations

$$\nabla\gamma = \nabla\sqrt{1+p^2} = \frac{1}{2\gamma}\nabla p^2 \ , \tag{1.68}$$

and

$$\mathbf{u} \times \nabla \times \mathbf{p} = \nabla_{\to p}(\mathbf{u} \cdot \mathbf{p}) - (\mathbf{u} \cdot \nabla)\mathbf{p} = c\nabla\gamma - (\mathbf{u} \cdot \nabla)\mathbf{p} \ , \tag{1.69}$$

where $\nabla_{\to p}$ operates only on $\mathbf{p}$, we finally obtain the central relativistic equation of motion

$$\frac{1}{c}\frac{\partial}{\partial t}(\mathbf{p} - \mathbf{a}) - \mathbf{u} \times \nabla \times (\mathbf{p} - \mathbf{a}) = \nabla(\varphi - \gamma) \ . \tag{1.70}$$

A basic solution is $\mathbf{p} = \mathbf{a}$, for which $\nabla(\varphi - \phi) = 0$. In this case the electrostatic force $\nabla\varphi$ just balances the ponderomotive force $\nabla\gamma = \nabla\sqrt{1+p^2} = \nabla\sqrt{1+a^2} = (2\gamma)^{-1}\nabla a^2$. For example, it describes how plasma electrons are pushed forward in the front of a laser pulse exiting plasma waves or the pressure equilibrium in a self-focused laser channel in which the ponderomotive force expels electrons building up a radial electrostatic field. The creation of strong electrostatic fields of same order as the laser electric field is a key feature of relativistic laser plasma interaction. These electrostatic fields accelerate electrons and in particular ions to multi-MeV energies. It is convinient to consider circular polarized light beams

$$\mathbf{a} = \mathrm{Re}\left\{(\hat{e}_x \pm \hat{e}_y)a_0(r,z,t)e^{-i\psi}\right\}$$

with $r = \sqrt{x^2+y^2}, \psi = kz - \omega t$, and $|\mathbf{a^2}| = a_0^2(r,z,t)$, varying slowly in time and space. Under these conditions and $\mathbf{p} = \mathbf{a}$, also $\gamma = \sqrt{1+p^2} = \sqrt{1+a_0^2}$ and φ vary slowly in space and time, just as the envelope function a_0^2. In this case, the wave equation Eq. (1.63) can be written in the form

$$\nabla^2\mathbf{a} - \frac{1}{c}\frac{\partial^2\mathbf{a}}{\partial t^2} = \frac{\omega_p^2}{c^2}\frac{n\mathbf{a}}{\gamma} \ . \tag{1.71}$$

1.3.2 Instabilities

The main quantity, which defines the time scale for plasma processes is the plasma frequency. The natural oscillation frequency of the electron plasma is the *electron plasma frequency*

$$\omega_{pe} = \sqrt{\frac{4\pi e^2 N_e}{m_e}} \ , \tag{1.72}$$

As the electrons are the lightest particles in the plasma we will mainly use this frequency and call it sometimes the *plasma frequency* $\omega_p = \omega_{pe}$. Usually in relativistic case we have the mass correction: $m_e \to m_e\langle\gamma\rangle$, where $\langle\gamma\rangle$ is the relativistic gamma-factor, averaged locally over mainly electrons.

From the dispersion relation

$$\omega^2 = \omega_p^2 + k^2c^2 \tag{1.73}$$

is easy to see that with condition $\omega < \omega_p$ we have imaginary wave vector, so the laser pulse can not propagates in the plasma. The liminal frequency value $\omega = \omega_p$ defines the

maximum plasma density, through which pulse with specified frequency can penetrate. It is *critical plasma density*, which given by formula

$$N_{cr} = \frac{m_e \omega^2}{4\pi e^2} \ . \tag{1.74}$$

Plasma can be considered as a medium with the refraction index

$$\eta = \sqrt{\varepsilon} = \sqrt{1 - \frac{N_e}{N_{cr} \langle \gamma \rangle}} \ , \tag{1.75}$$

where N_{cr} is defined by Eq. (1.74). From Eq. (1.75) we can see that the threshold for plasma non-transparency is $N \sim \langle \gamma \rangle N_{cr}$. At relativistic intensities $\langle \gamma \rangle$ depends on the local intensity I (approximately $\langle \gamma \rangle \sim I^{1/2}$), and a bunch of non-linear optics effects appears. This dependence of plasma frequency on γ and through it on the laser radiation intensity has deep consequences for light propagation in plasma.

The condition of electromagnetic wave passing through the plasma is that the wave length of the wave vector k is the real number. Using Eq. (1.73), it can be rewritten as $\omega > \omega_p$.

When an ultra-relativistically intense laser pulse propagates in plasma, we can use for the locally averaged electrons γ-factor the estimation:

$$< \gamma > \sim \frac{a_0}{2} \ , \tag{1.76}$$

([34]). Using this equation one can easily obtain the condition of relativistic transparency

$$a > 2 \frac{N_e}{N_{cr}} \ . \tag{1.77}$$

The first results in nonlinear plasma optics were obtained from the identification of so-called parametric instabilities. They were investigated in terms of wave-wave interactions, when an incident electromagnetic wave with frequency ω_0 decays into two sidebands: the Stokes wave with the frequency $\omega_0 - \omega_{mod}$ and the anti-Stokes one with the frequency $\omega_0 + \omega_{mod}$. The frequency ω_{mod} corresponds to the modulation of refraction index. This technique was first applied in the papers [36, 37, 38]. Using this formalism, various instabilities were investigated, including Brillouin and Raman scattering, Compton scattering, filamentation/self-focusing and self-phase modulational instabilities [39, 36, 37, 38, 40, 41].

The most important instabilities for a short laser pulse interaction with plasma are:

FRS Forward Raman scattering ($\omega_{mod} = \omega_{pe}$)

SF Relativistic self-focusing / filamentation ($\omega_{mod} \ll \omega_{pe}$)

SPM Relativistic self-phase modulation ($\omega_{mod} \ll \omega_{pe}$).

An alternative formalism to consider the instability was proposed in [42, 43, 44]. In these papers, modulations of the laser intensity were considered in terms of physical phenomena, which appear from modulations of the refraction index. The index of refraction (as well as the group and phase velocities) can be altered by modulations of (i) plasma density N, (ii) laser amplitude a, (iii) laser frequency ω_0. Therefore, the index of refraction may be expanded on this three perturbations

$$\eta = 1 - \frac{1}{2}\left(1 + \frac{\delta N_e}{N_e} - \frac{\langle a^2 \rangle}{2} - 2\frac{\delta\omega_0}{\omega_0}\right) \ , \tag{1.78}$$

(see for details [34, 35]).

From the equation for conservation of the photons number

$$\langle a^2 \rangle \omega_0 r^2 L = const \ , \tag{1.79}$$

where r is the laser spot size, L is initial length of longitudinal pulse, and $\langle a^2 \rangle$ is the square of dimensionless amplitude(the laser intensity), which is averaged over fast oscillations. We can see that laser intensity can be modulated by changes in

- L, e.g., due to the longitudinal bunching
- r, due to the transverse focusing
- ω_0, due to the photon acceleration

Let us consider the laser beam propagation in underdense plasma. Two key mechanisms responsible for *relativistic self-focusing* exist. The first one is the *relativistic mass increase* of plasma electrons, which cause plasma frequency decrease according to $\omega_p^{rel} \sim \langle \gamma \rangle^{-1}$. The second mechanism is the *electrons expelling* out of the focal spot by ponderomotive force push. Such electrons expulsion from the pulse region diminishes the local electrons frequency N_e and therefore the local plasma frequency. As a result of such local decrease of the plasma frequency we have the increasing of the plasma refraction index, and the plasma acts as a positive lens. The process of relativistic self-focusing was investigated theoretically in [37, 45, 3, 47] and experimentally in [48, 49].

Let us first consider $a < 1$. If we investigate low-intensity laser beam $a \ll 1$, the plasma density can be considered as undisturbed $N_e \approx N_0$, and electrons can be treated as non-relativistic particles with $\gamma \approx 1$. With the amplitude increasing, first gamma-nonlinearity appears, $\gamma \approx 1 + a^2/4$, while the density perturbations contribute in the higher oder. Then the wave equation in envelope approximation can be used

$$\left(\nabla_\perp^2 + 2ik\frac{\partial}{\partial x}\right) a = -\frac{\omega_p^2}{c^2}\frac{|a|^2}{4}a \ . \tag{1.80}$$

The term $\nabla_\perp^2 a$ disperses the beam, the term $\omega_p^2 |a|^2 a/(4c^2)$ compresses it and at the threshold intensity they should balance each other. For Gaussian envelope approximation $a(r,z) \sim a_0(z)\exp(-r^2/R^2(z))$ the critical power is given by formula

$$P_{cr} = 2\left(\frac{\omega}{\omega_p}\right)^2 P_0 \text{ where } P_0 = \frac{m_e^2 c^5}{e^2} = 8.7 \text{ GW} \ , \tag{1.81}$$

One should note, that then the power approaches to P_{cr}, contraction of the beam leads to the increase of light intensity on the axis and ponderomotive expulsion of the electrons. This leads to plasma channel formation with reduced electron density. Numerical investigations performed in paper [45] give approximately the same value for self-focusing threshold

$$P_{cr} \approx 17 \left(\frac{\omega}{\omega_p}\right)^2 \text{GW} \ . \tag{1.82}$$

From this value the laser pulse becomes relativistically focused. An analysis in envelope approximation, which was performed in [46], shows that the picture of self-focusing depends on laser pulse and plasma parameters. The first possibility is that the self-focusing of the whole laser pulse leads to single channel production. But if the laser power exceeds the value P_{cr} by a few oder of magnitude, instead of single channel, the multiple channels can be produced. This effect is known as the relativistic filamentation([46]).

Let us consider now theory of self-focusing at $a > 1$. The Lorentz force $(e/c)\mathbf{v} \times \mathbf{B}$ drives the electrons forward in the pulse propagation direction. In this regime the radiation drives currents of relativistic electrons in the direction of pulse propagation. This currents create a strong magnetic field, which significantly change the picture of pulse interaction with plasma.

Let us consider a simplified model of this process. Each filament carries a strong current, which can be estimated as $-feN_e c$, where $f \leq 1$ and N_e is the background density. This currents magnetize the plasma. Quasi-static magnetic field, generated by such current at the distance r from the axis is $B^s_\phi = 2\pi r(feN_e)$. Under certain conditions, this field can reach the value of the light magnetic field $B_l = aB_0$, $B_0 = m_e c\omega/e \approx 107$ MG. The ratio of these fields can be rewritten as

$$\frac{B^s}{B^l} = \frac{1}{a}\frac{fN_e}{N_{cr}}\frac{\pi r}{\lambda} \ , \tag{1.83}$$

where λ is the laser wavelength, $N_{cr} = \pi m_e c^2/(e\lambda)^2$.

This very complex situation was investigated in 2D and 3D PIC simulations in papers [50, 51]. It was shown, that the quasistatic magnetic field is strong enough to pitch the electrons, and therefore to direct the light deflection. As a result the current and light filaments can merge into the single channel, which contains a significant part of incident laser power. The physical reason of this merging is the attraction of electric currents inside the filaments. In 3D PIC simulation [51] it was shown, that the incident beam first propagates through an unstable filamentary stage and then collapses into the single channel with a width one-two λ.

1.3.3 Electron plasma waves

Let we consider now the plasma in one-fluid approximation, i.e. as electron fluid. In that way we will use the electrons density $N(\mathbf{r}, t)$ and the velocity $\mathbf{v}(\mathbf{r}, t)$ for the plasma description. The equation of motion and the set of Maxwell equations will be used to follow plasma evolution.

To investigate electron density oscillations we will consider the Poisson's equation:

$$\nabla \cdot \mathbf{E} = -4\pi e(N - N_0) \ , \tag{1.84}$$

together with the equation of motion:

$$m_e \frac{d\mathbf{v}}{dt} = -e\mathbf{E} - \frac{1}{N}\nabla P \ , \tag{1.85}$$

and continuity equation:

$$\frac{\partial N}{\partial t} + \nabla \cdot (N\mathbf{v}) = 0 \ . \tag{1.86}$$

We will use isothermal approximation, so $P = Nk_BT$ is the thermal pressure.

Let us designate is the uniform background density as N_0. We will consider small density perturbations $|N - N_0| \ll N_0$. Then one can write

$$\begin{aligned} N(x,t) &= N_0 + N_1(x,t) \ , & (1.87)\\ \mathbf{v}(x,t) &= v_1(x,t)\ \mathbf{e_x} \ , & (1.88)\\ \mathbf{E}(x,t) &= E_1(x,t)\ \mathbf{e_x} \ , & (1.89)\\ P(x,t) &= P_0 + P_1(x,t) \ . & (1.90) \end{aligned}$$

We will search for the plane wave solutions for which

$$\{n_1, v_1, E_1, P_1\} \propto e^{i(kx - \omega t)} \ . \tag{1.91}$$

So in Eq. (1.87)-(1.90) we can substitute $\partial_t \to -i\omega$, $\partial_x \to ik$.

Let us first consider *cold* plasma with $P \equiv 0$. When we have a set of algebraic equations

$$\left\{ \begin{array}{rcl} ikE_1 &=& -4\pi e N_1 \ , \\ -i\omega m_e v_1 &=& -eE_1 \ , \\ -i\omega N_1 &+& ikN_0 v_1 = 0 \ . \end{array} \right. \tag{1.92}$$

This system has a non-trivial solution if

$$\omega^2 = \frac{4\pi e^2 N_0}{m_e} \equiv \omega_p^2 \ . \tag{1.93}$$

This solution describes oscillations of the electron fluid with the plasma frequency ω_p for arbitary wave vector k.

Laser pulses, which have the dispersion relation $\omega_L^2 = \omega_p^2 + k^2c^2$ and propagating with group velocity $v_{gr}^{las} = c[1 - (\omega_p/\omega_L)^2]^{1/2}$ in plasma, excite plasma waves which trail with the laser pulse. Their phase velocity v_p equals to the group velocity v_{gr}^{las} of the laser pulse, leading to $\beta_p = v_p/c \simeq v_{gr}^{las}/c = c[1 - (\omega_p/\omega_L)^2]^{1/2}$. In the context of non-linear plasma waves and of the wakefield acceleration to be discussed below, the γ-factor of the plasma wave

$$\gamma_p = \frac{1}{1 - \beta_p^2} = \frac{\omega_L}{\omega_p} = \sqrt{\frac{n_{crit}}{n_0}} \ . \tag{1.94}$$

plays a central role; as it turns out, γ_p is completely determined by the electron density n_0 and the critical density n_{crit} at which the plasma frequency (1.93) equals to the laser frequency.

Chapter 2

Theory of electron acceleration

2.1 Direct electron acceleration in plasma channel

2.1.1 Betatron frequency

In this part described mechanism of DLA(direct laser acceleration) in self-focused laser plasma channels. Electrons propagating along the channel axis may interact resonant with the laser field travelling in same direction. The magnetic wiggler, causing the electron to make transverse oscillation and to couple it to the transverse electric field of the light wave in the free electron configuration, is replaced in the present situation by the quasi-static electric and magnetic fields of the plasma channel. Net energy transfer from the laser wave to the electron occurs at relative phase just opposite (shifted by π) to that in FEL. In this sense it may be called inverse free electrons acceleration (IFEL) mechanism.

Let us initially derive basic expressions for quasi-static electric and magnetic fields of the plasma channel. For this purpose, we consider a stationary cylindrical laser plasma channel with uniform electron density $n_e = fn_0$. The factor $f(0 \leq f \leq 1)$ accounts for electron expulsion from the channel due to the ponderomotive pressure of the laser pulse; other hand the ion density $n_i = n_0$ is uncharged. The corresponding net charge density $(1 - f)n_0$ then creates the radial electric field

(2.1)

$$-eE_r = (1 - f)m\omega_p^2/2 \cdot r \ . \tag{2.2}$$

The light propagating in the channel drives the electrons in forward direction at almost the velocity of ligth, producing a current density $-efn_0c$ which creates an azimutal magnetic field

$$-eB_\varphi = fm\omega_p^2/2 \cdot r. \tag{2.3}$$

Solving the equation of radial motion of an electron in the channel,

$$m\gamma d^2r/dt^2 = -eE_r - (-eB_\varphi) = -m\omega_p^2/2 \cdot r \ , \tag{2.4}$$

we find that oscillation betatron frequency is

$$\omega_\beta^2 = \omega_p^2/2\gamma. \tag{2.5}$$

We conclude that electric and magnetic fields of the channel cooperate in such a way that electrons moving mainly in axial direction feel a harmonic oscillator potential in radial direction which causes them to oscillate radially with ω_β.

2.1.2 Acceleration in plasma channel

Analytically electron acceleration inside a plasma channel can be obtained from the single-electron equations describing electrons simultaneously exposed to the laser fields $\mathbf{E_L}, \mathbf{B_L}$ and to the quasistatic channel fields $\mathbf{E_C}, \mathbf{B_C}$. Here we restrict ourselves to planar (x, y) geometry with a linear polarized laser field $\mathbf{E_L} = E_L\mathbf{e_y} = E_0\mathbf{e_y}\cos\omega(t - x/v_p), \mathbf{B_L} = E_L\mathbf{e_z}/\beta_p$, having phase velocity $\beta_p = v_p/c$ in plasma, and the channel fields $\mathbf{E_C} = E_C\mathbf{e_y} = k_E y\mathbf{e_y}, \mathbf{B_C} = B_C\mathbf{e_z} = k_B y\mathbf{e_z}$. Using dimensionless variables

$$\begin{array}{c} p \to p/mc, \beta \to v/c, t \to \omega t, \\ x \to x\omega/c, E \to eE/m\omega c, B \to eB/m\omega, \end{array} \tag{2.6}$$

we find

$$\frac{dp_x}{dt} = -\frac{\beta_y}{\beta_p}E_L - \beta_y B_C \ , \tag{2.7}$$

$$\frac{dp_y}{dy} = -\left(1 - \frac{\beta_x}{\beta_p}\right)E_L - E_C + \beta_x B_C \ , \tag{2.8}$$

$$\frac{d\gamma}{dt} = -\beta_y(E_L + E_C) \ . \tag{2.9}$$

The energy integral Eq. (1.29), derived above for the laser field alone, can be generalized to the channel situation and gives

$$(\gamma + \phi) - \beta_p p_x = const \ , \tag{2.10}$$

where $\phi = (k_E + v_x k_B)y^2/2$ is the channel potential and $\gamma = \sqrt{1 + p_x^2 + p_y^2}$. Though an exact analytical solution of Eqs. (2.7)-(2.9) is not possible, they can help to understand the mechanism of acceleration. Equation (2.8) for the transverse motion

$$\frac{d^2y}{dt^2} + \omega_\beta^2 y = \left[\left(\frac{dy}{dt}\right)^2 - \left(1 - \frac{\beta_x}{\beta_p}\right)\right]\frac{E_L}{\gamma} + \left(\frac{dy}{dt}\right)^2\frac{k_E y}{\gamma} \tag{2.11}$$

describes a driven oscillator with the frequency

$$\omega_\beta^2 = (k_E + \beta_x k_B)/\gamma \ , \tag{2.12}$$

corresponding to betatron oscillations in the static E_C and B_C field. The driving force on the right-hand side Eq. (2.11) hits the resonance when

$$\omega_\beta = 1 - \beta_x/\beta_p \ . \tag{2.13}$$

This resonance condition states that when an electron makes one oscillation, the electromagnetic wave which propagates with $\beta_p > 1$ overtakes it exactly by one period. It appears that the resonant electron energy γ is not a monotonic function of k_E and k_B. At a given $\beta_p > 1$, the resonance can only be reached for a sufficiently strong self-generated electrostatic field satisfying the condition

$$k_E > \gamma_0[5\beta_p^2 + 4 - 3\beta_p\sqrt{(\beta_p^2+8)}]/(2\beta_p^2) \ , \tag{2.14}$$

where the resonant energy

$$\gamma_0 = \sqrt{2}[\beta_p\sqrt{(\beta_p^2+8)} - \beta_p^2 - 2]^{-1/2} \ , \tag{2.15}$$

or

$$\beta_x = [-\beta_p + \sqrt{(\beta_p^2+8)}]/2 \ . \tag{2.16}$$

2.1.3 Synchrotron oscillations

Let us now consider longitudinal electron motion in the channel. As it turns out, Eq. (2.11) becomes much simpler in the ultra-relativistic limit $\gamma \gg 1$. Then ω_β changes slowly on the time scale of one betatron oscillation and for the transverse motion of the electron we may write:

$$\begin{array}{c} p_y = P_y \cos\theta_\beta \\ t_t\theta_\beta = \omega_\beta \end{array} \ . \tag{2.17}$$

where P_y is the amplitude of the oscillating transverse momentum. The maximum transverse displacement of the electrn is $y_0 = P_y/\omega_\beta$. The laser field at the electron position is $E_L = E_0\cos(t - x/\beta_p)$. Using Eq. (2.9) we write down the final set of IFEL equations:

$$d_x\left(\gamma + \frac{k_E y^2}{2}\right) = -E_0\frac{P_y}{2p_x}(\cos\Psi + \cos\psi) \ , \tag{2.18}$$

$$\beta_x d_x\Psi = \omega_\beta - \left(1 - \frac{\beta_x}{\beta_p}\right) \ , \tag{2.19}$$

$$\beta_x d_x\psi = \omega_\beta + \left(1 - \frac{\beta_x}{\beta_p}\right) \ , \tag{2.20}$$

where Ψ is the slowly oscillating ponderomotive phase of an electron in the bucket produced by the laser wave, while the fast phase ψ rotates with $2\omega_\beta t$.

According to Eq. (2.18), electrons are accelerated for ponderomotive phases, satisfying $\pi/2 < \Psi < 3\pi/2$, and are deccelerated otherwise. The maximum acceleration is achieved when the betatron oscillations are exactly in counterphase with the laser electric field, by the reason of negative electron charge. This mean that when the electron moves with its highest transverse velocity near the channel axis, the electric field of the laser pulse is also at its maximum and has the accelerating direction. When the electron reaches the turning point at the channel boundary the laser field vanishes. As the electron reverses its transverse motion, the direction of the laser electric field also reverses direction, and the electron continues gaining energy.

The continuous growth of γ leads to a corresponding decrease of ω_β and detuning according to Eq. (2.19). The electron then dephases, and acceleration eventually stops. To describe this effect quantitatively, we use Eq. (2.18)-(2.19) and obtain for the ponderomotive phase Ψ the usual IFEL nonlinear pendulum equation [52]:

$$d_t^2 \Psi = E_0 \frac{\omega_\beta}{4\gamma} \sin\alpha \cos\Psi \ . \tag{2.21}$$

Here, α is the angle under which the electron intersects with the channel axis, such that $\sin\alpha = P_y/\gamma$, and we have neglected smaller terms of the order of $\sim \gamma^{-3}$. After many synchrotron rotations in bucket, electrons mix in phase space; also different electrons run at different angles α to the channel axis, and as a consequence the electron energy spectrum acquires a thermal-like distribution. As we see from Eq. (2.18), the electron energy gain is proportional to the laser pulse electric fild E_0, which in turn is $\sim I^{1/2}$.

2.2 Non-linear physics of acceleration

2.2.1 Non-linear relativistic plasma waves

In this part we derive basic properties of the non-linear regime, making use of the one-dimensional quasi-static approximation. In this case, the relativistic one-dimensional equations for the fluid velocity u in the x-direction are

$$\frac{\partial n}{\partial t} + \frac{\partial}{\partial x}(nu) = 0 \ , \tag{2.22}$$

$$\left(\frac{\partial}{\partial t} + u\frac{\partial}{\partial x}\right)(\gamma m u) = -eE - \frac{1}{n}\frac{\partial p_e}{\partial x} \ , \tag{2.23}$$

$$\frac{\partial E}{\partial x} = 4\pi e(n_0 - n) \ , \tag{2.24}$$

with $\beta = u/c$ and $\gamma = 1/\sqrt{1-\beta^2}$. We look for wave solution on $n(x,t), u(x,t)$ and $E(x,t)$ that depend only on $\tau = \omega_p(t - x/v_p)$. Since $\partial/\partial t = \omega_p d/d\tau, \partial/\partial x = -(\omega_p/v_p)d/d\tau$, one finds

$$\hat{n} = 1/(1 - \beta/\beta_p) \ , \tag{2.25}$$

$$(1 - \beta/\beta_p)\frac{d}{d\tau}\beta\gamma = -\hat{E} \ , \tag{2.26}$$

$$d\hat{E}/d\tau = \beta/(1 - \beta/\beta_p) \ , \tag{2.27}$$

where we have introduced dimensionless variables $\hat{n} = n/n_0, \beta_p = v_p/c, \hat{E} = eE/(m\omega c)$, and cold plasma is assumed with $p_e \equiv 0$. Combining the second and the third of these equations, we can write

$$\hat{E}\frac{d\hat{E}}{d\tau} = \frac{d}{d\tau}(\hat{E}^2/2) = \beta\frac{d}{d\tau}(\beta\gamma) = -\frac{d\gamma}{d\tau} \ , \tag{2.28}$$

and obtain the integral

$$\hat{E}(\gamma) = \sqrt{2(\gamma_m - \gamma)} \ , \tag{2.29}$$

where γ_m is the integration constant corresponding to maximum fluid velocity u_m with $\beta_m = u_m/c$ and $\gamma_m = 1/\sqrt{1 - \beta_m^2}$. For $\gamma = \gamma_m$, the electric field $\hat{E}$ vanishes, while the maximum field

$$\hat{E}_m = \sqrt{2(\gamma_m - 1)} \ , \tag{2.30}$$

is obtained at location, where $u = 0$ and $\gamma = 1$.

Explict expressions for velocity, density and electric field as function τ can be obtained in the non-relativistic limit $\beta_p \ll 1$ and $\gamma_p = 1 + \beta_p^2/2$. We find from Eqs. (2.26) and (2.29)

$$\pm d\tau = \frac{(1 - \beta/\beta_p)d(\beta\gamma)}{\sqrt{2(\gamma_m - \gamma)}} \simeq \frac{(1 - \beta/\beta_p)d(\beta/\beta_m)}{\sqrt{(1 - (\beta/\beta_m)^2}} \tag{2.31}$$

and after integration

$$\pm(\tau - \tau_0) = \arcsin((\beta/\beta_m)) + (\beta/\beta_p)\sqrt{1 - (\beta/\beta_m)^2} \ . \tag{2.32}$$

From this we can find $\beta(\tau)$ and thereby $\hat{n}(\tau)$ and $\hat{E}(\tau)$, using Eqs. (2.25) and (2.29). For small wave amplitudes $\beta_m \ll \beta_p$, Eq. (2.32) can be inverted, and we recover the linear wave result

$$\beta = \beta_m \sin(\tau - \tau_0) \ , \tag{2.33}$$

$$\hat{n} = \frac{1}{1 - \beta/\beta_p} = 1 + (\beta_m/\beta_p)\sin(\tau - \tau_0) \ , \tag{2.34}$$

$$\hat{E} = \sqrt{\beta_m^2 - \beta_p^2} = \beta_m \cos(\tau - \tau_0) \ . \tag{2.35}$$

Extremum of $\beta(\tau), \hat{n}(\tau)$ and the zeros of $\hat{E}(\tau)$ dont shift in τ when increasing β_m, while the zeros of $\beta(\tau), \hat{n}(\tau)$ and the extremum of $\hat{E}(\tau)$ are shifted in such a way that,

in the non-linear high-amplitude regime, velocity and density develop sharp wave crests with wide troughs in between, while the electric field acquires a sawtooth shape. In the half-waves with negative $\hat{E}(\tau)$, electrons can be accelerated. This is the basic principle of plasma wave accelerators.

The non-linear solution derived above exists only as long as the fluid velocity β stays below the phase velocity β_p of the plasma wave. For $\beta = \beta_p$, the plasma wave develops cusps at the wavecrests moving with phase velocity; they have infinite density according Eq. (2.25). For $\beta_m > \beta_p$, the density peaks move faster then the wave and start to overtake other fluid elements. Then a multi-velocity regime develops, and this is calle *wave breaking*. This regime cannot be described within the approximate picture of a plasma fluid. The maximum electric field achievable in a cold plasma at the point of wave breaking [5] is given by Eq. (2.27):

$$E_{WB}/E_0 = \sqrt{2(\gamma_p - 1)} \; , \tag{2.36}$$

where $E_0 = mc\omega_p/e$ and $\gamma_p = 1/\sqrt{1-\beta_p^2}$ is the γ-factor of the plasma wave. For $\beta_p \ll 1$, we recover the non-relativistic result ([6])

$$E_{WB} = E_0\beta_p = mv_p\omega_p/e \; . \tag{2.37}$$

The wave breaking limit is of central importance for laser wakefield acceleration, because it sets the scale for the maximum energy to which a particle can be accelerated in the wave. Apparently, the cold relativistic value of E_{WB} exceeds any limit for sufficiently large γ_p which can be obtained for small enough plasma density. Relativistic effects tend to prevent wave breaking because fluid velocities cannot exceed the velocity of light. On the other hand, thermal effects on the wave breaking strongly interfere and set an upper limit.

2.2.2 Wake field acceleration

The plasma waves can be exited by laser pulses. Here we consider the case of oa intense laser pulse with amplitude a_0 propagating in underdense plasma and with group velocity $v_{gr}^{las} = c\sqrt{1-(\omega_p/\omega)^2}$. Its ponderomotive force pushes electrons at the front in laser direction, thus exiting a plasma wave which trails the laser pulse. The γ-factor of the plasma wave has been given already in Eq. (1.94), showing that $\gamma_p \sim n_0^{-1/2}$. High γ_p can be reached for low plasma density n_0.

Here we restrict ourselves to laser pulses with a duration shorter than a plasma oscillation such that the laser pulse fits into the first bucket of the plasma wave. The balance between light pressure and plasma pressure is obtained from Eq. (1.70) requiring $\nabla(\varphi - \gamma) = 0$. Combining the plasma electric field $E = (mc^2/e)\nabla\varphi$, the file unit $E_0 = mc\omega_p/e$, and γ-factor of the plasma electrons for circular polarized light $\gamma = \sqrt{1+|a|^2}$, we find

$$\frac{E}{E_0} = \frac{c}{\omega_p}\nabla\gamma = \frac{1}{2\gamma}\frac{c}{\omega_p}\nabla|a|^2 \; . \tag{2.38}$$

Approximating $\nabla|a|^2 \approx 2k_p|a|^2$, where $k_p = \omega_p/c$, and applying Eq. (2.38) at the location of maximum fields, we obtain

$$\frac{E_{max}}{E_0} \approx a_0^2/\sqrt{1+a_0^2}\ . \tag{2.39}$$

This holds for circular polarization; in the case of linear polarization, a_0^2 has to be replaced by $a_0^2/2$. A more rigorous derivation of this result was given e.g. by [53] et al. and [43] et al.

In 1979 Tajima and Dawson proposed to use high-amplitude plasma waves for the particle acceleration, in particular using laser pulses to exite plasma waves. This seed paper has triggered a new field of plasma-based accelerators, and an excellent review was given by [2] et al., containing a comprehensive list of references.

Following [2] et al., we estimate the energy that an electron can gain when traapped in the wakefield as

$$eW \approx eE_m L_d\ , \tag{2.40}$$

where E_m is the maximum electric field and L_d is the dephasing length, which is the maximum distance over which the electron can experience the accelerating field. Let us consider a plasma wave with $v_p \simeq c$ such that $\gamma_p \gg 1$ and a trapped electron which is also moving close to c such that the acceleration time is given by $t_d = L_d/c$. The phase distance of the accelerating half-wave is then $\Delta\tau = \omega_p(L_d/v_p - t_d) = \pi$ and determines the dephasing length

$$L_d = \frac{\pi}{\omega_p}\frac{c}{(c/v_p - 1)} \simeq \lambda_d\gamma_p^2\ , \tag{2.41}$$

using $(c/v_p - 1) \simeq 1/(2\gamma_p^2)$ and $\lambda_p \simeq 2\pi c/\omega_p$. Having L_d, we find for the maximum energy gain approximate result

$$eW_m \approx 2\pi\gamma_p^2(E_m/E)mc^2\ . \tag{2.42}$$

The energy gain can be obtained more precisely using the non-linear cold plasma solution. At this point, we calculate the gain first in the frame of the wave, running with phase velocity v_p in x-direction. The Lorentz transformation into the moving frame (dashed quantities) reads for space and time coordinates

$$\begin{aligned} cccx' &= \gamma_p(x - v_p/c), \\ t' &= \gamma_p(t - v_p x/c^2), \end{aligned} \tag{2.43}$$

and for the electric filed [54]

$$\mathbf{E}' = \gamma_p(\mathbf{E} + \beta_\mathbf{p} \times \mathbf{B}) - \frac{\gamma_p^2}{\gamma_p + 1}\beta_\mathbf{p}(\beta_\mathbf{p} \cdot \mathbf{E})\ . \tag{2.44}$$

In the present case with $\mathbf{B} = 0$ and both $\mathbf{E}$ and $\beta_\mathbf{p}$ in x-direction, we find that the longitudial E-field is a Lorentz invariant:

$$E_x' = E_x\ . \tag{2.45}$$

We can therefore calculate the energy gain in the moving frame

$$W' = -e \int E'_x dx' = e \int E_x(\gamma_p v_p/\omega_p) d\tau = \beta_p \gamma_p mc^2 \int \hat{E}(\tau) d\tau \ , \tag{2.46}$$

making use of $x' = -(\gamma_p v_p/\omega_p)\tau$. The electric field $eE_x(\tau)/(mc\omega_p) = \hat{E}(\tau)$ has already been derived in laboratory frame. Using Eq. (2.26) we find

$$\int \hat{E} d\tau = \int_{-\beta_m}^{+\beta_m} (1 - \beta/\beta_m) d(\beta\gamma) = 2\beta_m \gamma_m \ , \tag{2.47}$$

when integrating over the half-wave from β_m to $-\beta_m$ which corresponds to maximum acceleration. The maximum energy gain of the electron in wave frame is then

$$W'_{max} = \gamma' mc^2 = 2(\beta_p \gamma_p)(\beta_m \gamma_m) mc^2 \ . \tag{2.48}$$

Again we consider the case of interests for electron acceleration with the phase velocity $\beta_p \simeq 1$ and $\gamma_p \gg 1$. On the other hand, we allow for arbitrary wave amplitudes β_m and corresponding γ_m, though satisfying $\Gamma' \gg 1$ such that the electron is finally in an ultra-relativistic state. The energy gain seen in laboratory system then is

$$W_{max} = \gamma_p (W'_{max} + v_p W'_{max}/c) \simeq 4\gamma_p (\beta_m \gamma_m) mc^2 \ . \tag{2.49}$$

Recalling $\beta_m \gamma_m = (\gamma_m^2 - 1)^{1/2} = E_m (1 + \hat{E}_m^2/4)^{1/2}$, we find

$$W_{max} \simeq 4\gamma_p^2 mc^2 \begin{cases} E_m/E_0 & \text{for } E_m \ll E_0 \\ (E_m/E_0)^2/2 & \text{for } E_m \gg E_0 \end{cases} \tag{2.50}$$

These results were first obtained by [55]. At the point of wave breaking $\gamma_m = \gamma_p$, they imply $W_{max} \simeq 4\gamma_p^3 mc^2$. This is remarkable result. It indicates that already plasma waves with $\gamma_p = 10$, corresponding to a plasma density of $10^{19} cm^{-3}$, could accelerate electrons, injected at $\gamma_p mc^2 \simeq 5MeV$, to an energy of $2GeV$ over distance of $L_d = \gamma_p^2 \lambda_{Np} \simeq \gamma^{5/2} \lambda_p \approx 3mm$. To reach the wave breaking field in a cold plasma, $E_{WB}/E_0 = [2(\gamma_p - 1)]^{1/2} \approx 4.2$, one would need an ultra-short ($\approx 10fs$) laser pulse of linear polarization with $a_0^2 = 10$.

The analytical one-dimension wave analysis given above provides a basic understanding if wakefield acceleration in non-linear plasma waves. However, it is restricted to regimes below wave breaking and cannot describe the physics of wavebreaking itself, which is of kinetic nature and essentially multi-dimensional.

As it turns out, wakefield acceleration is not limited by wave breaking. On the contrary, new schemes of wakefield acceleration emerge in the broken-wave regime, where the proccess of continuous wave breaking leads to abundant self-trapping of electrons and efficient generation of high-current electron bunches. For laser pulses longer than a plasma wavelength, self-modulated laser wakefield acceleration occurs, and experiments in this regime were most successful in terms of both high energies and large number of

accelerated electrons [26] et al.. For laser pulses shorter then the plasma wavelength, another very interesting regime was found recently by Pukhov and Meyer-ter-Vehn (2002). At sufficiently high laser intensities, the wakefield is driven so strongly that it breaks completely after the first plasma oscillation and solitary wakefield bubble forms, which is essentially void of background plasma electrons, but which traps continuosly electrons at the breaking point on the rear side and accelerates them efficiently.

2.2.3 Acceleration in the "bubble" regime

Here, we restrict us by short generally description of the "bubble" regime, the main features of which are the following:

- a cavity free from electrons is formed behind laser pulse instead of plasma wave;
- a dense bunch of relativistic electrons is self-generated;
- the laser pulse propagates many Rayleigh lengths witout significant spreading.

The electron dynamics is defined by the ponderomotive force and the electromagnetic fields of bubble density patterns. The most important three are following:

- the electron plasma cavity with the large ion charge;
- the electrons sheath around the cavity forming the bubble boundaries;
- the bunch of accelerated electrons growing behind laser pulse in the cavity.

The density of electrons sheath peaks at the head of laser pulse and at the base of the cavity. These density peaks are formed by relativistic electrons with velocity $v \simeq v_0$, where v_0 is the velocity of bubble. The bubble base is the source of electrons, which get trapped and accelerated to $\gamma \gg \gamma_0$, where $\gamma_0 = \sqrt{1 - v_0^2/c^2}$ is the relativistic gamma-factor of the bubble.

The phenomenological theory of electrons dynamics and acceleration mechanism in the "bubble" regime we will discuss more detailed in the next chapter.

Chapter 3

Numerical simulation

3.1 Trajectories of electron in the Bubble

3.1.1 Introduction

In relativistic laser plasma interaction, electrons can be simultaneously accelerated and wiggled in a plasma cavity to emit an intense beam of x-rays, the so-called betatron radiation. Consisting in radiation from charged particles, the features of the betatron source are directly linked to electron trajectories. In this chapter we show how an image of electrons orbits in the bubble can be directly presented from numerical simulation with VLPL3D PIC-code. Using the postprocessing, we have characterized electrons trajectories into the bubble and have shown that most of electrons can follow similar transverse trajectory.

3.1.2 Phenomenological theory

Before considering the relativistic cavity moving in plasma we summarize the results for field within ionic sphere. The electromagnetic field of the uniformly charged sphere at rest is purely electrostatic

$$\mathbf{E} = \frac{\mathbf{r}}{3}, \quad \mathbf{B} = 0, \quad \varphi = 1 + \frac{R^2}{6} - \frac{r^2}{6} \ , \tag{3.1}$$

where R is the radius of sphere with charge density $|e|n_0$ and we choose that the potential is equal to unity at the sphere boundary.

Here we use dimensionless variables, normalized time to ω_p^{-1}, lengths to c/ω_p, velocity to c, electromagnetic fields to $mc\omega_p/|e|$ end electrons density n to background density n_0. The ionic sphere runs with relativistic velocity $v_0 \simeq 1$ in x-direction have inside fields

$$\begin{aligned} E_x = 0, E_y = B_z = y/2 \ , \\ B_x = 0, E_z = -B_y = z/2 \ , \end{aligned} \tag{3.2}$$

where the terms proportional to $\gamma_0^{-2} = 1 - v_0^2 \ll 1$ are neglected. The Lorentz force on relativistic electrons moving inside the sphere with velocity $\mathbf{v} = -\mathbf{v_0} = -\mathbf{e_x}$ is

$$\begin{array}{c} F_x = 0, F_y = -E_y - B_z = -y \ , \\ F_z = -E_z + B_y = -z \ , \end{array} \tag{3.3}$$

where it is negligible for electron with $\mathbf{v} = \mathbf{v_0} = \mathbf{e_x}$ because of relativistic compensation of the electrostatic force by the self-magnetic force [56].

For the fields inside spherical electron cavity, contrary to the case discussed above, the ions are immobile in the cavity while while it runs with relativistic velocity. The ions dynamics is neglected because the cavity radius is assumed to be smaller than the ion response length $\simeq c/\omega_p^{ion}$, where ion plasma frequency $\omega_p^{ion} = 4\pi e^2 n_0/M_{ion}$. We rewrite the Maxwell equations in terms of potentials using the following gauge:

$$A_x = -\varphi \ . \tag{3.4}$$

We get

$$\Delta\Phi = 1 - n\left(1 - \frac{p_x}{\gamma}\right) + \left(\frac{\partial}{\partial t} + \frac{\partial}{\partial x}\right)(\nabla \cdot \mathbf{A}) + \frac{1}{2}\frac{\partial}{\partial t}\left(\frac{\partial}{\partial t} - \frac{\partial}{\partial x}\right)\Phi \ , \tag{3.5}$$

$$\nabla \times \nabla \times \mathbf{A} + n\frac{\mathbf{p}}{\gamma} + \frac{\partial}{\partial t}\left(\frac{\partial \mathbf{A}}{\partial t} - \frac{\nabla\Phi}{2}\right) = 0 \ . \tag{3.6}$$

Here we use wakefield potential $\Phi = A_x - \varphi$ instead of the scalar one, $\mathbf{p}$ is electron momentum.

Then we use approximation assuming that all quantities depend on $\chi = x - v_0 t$ instead of x and t. Equations reduce to the form

$$\Delta\Phi = \frac{3}{2}(1-n) + n\frac{p_x}{\gamma} - \frac{1}{2}\frac{\partial}{\partial\chi}(\nabla_\perp \cdot \mathbf{A}_\perp) \ , \tag{3.7}$$

$$\nabla_\perp \mathbf{A}_\perp + \nabla_\perp(\nabla_\perp \cdot \mathbf{A}_\perp) = n\frac{p_x}{\gamma} + \frac{1}{2}\nabla_\perp\frac{\partial\Phi}{\partial\chi} \ . \tag{3.8}$$

where terms proportional γ_0^{-2} are neglected. With electron density $n = 0$ inside cavity we have

$$\Delta\Phi = \frac{3}{2} - \frac{1}{2}\frac{\partial}{\partial\chi}(\nabla_\perp \cdot \mathbf{A}_\perp) \ , \tag{3.9}$$

$$\nabla_\perp \mathbf{A}_\perp - \nabla_\perp(\nabla_\perp \cdot \mathbf{A}_\perp) = \frac{1}{2}\nabla_\perp\frac{\partial\Phi}{\partial\chi} \ . \tag{3.10}$$

The solution of Eqs. (3.9) and (3.10) with spherical symmetry is

$$\Phi = 1 - \frac{R^2}{4} + \frac{r^2}{4}, A_x = -\varphi = \frac{\Phi}{2}, \mathbf{A}_\perp = 0 \ , \tag{3.11}$$

where R is the radius of cavity, $r^2 = \chi^2 + y^2 + z^2$ and integration constant $\Phi(R) = 1$.

Therefore, electromagnetic fields in the cavity are:

$$\begin{aligned} E_x = \chi/2, E_y = -B_z = y/4 \\ B_x = 0, E_z = B_y = z/4 \ . \end{aligned} \tag{3.12}$$

The Lorentz force acting on electrons inside the cavity is

$$\begin{aligned} F_x = -\frac{\partial \Phi}{\partial \chi} = -E_x = -\chi/2 \ , \\ F_y = -\frac{\partial \Phi}{\partial y} = -E_y + B_z = -y/2 \ , \\ F_z = -\frac{\partial \Phi}{\partial z} = -E_z - B_y = -z/2 \ . \end{aligned} \tag{3.13}$$

Now we describe the cavity shape. The transverse size of the cavity reaches maximum near the middle which passes through cavity center. In the area where this plane cuts the boundary of cavity the electron sheath contain a return current carried by weakly relativistic electrons. On these electrons acts the Lorentz force (3.13), which is nearly balanced by the ponderomotive force. The transverse radius R of the cavity can thus be estimated from the equation

$$\frac{R}{4}(1 - v_x) \simeq \frac{R}{4} \simeq F_{pond} \simeq \frac{\partial}{\partial R}\sqrt{1 + a^2(R)} \ , \tag{3.14}$$

where we assume the spherical symmetry for the ion cavity and circularly polarized laser pulse [57].

When the force from the bunch becomes stronger than the ponderomotive force, cavity shape determined by the bunch. The bunch density n_b is much higher than the plasma density, then we can refer to the theory of relativistic electron beam in plasma in ion-focused regime [58] and use it to estimate the bubble transverse radius. The equilibrium at the interface near the middle plain is provided by the balance of the Lorentz forces from the cavity (3.13) and from the bunch electrons. The transverse radius in bunch dominated regime is

$$r_b\sqrt{n_b} < R < r_b\sqrt{2n_b} \ , \tag{3.15}$$

where the lower and upper limits are from a bunch with the weak current $n_b\pi r_b^2 \ll 1$ and strong current $n_b\pi r_b^2 \gg 1$ correspondingly. Plasma electrons flow along the interface in direction opposite to the laser pulse propagation and form the return current sheath. In case of weak the bunch current the width of return current sheath is about c/ω_p and electron energy $\gamma \simeq 1$ is small. At opposite limit $n_b\pi r_b^2 \gg 1$ the sheath electrons gains relativistic energies $\gamma > 1$ and sheath width increase $\simeq \sqrt{\gamma}c/\omega_p$.

In terms the laser pulse is circularly polarized, propagating in x-direction and azimuthal part of electrons trajectories of electrons is neglected (trajectories lies in plain $z = 0$) the average motion in slowly varying bubble fields is defined by averaged Hamiltonian [59, 57] :

$$H = \sqrt{1 + (\mathbf{P^{can}} + \mathbf{A})^2 + a^2} + \varphi \ , \tag{3.16}$$

where $\mathbf{P^{can}}$ is canonical electron momentum, $\mathbf{A}$ and φ are slowly varying vector and scalar potentials and a is vector potential of laser field. Fast electron oscillations are averaged out.

Changing variables in this Hamiltonian

$$x \to x = \chi - v_0 t, P_x \to P_\chi = P_x \tag{3.17}$$

by a canonical transformation with generating function $S = (x - v_0 t)P_\chi$, we have

$$H = \gamma - v_0 P_x - \varphi = \sqrt{1 + (\mathbf{P^{can}} + \mathbf{A})^2 + a^2} - v_0 P_x - \varphi \ . \tag{3.18}$$

Therefore, equations of motion are given by

$$\frac{dP_x}{dt} = -v_x \frac{\partial A_x}{\partial \chi} - v_y \frac{\partial A_y}{\partial \chi} + \frac{\partial \varphi}{\partial \chi} \ , \tag{3.19}$$

$$\frac{dP_y}{dt} = -v_x \frac{\partial A_x}{\partial y} - v_y \frac{\partial A_y}{\partial y} + \frac{\partial \varphi}{\partial \chi} \ , \tag{3.20}$$

$$\frac{d\chi}{dt} = \frac{p_x}{\gamma} - v_0 = v_x - v_0 \ , \tag{3.21}$$

$$\frac{dy}{dt} = \frac{p_y}{\gamma} = v_y \ . \tag{3.22}$$

The laser pulse, cavity and electron sheath run with the velocity v_0; the relativistic gamma-factor of electron bunch is much higher $\gamma_b \gg \gamma_0$. Potentials of Hamiltonian (3.18) depend on χ and slowly change with x and t due to ultra-relativistic electron bunch. If we neglect the time-independent corrections order of $t(v_b - v_0) \simeq t\gamma_0^{-2}/2 \ll 1$ the Hamiltonian is the integral of motion, where $v_b \approx 1 - 1/2\gamma_b^2$ is the bunch velocity.

The necessary condition for electrons trapping in the cavity is the existence of the point of return where $d\chi/dt = 0$. From Eq. (3.21) follows that at this point $p_x = v_0\gamma$. Then integral of motion (3.18) can be rewritten

$$H = \gamma - v_0 p_x - \Phi = 0 \ , \tag{3.23}$$

where we assume the initial conditions are $\mathbf{p} = \mathbf{A}_\perp = a = 0$ and $\Phi = 1$. The relations for p_x and Hamiltonian can be expressed at the return point in the form

$$p_x = v_0\gamma_0\gamma_\perp = v_0\gamma_0^2\Phi \ , \tag{3.24}$$

where $\gamma_\perp^2 = 1 + p_y^2 + a^2$. The area in phase space where the electrons are trapped can be defined as

$$p_x \geq v_0\gamma_0\gamma_\perp = v_0\gamma_0^2\Phi \ . \tag{3.25}$$

To obtain analytical results on the trapping we approximate the bubble by a sphere. The electron sheath around the cavity screens the ion field in the surrounding plasma.

Radial Lorentz force acting on relativistic electrons from this structure can be modeled as

$$F = rS(r-R) = -\frac{r}{4}\left(\tanh\frac{r-R}{d} - 1\right) \ , \tag{3.26}$$

where R is sphere radius, d is the width of electron sheath and $r^2 = \chi^2 + y^2 + z^2$. The potential of this structure is

$$\Phi = 1 + \frac{r^2}{4} - \frac{d^2\pi^2}{48} - \frac{1}{4}rd\ln\left(1 + e^{\frac{2r}{d}}\right) - \frac{1}{8}Li_2\left(-e^{\frac{2r}{d}}\right) \ . \tag{3.27}$$

In the limit $d \to 0$ function $S(r)$ reduces to step function and Eq. (3.27) reduces to Eq. (3.11).

From $p_x = v_0\gamma_0\gamma_\perp = v_0\gamma_0^2\Phi$ follows that trapping most likely occurs on the sphere surface, where $\Phi \simeq \Phi_{min} \simeq 1$. Then trapping condition takes form

$$\frac{p_x}{v_0\gamma_0} = \gamma_\perp \simeq \gamma_0 \ . \tag{3.28}$$

To be trapped electron must be accelerated so that $p_\perp \simeq \gamma_0$ and $p_x \simeq \gamma_0^2$. Integrating numerically Eqs. (3.19)-(3.22)for the potential (3.27) can be found that the cavity can trap electrons initially at rest if

$$R > \gamma_0 \ . \tag{3.29}$$

From Fig. (3.1) seen that only the electrons, whose trajectories run through the wave-breaking region become trapped. Therefore get trapped only small portion of electrons which are initially located in electron sheath near the middle plain. Let we introduce the trajectory divergence η. If initially the average range between electrons in the sheath in middle plain was $\delta\rho$ then it becomes $\eta\delta\rho$ in wavebreaking area. Hence electron in a narrow layer with the width $D/\eta \ll c/\omega_p$ located inside sheath become trapped. Then cross-section σ for electrons trapping can be estimated as

$$\sigma \sim 2\pi R n_s \frac{D}{\eta} \ . \tag{3.30}$$

where n_s is the electron density. The bulk of the plasma electrons, which collide with the laser pulse, enter the sheath with width d. The sheath density can be estimated as the ratio between the area of the circle with radius R and that of the ring with radius R and width d.

$$n_s \sim \frac{R}{2d} \ , \tag{3.31}$$

where $\gamma \simeq 1$ in the sheath assumed. Making use of Eqs. (A.3), (3.30) and (B.10) we finally obtain the estimates for the trapping cross-section as function of the cavity radius:

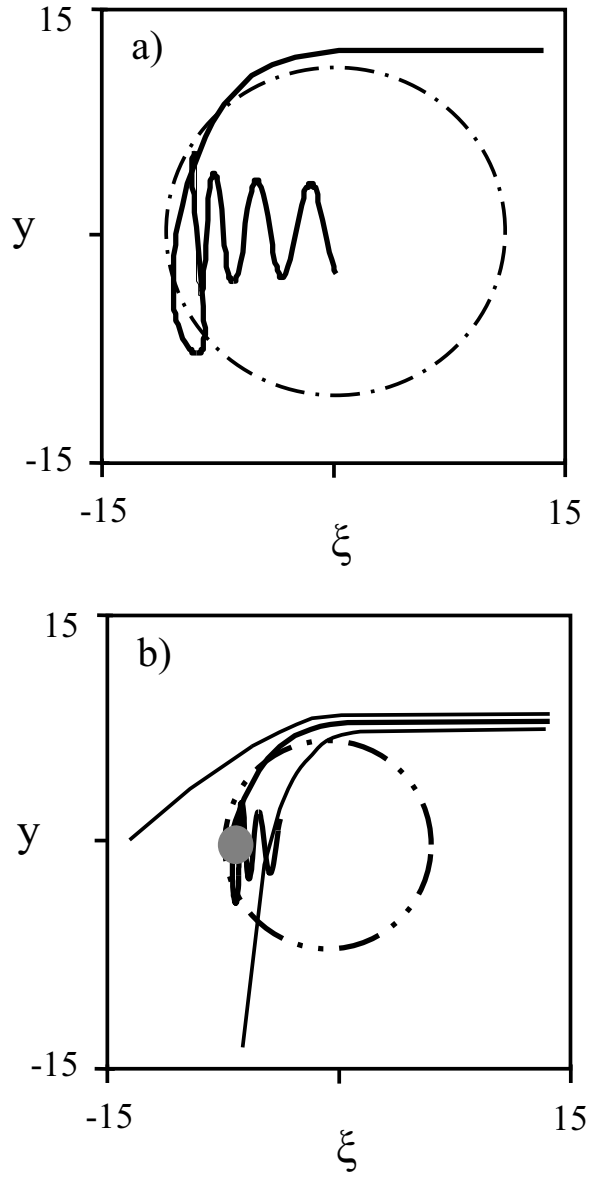

Figure 3.1: Typical electron trajectories in the bubble in the plane $z = 0$. The coordinates are given in c/ω_p.

$$\sigma \simeq \frac{\pi}{d}\left(\ln\frac{R}{2\sqrt{2}}\right)^{-1} . \tag{3.32}$$

3.1.3 Analysis of wakefield electrons orbits in plasma wiggler

In the bubble regime the plasma wave period is of the order of the laser pulse duration. In that case, the first plasma wave period consists on an ion cavity almost free of background electrons in the bubble. The cavity acts, because of its intense electrostatic fields structures, as an electron accelerator and as an electron wiggler. Within the cavity the electron motion consists of a relativistic longitudinal acceleration combined with a transverse oscillation around the cavity axis. So far, none experimental technique has allowed to look into the cavity and probe the electron trajectories. By measured the spatial properties of the x-ray radiation produced by the relativistic electrons as they propagate within the cavity (betatron radiation), [60].

We have simulated the mechanism of Betatron radiation by considering a test particles model in which electrons are accelerated and oscillate in a cylindrical uniformly charged ion channel. The forces experienced by the electrons in the channel are electrostatic and time independent. The channel axis corresponds to the X axis. As initial conditions, we consider an electron entering the channel at initial position $(x_0, y_0, z_0 = 0)$. The channel axis $(x_0 = y_0 = 0)$. The initial momentum is $p_{x_0}, p_{y_0}, p_{z_0}$. In the channel, the electron is submitted to the transverse restoring force due to the ions (obtained from Gauss law) and to the longitudinal electrostatic field representing the wakefield. The equation of motion is then:

$$\frac{d\vec{p}}{dt} = -m\omega_p^2 \vec{r_\perp}/2 + \frac{mc\omega_p}{e}\vec{u}_x,$$

where m is the electron mass, $\vec{r}_\perp$ the transverse position of the electron and $\omega_p = (n_e e^2/m\epsilon_0)^{1/2}$ the plasma frequency, with n_e the plasma electron density, e the electron charge, and $\vec{u}_z$ the unit vector in the channel axis direction X. Here, considering an electron density of 10^{19} cm^{-3}, the longitudinal accelerating field and the transverse fields are respectively of the order of 300 GeV/m and 100 GeV/m for 1 μm excursion. At the first order, we can consider an already relativistic electron at an energy γ_0 and neglect the acceleration term. The equation of motion then reduces to an harmonic oscillator. The electron motion is then an combination of a drift at constant velocity and an oscillatory motion at the betatron frequency $\omega_\beta = \omega_p/\sqrt{2\gamma_0}$.

The complete equation of motion has been integrated numerically to take into account the acceleration. Fig. (3.2) represents a three dimensional and a two dimensional transverse representation of the trajectory of one electron for two typical sets of initial conditions. On figure (1a), initial conditions are $z_0 = 2.5$ μm, $y_0 = 0$ μm, $p_{z_0} = 0, p_{y_0} = 2, p_{x_0} = 10$; on figure (1b) $z_0 = 2.5$ μm, $y_0 = 0$ μm, $p_{z_0} = 0, p_{y_0} = 0, p_{x_0} = 10$. We will choose $p_{z_0} = 0$ and $y_0 = 0$. Indeed, a case with $p_{z_0} \neq 0$ and/or $y_0 \neq 0$ can be reduced to a case with $p_{z_0} = 0$ and $y_0 = 0$ with an appropriate change of reference frame. For both, the motion consists on a transverse oscillatory motion at the Betatron frequency

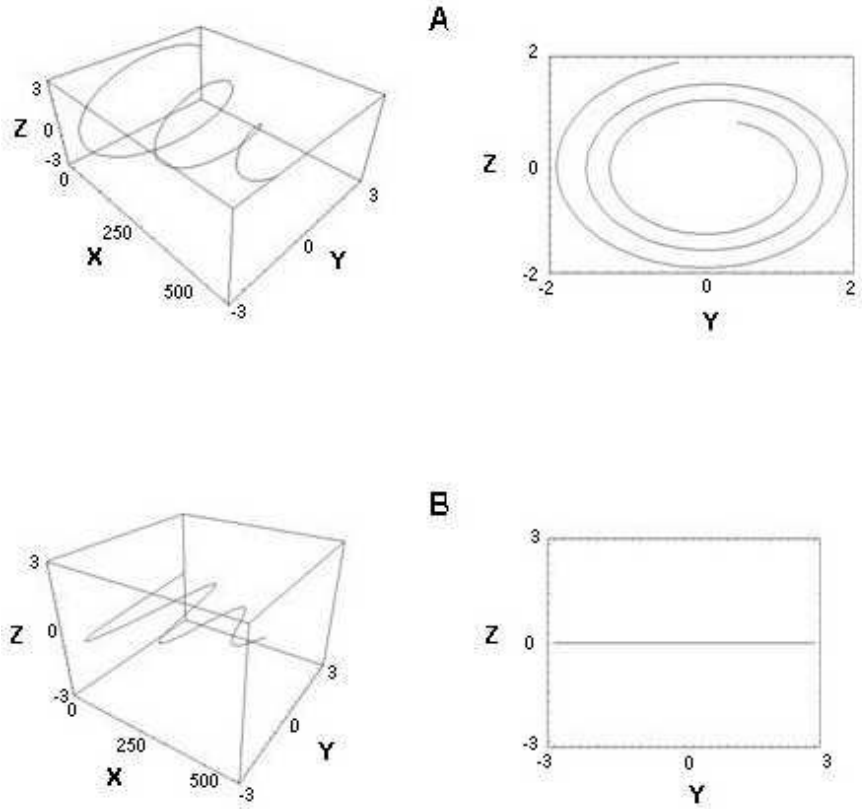

Figure 3.2: Three dimensional and transverse electrons orbits for, (a) $x_0 = 2.5\mu m, y_0 = 0\mu m, p_{x_0} = 0, p_{y_0} = 2, p_{z_0} = 10, n_e = 10^{19} cm^{-3}$, (b) $x_0 = 2.5\mu m, y_0 = 0\mu m, p_{x_0} = 0, p_{y_0} = 0, p_{z_0} = 10, n_e = 10^{19} cm^{-3}$. The electron is accelerated up to 150 MeV

combined with a drift in the longitudinal direction X. From rest, the electron is accelerated to relativistic energies (about 150 MeV here), its effective mass (γm_e) becomes larger and it results in a reduction of the amplitude of the transverse motion and the betatron frequency. This variation of amplitude reduces as the electron becomes more and more energetic. It clearly appears on the transverse orbits graphs; the trajectory is helical. The difference between figure (1a) and figure (1b) relies on the excursion in the Y direction (on figure 2a, the motion is restricted to a a 2D orbit in the Z, X plane; it is 3D on figure (2b)). This depends on the initial transverse momentum p_{y_0}. The initial transverse momentum given to the electron results in an elliptical transverse orbit. Note that, due to the weaker mass of the electron, the importance of p_{y_0} is stronger as it is imposed at the early stages of acceleration.

Betatron radiation is a synchrotron like radiation emitted by the relativistic electrons as they execute oscillations in the channel. The properties of the radiation are described by the formulae of the radiation from a relativistic moving charge. The radiation features directly depend on the electron trajectory. In particular, the critical energy grows as γ^3/R_c and the radiated energy as γ^4/R_c where γ is the electron energy and R_c the instantaneous radius of curvature of the orbit. In our parameter regime (interaction at an intensity $\sim 10^{18}$ W/cm^2 and a helium plasma at $n_e \sim 10^{19}$ cm^{-3}), the radiation consists on a bright x-ray beam (10^9 photons/pulse) with a divergence of a few tens milli radians and a broad band energy spectrum extending up to about 10 keV. The spatial distribution of the radiation (which is measured by placing a detector in the x-ray beam) represents a signature of the electron motions and can reveal the electron orbits discussed above. A straightforward link exists between the orbits and the radiation. Indeed, the energy radiated in a direction of observation $\vec{n}$, obtained by integrating the radiated energy over the frequencies, has a $(1-(\vec{v}/c).\vec{n})^{-1}$ dependence (where $\vec{v}$ is the electron velocity). This implies that the Betatron radiation is emitted in the direction of the electron velocity. The profile of the Betatron x-ray radiation, measured in the far field, is therefore an image of the transverse momentum of the oscillating relativistic electron.

For a single electron in one period of oscillation, Figure (3.3) illustrates schematically the correspondence between the electron trajectory (A), its momenta (B), and the distribution of the emitted radiation(C) for the general case of an elliptical transverse trajectory. On figures A and B, symbols (white circle and blue circle) represent an arbitrary position in space and phase space of an electron along its trajectory. The lines sections on figure C represent the corresponding emission as it could be observed onto a detector placed in the beam. From the measurement of Betatron profiles together with measurement of electrons energies (γ), can be obtained: (p_y,p_z) and (y,z) of the electrons in the ion cavity.

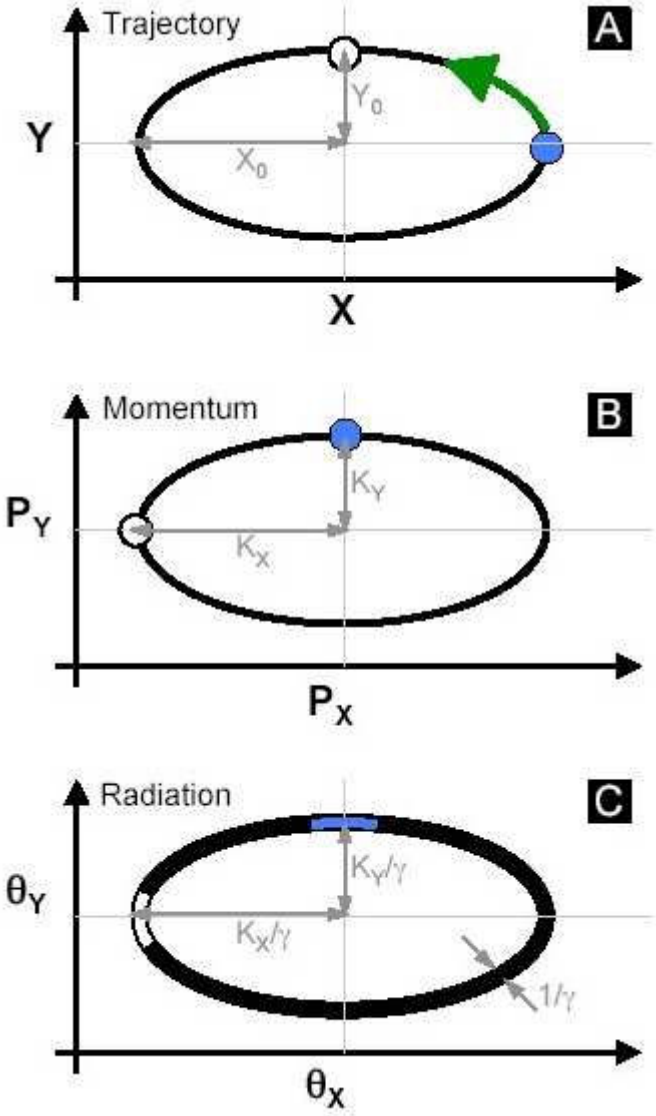

Figure 3.3: The correspondence between the electrons transverse trajectory, the transverse momentum and the distribution of betatron radiation. On (a) the symbols (circles) correspond to an arbitrary position. On figure (b), the same symbols correspond to the momenta. On figure (c) the line sections are the corresponding angular directions of the radiation emitted.

3.2 3D PIC simulation

3.2.1 Simulation parameters

In correspondence with the experiments performed at the Laborotorie d'Optique Appliquee [60] we carry out the computer simulation of laser plasma interaction using the particle-in-cell (PIC) code framework VLPL3D.

We assume that the laser wavelength $\lambda_0 = 2\pi/k_0 = 0.820\mu m$. We use a simulation box of dimension $(60 \times 88 \times 88)\lambda_0$ volume (x, y, z) cartesian geometry. It corresponds to the size of $(49\mu m \times 72\mu m \times 72\mu m)$. The direction of propagation is the x-axis. The number of gridpoints is $600 \times 176 \times 176 = 1.8 \cdot 10^7$. The resolution in the transverse direction is $k_{p_0}\Delta y = 0.26$, resolution in longitudinal direction is $k_{p_0}\Delta x = 0.05$, where $k_{p_0} = \omega_{p_0}/c$, $k_0/k_{p_0} = 11.95$, and $\omega_{p_0}^2 \equiv 4\pi e^2 n_0/m$. We use eight macroparticles / cell.

Parameters for numerical simulation were chosen in correspondance with values of physical parameters in the performed experiment. The laser pulse is linearly polarized in the Y-direction, it is duration of $\tau_{CPA} = 30fs$ and intensity $I = 3 \cdot 10^{18} W/cm^2$ which corresponds to the normalised vector potential $a_0 \equiv eA/mc^2 = 1.5$. The laser pulse is Gaussian in the transverse direction. In the longitudinal direction it has the cosinusoidal profile. Focused spot size is $9\mu m$. The plasma density is $n_0 = 7 \cdot 10^{-3} \cdot n_{crit} = 1.16 \cdot 10^{19} cm^{-3}$.

The transverse plasma profile is uniform. The longitudinal plasma profile has density increasing from zero to n_0 over $60 - 670$ wavelengths, then density is uniform $n_0 = 10^{19} cm^{-3}$ till 3110 wavelengths, then decreasing to zero at 3720 wavelengths.

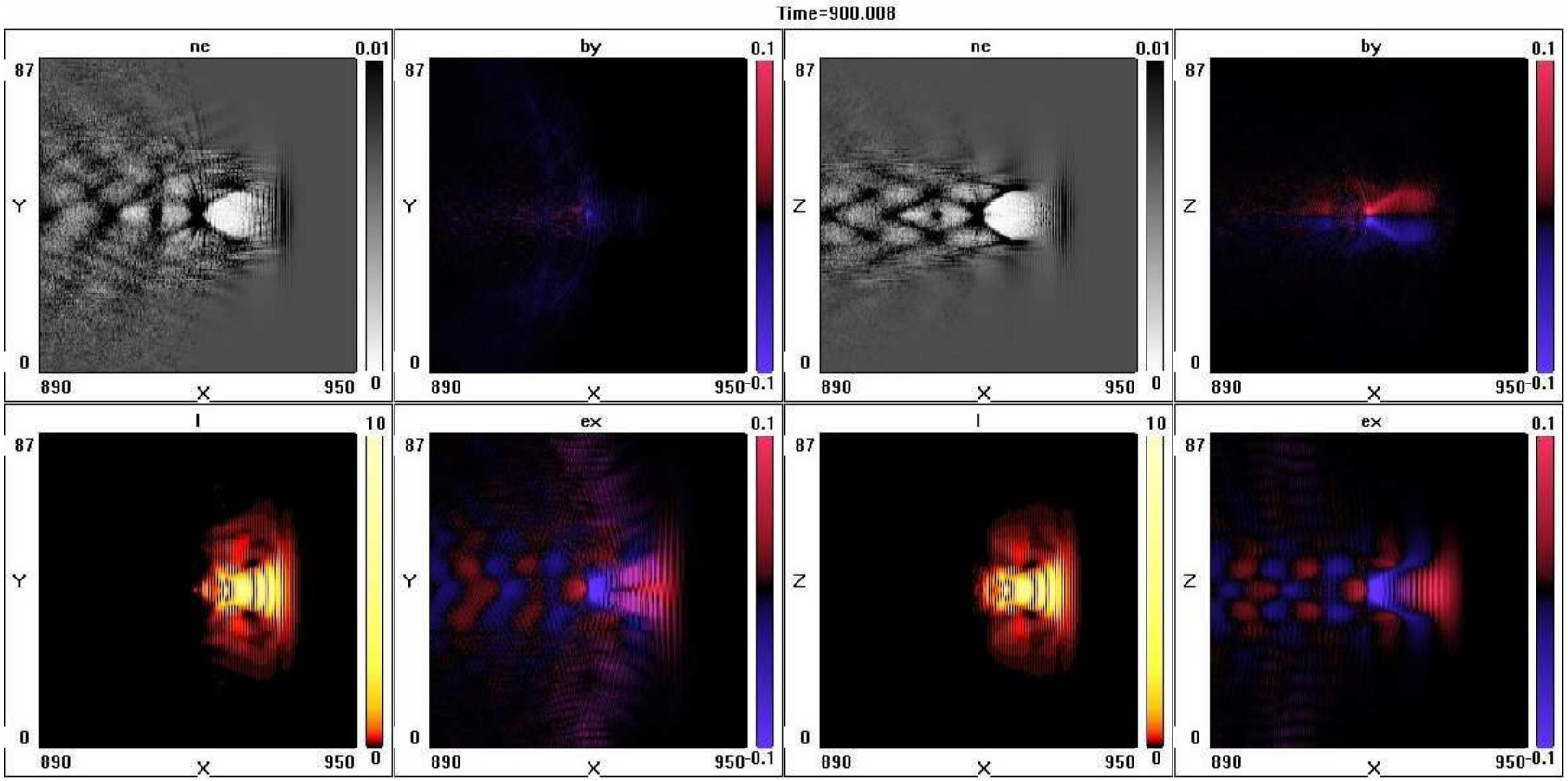

Figure 3.4: Graphical view of numerical simulation at time $T = 900$. The figure shows electron density(ne), intensity of the laser(I), magnetic field in Y-direction(by) and electric field in X-direction(ex) in planes $(X - Y)$ and $(X - Z)$. All coordinates given in the laser wavelengths λ_0.

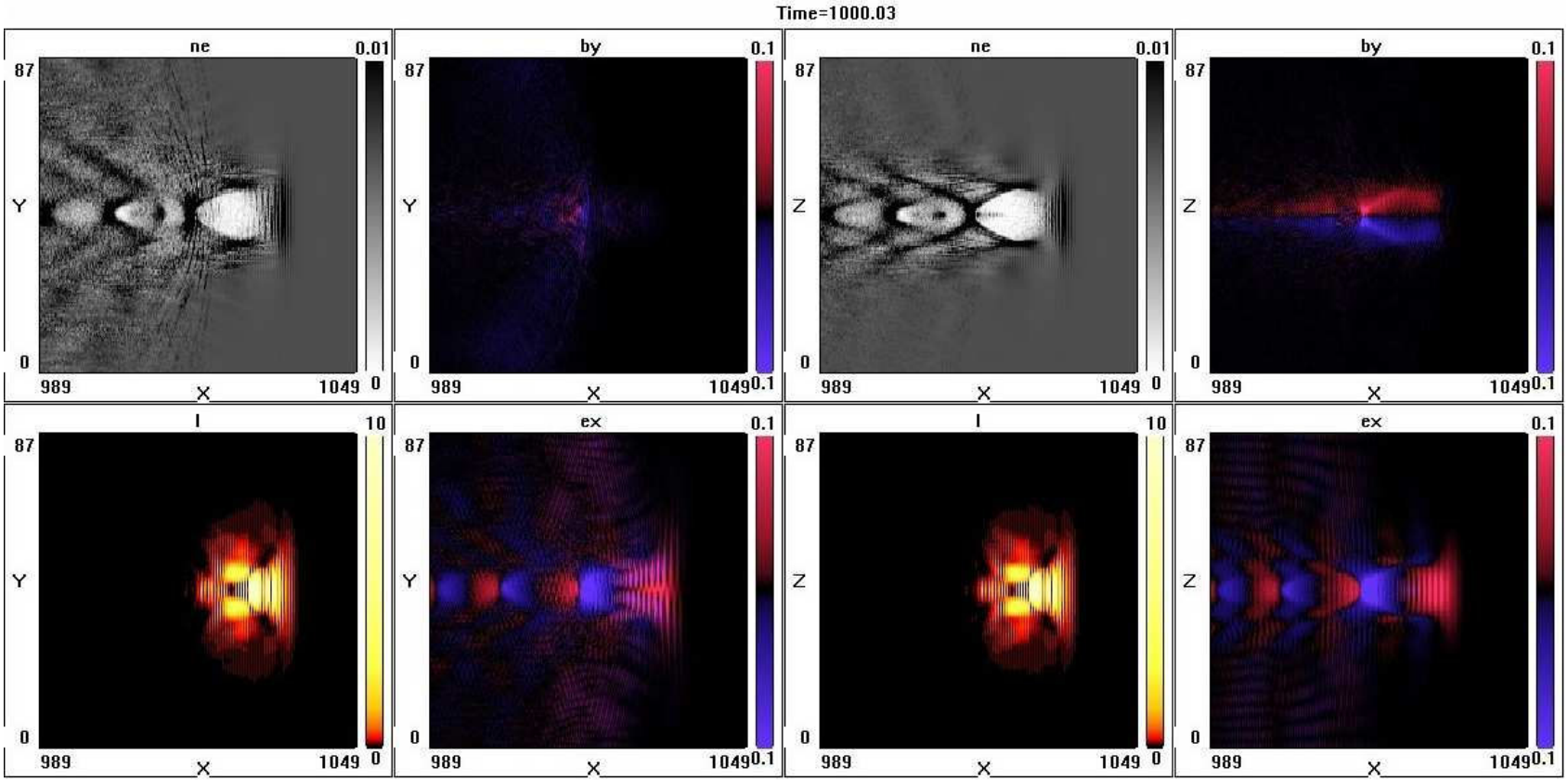

Figure 3.5: Graphical view of numerical simulation at time $T = 1000$. The figure shows electron density(ne), intensity of the laser(I), magnetic field in Y-direction(by) and electric field in X-direction(ex) in planes $(X - Y)$ and $(X - Z)$. All coordinates given in the laser wavelengths λ_0.

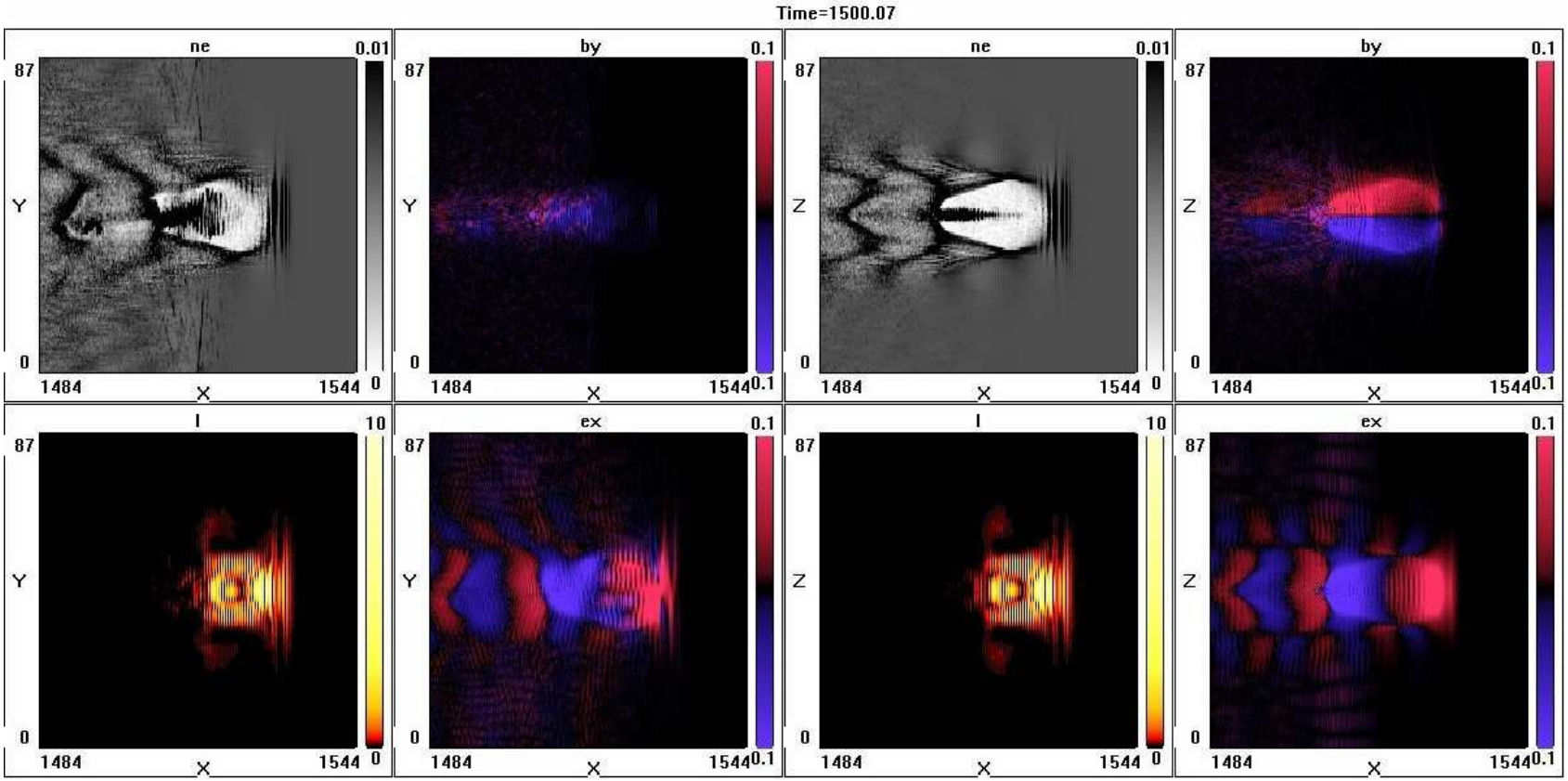

Figure 3.6: Graphical view of numerical simulation at time $T = 1500$. The figure shows electron density(ne), intensity of the laser(I), magnetic field in Y-direction(by) and electric field in X-direction(ex) in planes $(X - Y)$ and $(X - Z)$. All coordinates given in the laser wavelengths λ_0.

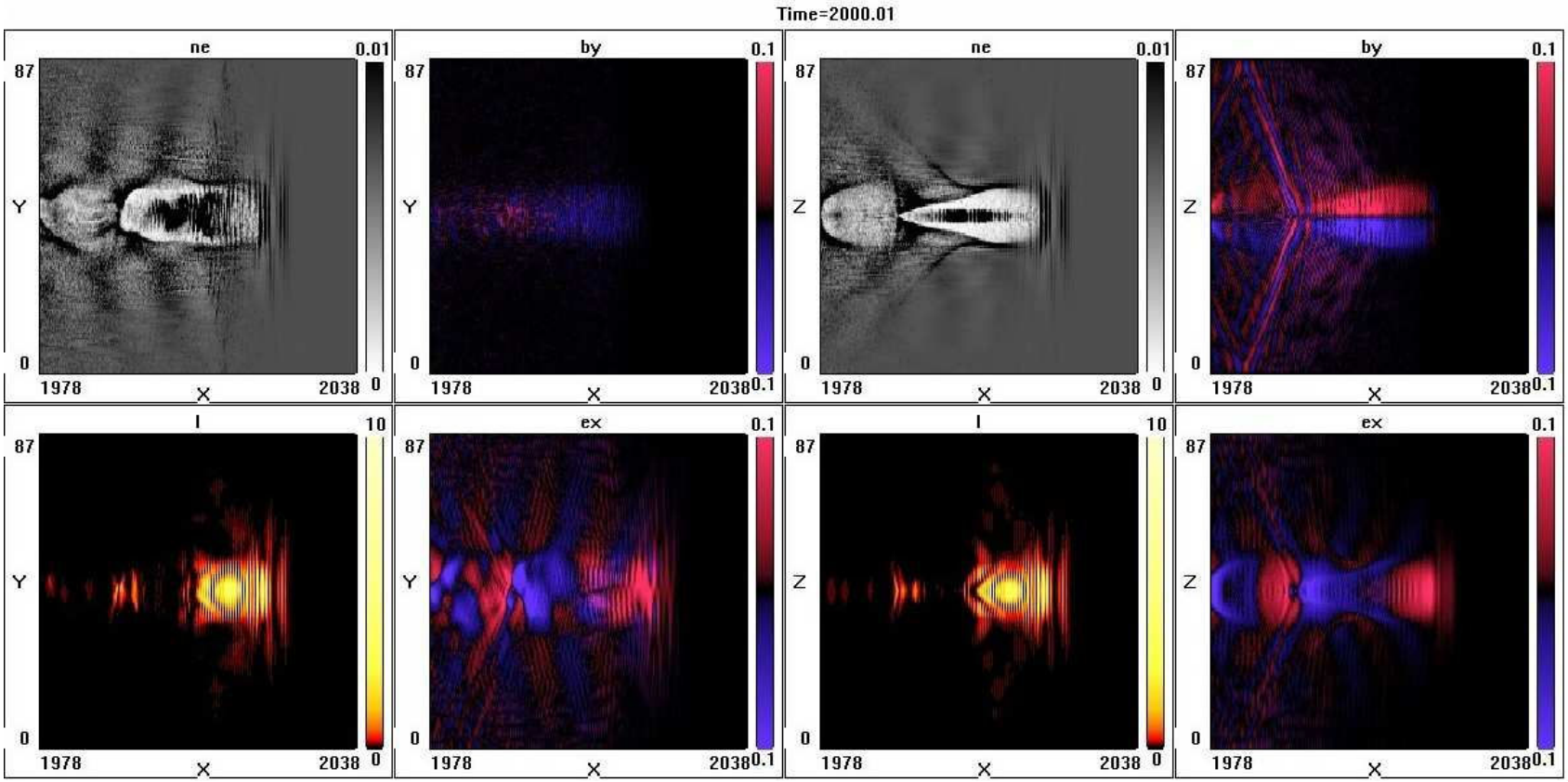

Figure 3.7: Graphical view of numerical simulation at time $T = 2000$. The figure shows electron density(ne), intensity of the laser(I), magnetic field in Y-direction(by) and electric field in X-direction(ex) in planes $(X - Y)$ and $(X - Z)$. All coordinates given in the laser wavelengths λ_0.

Figures (3.4)-(3.7) represent simulation results of laser pulse propagation in the plasma. Time is measured in the laser pulse period, $\tau = 2\pi/\omega$. It is seen that bubble was formed at time $T = 900$ laser periods. There are typical parts of bubble: front part of the bubble, sheath of electrons, wavebreaking area at back of the bubble and dense bunch of relativistic electrons in the middle of the bubble. It is seen from the Figures (3.4)-(3.7) that the front part of the electron bunch participates in betatron resonance with the laser pulse.

3.2.2 Trajectories of high energetic electrons

Using modification of VLPL PIC-code we have got more detailed information about the bubble evolution. Parameters of each particle for each time step were analyzed. The list of parameters contains: $(phase, x, y, z, px, py, pz, number, x_0, y_0, z)$, where *phase* is the time step, *number* is the unique label of particle, x_0, y_0, z_0 are the initial coordinates of particle.

Using postprocessing of described data we obtain directly the image of electrons trajectories. Electrons with the highest energies were chosen. Fig. (3.8) represents examples of trajectories of electrons. Direction of laser pulse propagation is the X-axis. Trajectories are given in projection on the plane $(Y - Z)$. The form of trajectories is comparable with the theoretically predicted form (3.2). The stretch of trajectories in the Y-direction corresponds to the laser pulse polarization along the Y-axis. All coordinates are given in laser wavelengths.

Further we restrict the data for postprocessing by the area in the middle of bubble where the electron bunch is positioned. At the time $T = 2000$ laser periods, the electron bunch is located in volume $(1998 - 2018)\lambda \times (41 - 47)\lambda \times (41 - 47)\lambda$, where λ is laser wavelength. By initial conditions the background plasma density is $n_e = 7 \cdot 10^{-3} n_{crit} = 10^{19} cm^{-3}$, therefore the simulation area contains about 10^{12} electrons. The volume which contains the electron bunch measured in laser wavelength is $V_{bunch} = 10\lambda \times 8\lambda \times 8\lambda$. The volume of simulation measured in laser wavelength is $V_{total} = 60\lambda \times 88\lambda \times 88\lambda$.

$$V_{bunch}/V_{total} \sim 10^{-3} \ . \tag{3.33}$$

The density of the electron bunch is greather than the average plasma density, therefore the electron bunch contains not less than 10^9 electrons. The part of electron bunch which remains behind the laser pulse is located in volume $(1998 - 2008)\lambda \times (41 - 47)\lambda \times (41 - 47)\lambda$. The part of electron bunch which is in betatron resonance with the laser pulse is located in volume $(2008 - 2018)\lambda \times (41 - 47)\lambda \times (41 - 47)\lambda$. Further this areas are postprocessed separately.

The Figures (3.9)-(3.10) represent some typical trajectories of electrons. All trajectories are given in projection on plane $(Y - Z)$. Figure (3.9) represents trajectories of electrons only from back part of electron bunch. Trajectories shown in this Figure have form which is close to circle. Figure (3.10) represents trajectories of electrons only from the front part of the electron bunch. Trajectories shown in this Figure have elliptical form strongly strethed in the Y-direction. The reasons of such form are the betatron

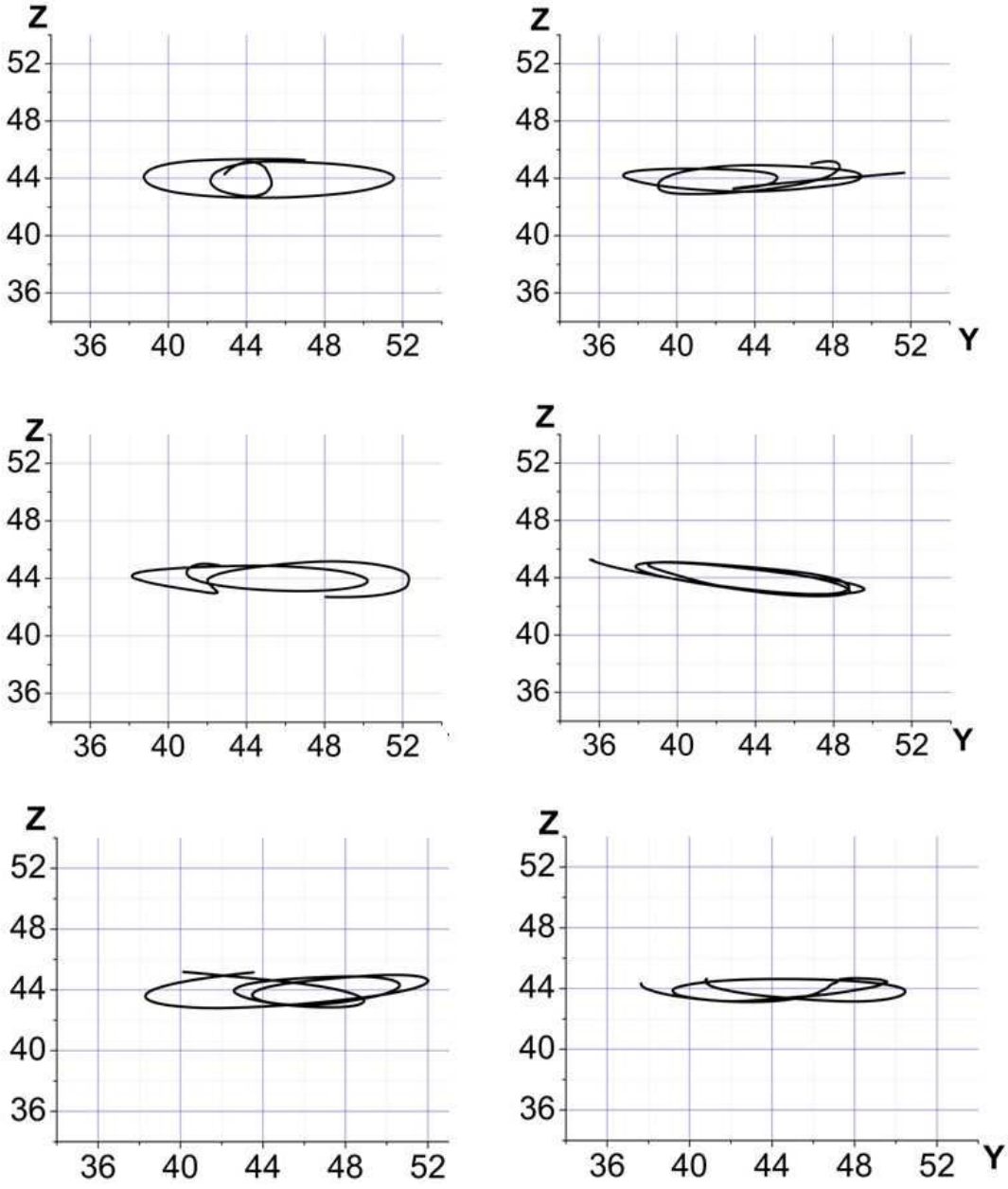

Figure 3.8: Trajectories of some electrons from group of particles with highest energy over all area of simulation.

resonance and the laser polarization along Y-axis.

The Figures (3.11)-(3.12) represent trajectories of the electrons in three dimensions. Using unique labels of each particle, the Figures show trajectories of exactly the same electrons from previous Figures (3.9)-(3.10). All coordinates are given in laser wavelengths.

The condition for producing the stream of data about each particle is liminal energy of this particle. It means that the information about a particle is accessible only with the condition that the energy of this particle is greater than $150MeV$. For this reason each trajectory has the start point at a definite x-coordinate from which the energy of the electron exceeds the energy limit $150MeV$. The simulation has finished at the time $T = 2000$ of laser periods. For this reason any trajectory can not finish in the point with coordinate greater than $x = 2000$ laser wavelengths. The area of simulation has sizes 88λ in both directions which are perpendicular to the direction of the laser propagation. In Figures the axis in the middle of the simulation area corresponds to the point with coordinates $(y = 44, z = 44)$.

The Figure (3.11) represents trajectories of electrons from the back part of the electron bunch, where betatron resonance is not presented. The trajectories have the form of a helix around the axis of laser pulse propagation in accordance with the Figure (3.2, A).

The Figure (3.11) represents trajectories of electrons from the front part of the electron bunch, where the betatron resonance occurs. The trajectories become flat in the Z-direction and stretched in the Y-direction in accordance with the Figure (3.2, A). The decreasing of the amplitude of electrons trajectories along the Z-direction is explained by the linear polarization of the laser pulse. The axis of the laser pulse propagation corresponds to the axis $(x, 44, 44)$ in shown Figures. It is seen from the Figures that electrons are moving around the axis of the laser pulse propagation.

3.2.3 Distribution of electrons capture

Changes in the VLPL3D PIC-code allow us to produce information about each electron which is in the simulation box. One block of the data contains tvelve variables: $(phase, x, y, z, p_x, p_y, p_z, N, x_0, y_0, z_0)$, where $phase$ is time measured in the laser periods(τ), (x, y, z) are current coordinates of the particle, (p_x, p_y, p_z) are momentum of the particle, $unique_number$ is the unique label of the particle, (x_0, y_0, z_0) are initial coordinates of the particle. Such the group of parameters can be defined for each particle in the simulation area at any moment of time. However we do not need to describe all particles. In the VLPL3D PIC-code we can restrict the information stream by electrons which are energetic enough. Only the electrons with energy greater than $150MeV$ were processed. The simulation was performed with MPI(message passing interface) with partitioning $12 \times 4 \times 4$ in $X-, Y-, Z-$axis correspondingly.

Therefore there are 192 subvolumes of the area of numerical simulation. For each subvolume there is a stream of data which is saving in the file with the name corresponding to the number of the subvolume.

For further postprocessing of data from the VLPL3D PIC-code we have developed the program on C++ on the Linux platform. The program contains three group of

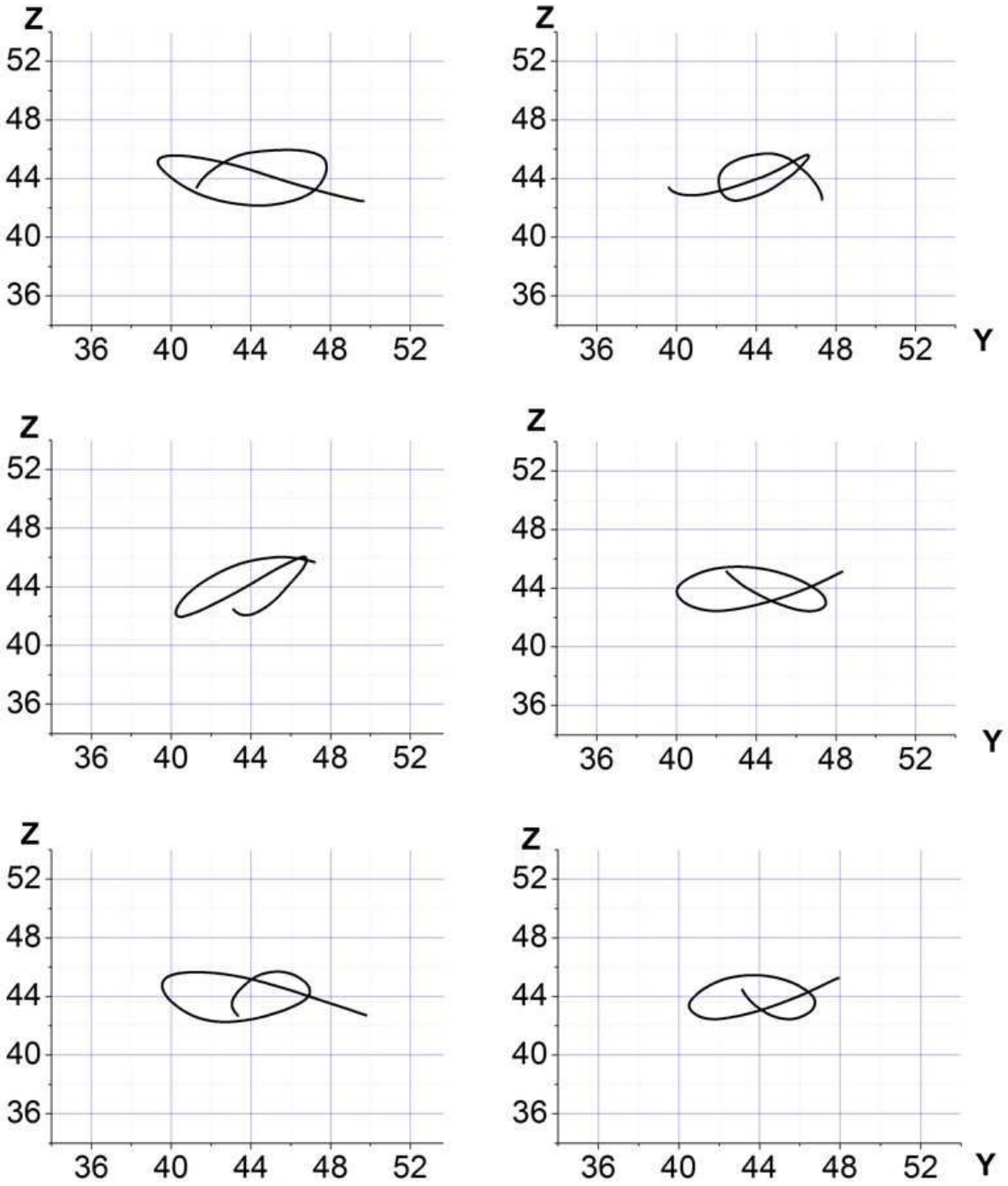

Figure 3.9: Trajectories of some of the most high energetic electrons from the back part of electron bunch.

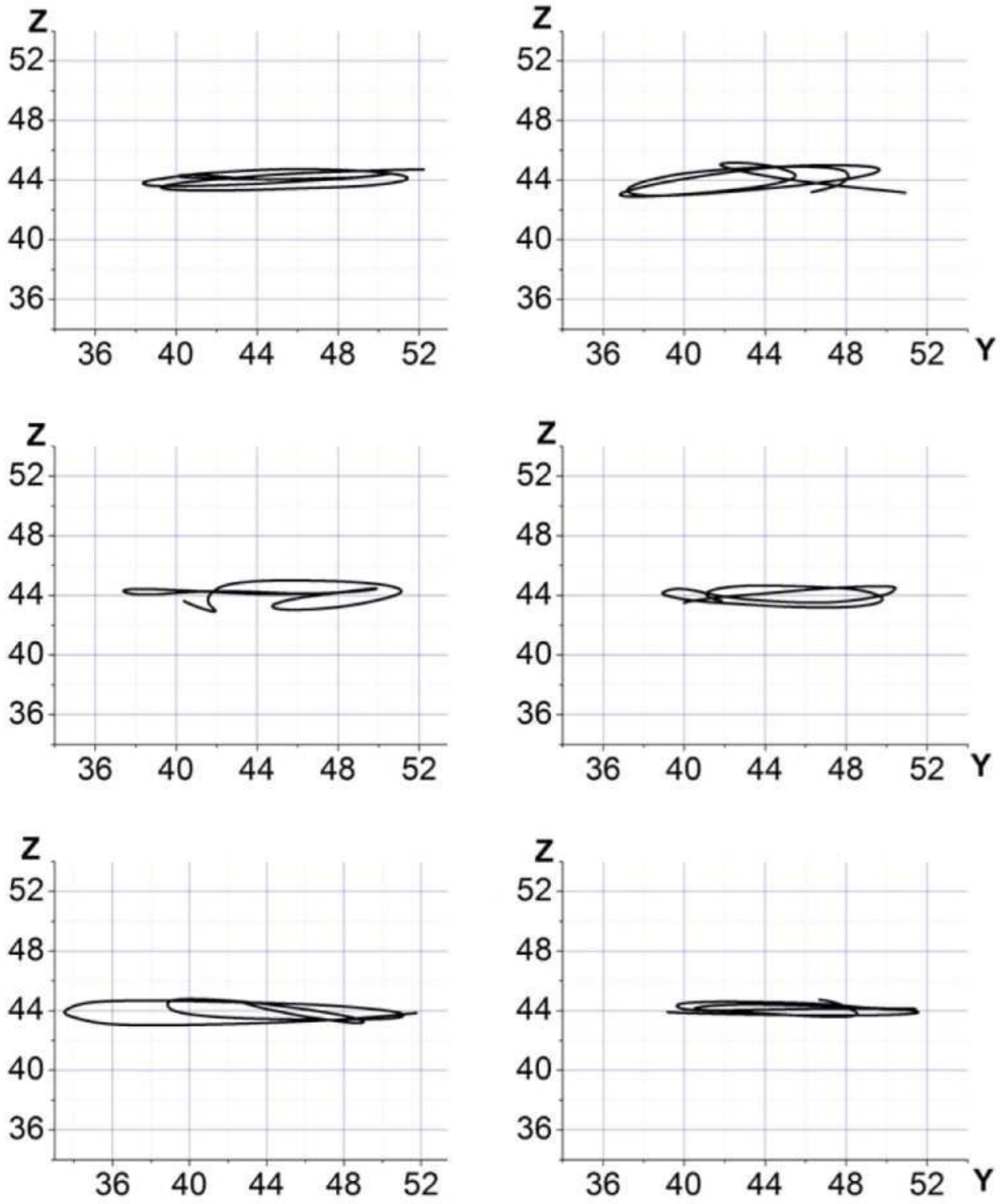

Figure 3.10: Trajectories of some of the most high energetic electrons from the front part of electron bunch.

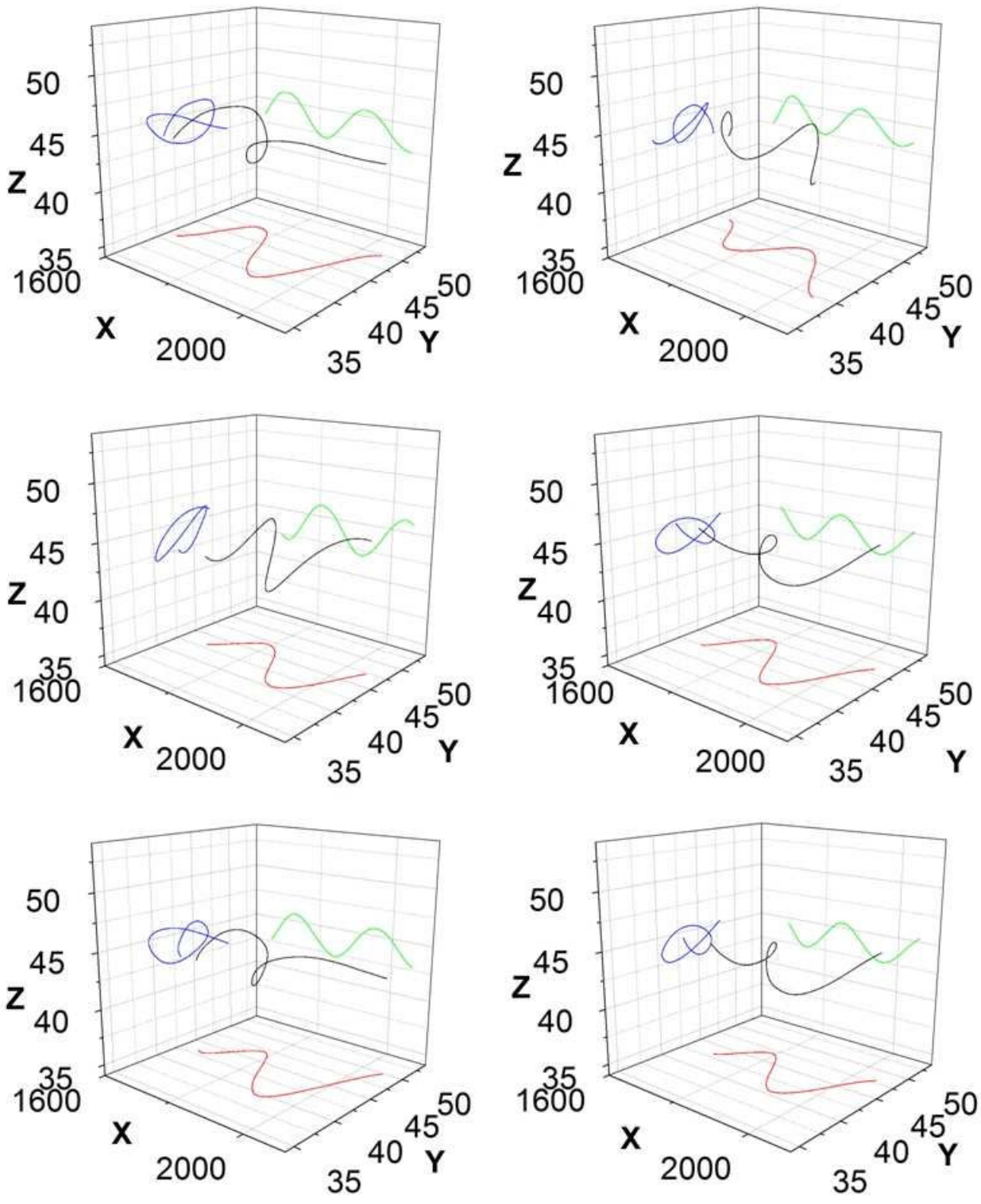

Figure 3.11: Trajectories of some of the most energetic electrons from the back part of the electron bunch.

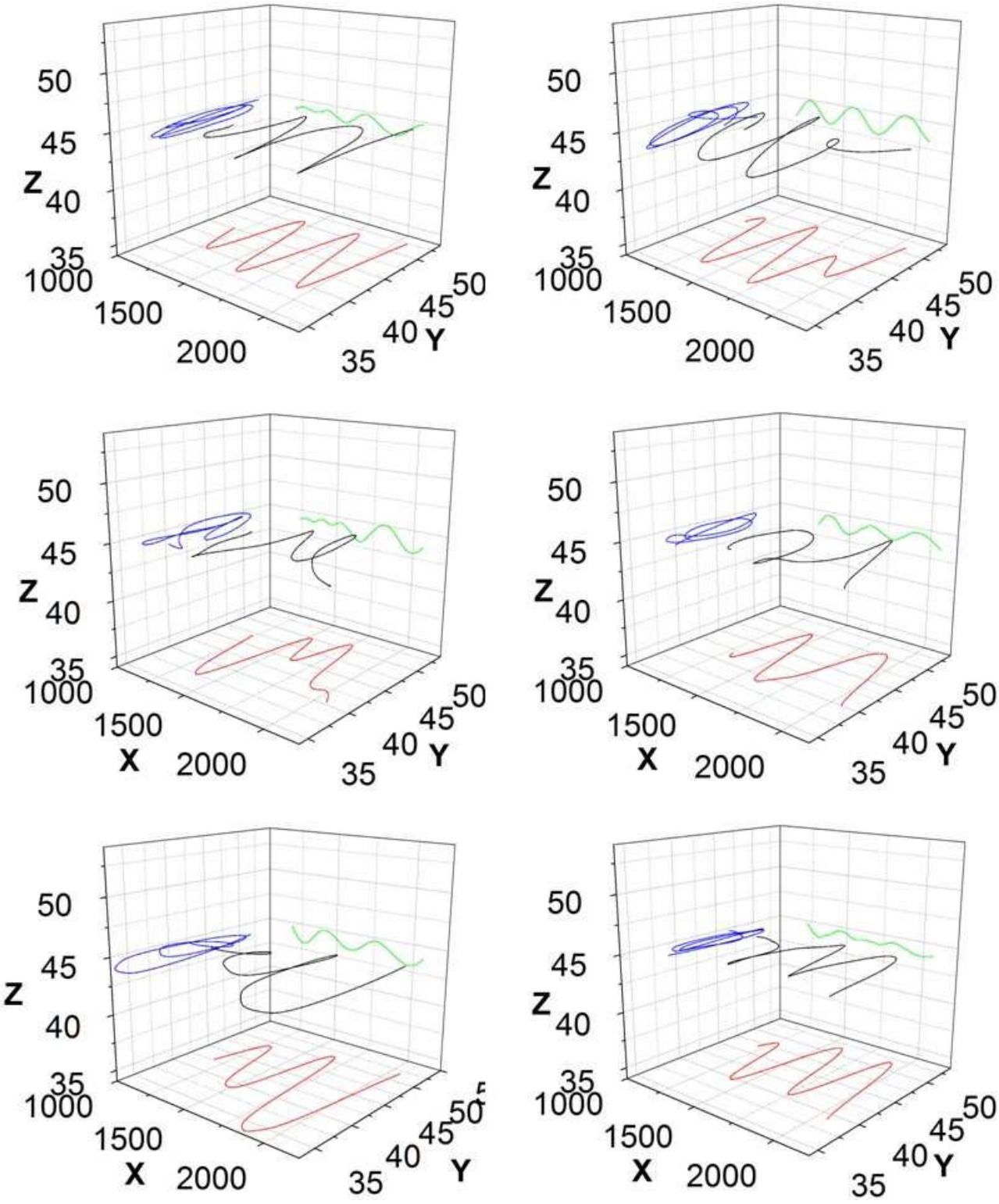

Figure 3.12: Trajectories of some of the most energetic electrons from the front part of the electron bunch.

functions.

The first group of functions is responsible for correct work with files. The program automatically determines the number of files. The structure of the block of reading can be changed in dependence of the structure of the block of data from the VLPL3d PIC-code. The quantity of blocks for the one time processing depends from the available computer memory. By default the number of blocks of reading is 10 millions.

The second group of functions is responsible for work with the volume of data. Different functions using various kinds of the sorting and transformation of blocks of the data to produce several distributions. The function for the calculation of the trajectories of particles stays separately in this group. This function has been constructed with using the unique label of the particle.

Third group of functions is responsible for producing the final results. The result is files in standard format which can be further processed by any mathematical software. In the case of the calculation of the particles trajectories corresponding function is responsible for the selection of data which describe only marked particles from the volume of data.

The Figure (3.13) represents the picture of the capture of electrons in three dimensional form. The Figure has been made with using described program. The program has determined initial coordinates for each electron with the energy which is greater than $150MeV$ at the moment of time $T = 2000$ of laser periods. The "initial" coordinates of a particle means the point where the acceleration of the electron has started.

It is seen from the Figure that area of the capture of electrons has the form of a dilative funnel with the axis along the Z-direction. It is demonstrating that particles, which are located in the electron bunch, initially were moved into wavebreaking area from the electron sheath of the bubble. The form of the area of capture corresponds to the form of bubble in the Figure (3.7). This picture of the capture of electrons is in accordance with conclusions of the phenomenological theory, the Figure (3.1).

From projections on planes $(X-Z)$ and $(X-Y)$ we can conclude that the asymmetry of the area of capture is explained by the horizontal polarization of the laser pulse.

After the bubble has formed, the laser pulse and the wavebreaking area became separated in space. The size of the area of capture increases along the Z-direction with time because the laser polarization is losing influence on the process of capture.

The Figures (3.14)-(3.16) represent the distribution of the gamma-factor of captured electrons in dependence from the x_0-coordinate of capture at three different moments of time. It seen from the Figures that at the moment of time $T = 1000$ the capture of particles with energy above $150MeV$ starts at the x-coordinate about 600 laser wavelengths.

To the moment of time $T = 1500$ (Figure (3.15)) the large number of electrons from the group of particles, which were captured in the initial period($x_0 = (600 - 1000)$ of laser wavelengths), decrease the energy less than $150MeV$. The largest number of electrons is located in the area $x_0 = (1200 - 1300)$ of laser wavelengths. It is seen from the Figure (3.15) that for the moment of time $T = 1500$ of laser periods electrons with the initial x_0-coordinates till 1300 of laser wavelengths are presented. Therefore

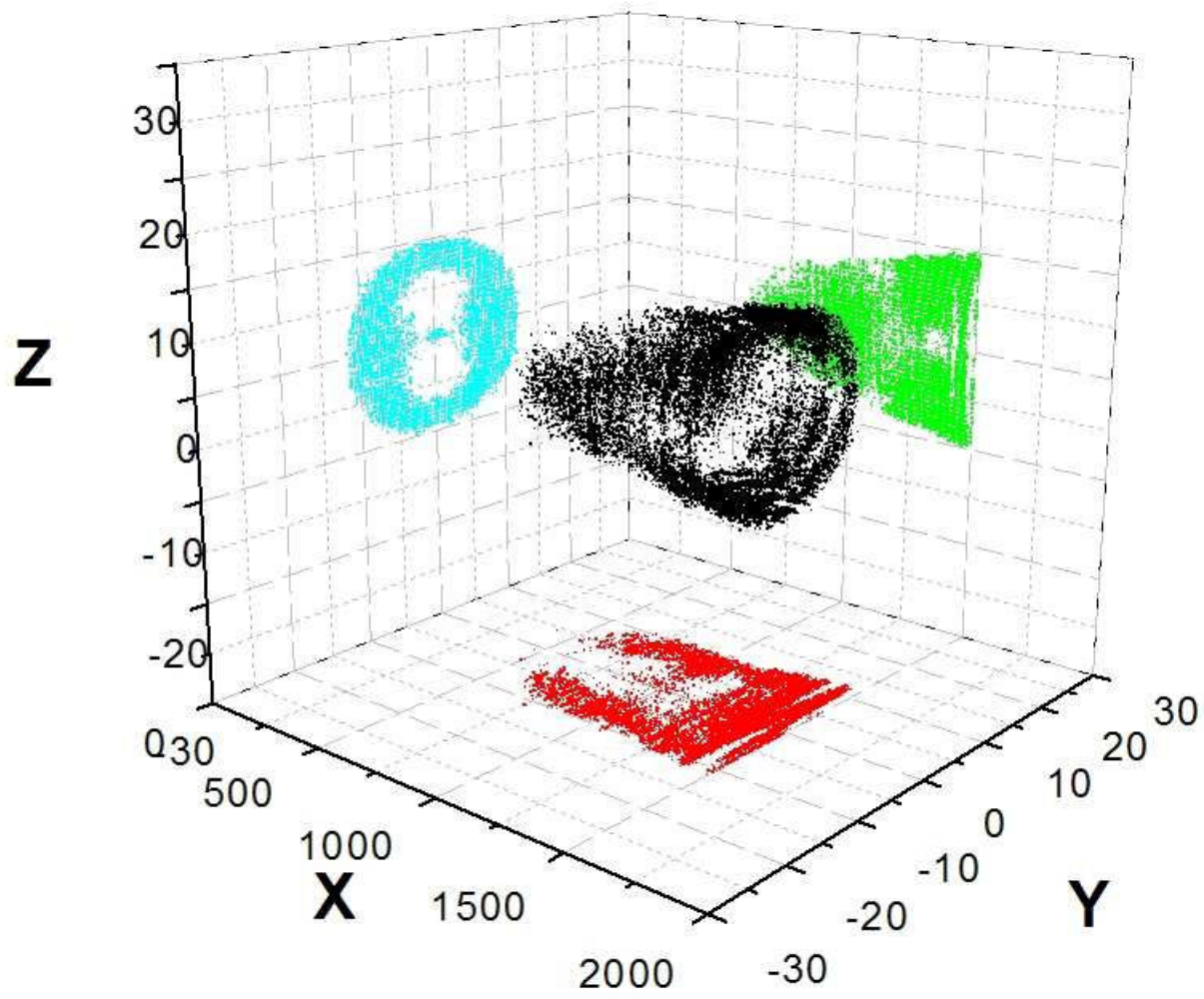

Figure 3.13: Initial positions of accelerated electrons. The X-axis is the direction of the laser pulse propagation. Zeros of perpendicular coordinates correspond to the axis of the laser pulse propagation, the middle of the simulation area. The picture was taken at the moment of time $T = 2000$ laser periods.

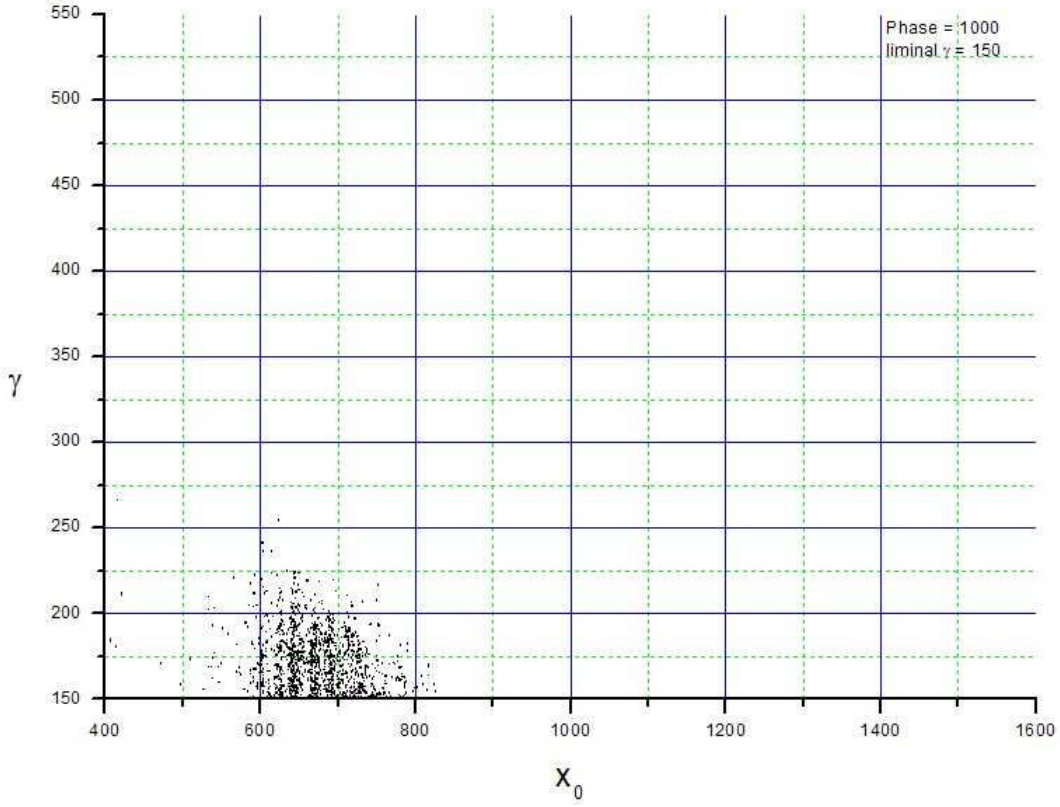

Figure 3.14: The distribution of the gamma-factor of electrons in the dependence from the x-coordinate of the capture. Only particles which have the energy above $150MeV$ are included in distribution. The distribution taken at the moment of time $T = 1000$ of laser wavelengths. The Figure is presented for the case of linear polarization.

electrons have been accelerated up to $150MeV$ during the range about 200 of laser wavelengths. For the next hundred of laser wavelengths the considerable part of electrons get additional energy about $100MeV$. Some part of electrons which are shown on the Figure, has the energy about $300 - 450MeV$. Electrons which have been accelerated during about 500 of laser wavelengths have the maximum of the energy about $450MeV$. The averaged acceleration rate is $\sim 1MeV/\lambda$.

The Figure (3.16) represents the distribution of the gamma-factor of captured electrons in the dependence from the x_0-coordinate of the capture at the moment of time $T = 2000$ laser periods. It is seen from the Figure (3.16) that at the moment of time $T = 2000$ there are no electrons with the x_0-coordinate of the capture, which is greater than $x_0 = 1500$ laser wavelengths. In the period of $(1300 - 1800)$ laser wavelengths the process of capture of electrons has been stop.

The Figure (3.17) represents the distribution of current x-coordinates of electrons in the dependence from the x_0-coordinate of capture at the moment of time $T = 2000$. It is seen from the Figure that the majority of particles is located in the area which can be approximated by a line. The line describes defined relation between the coordinate and

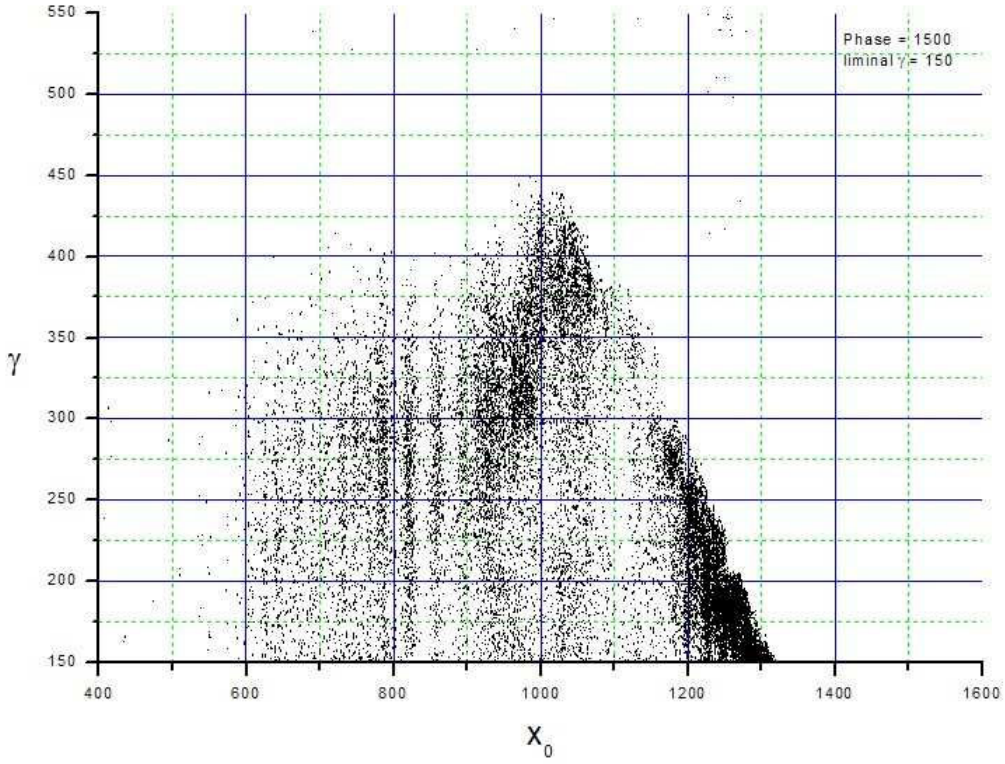

Figure 3.15: The distribution of the gamma-factor of electrons in the dependence from the x-coordinate of the capture. Only particles which have the energy above $150MeV$ are included in distribution. The distribution taken at the moment of time $T = 1500$ of laser wavelengths. The Figure is presented for the case of linear polarization.

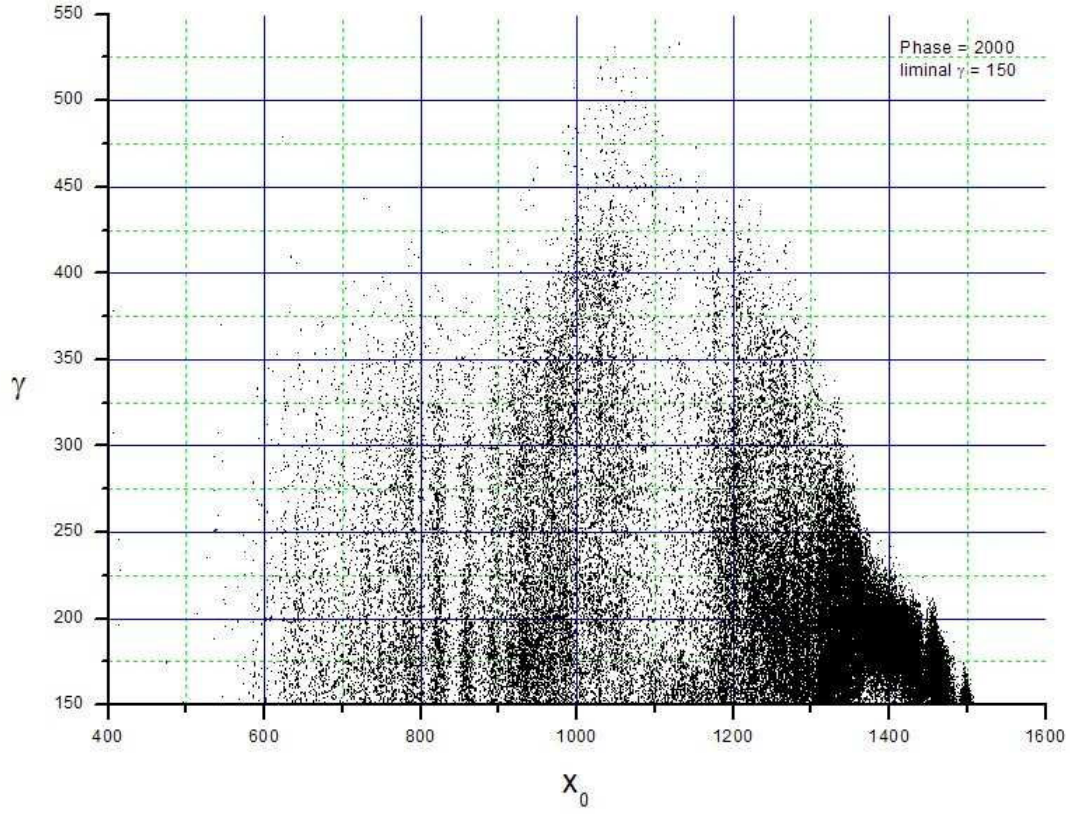

Figure 3.16: The distribution of the gamma-factor of electrons in the dependence from the x-coordinate of the capture. Only particles which have the energy above $150MeV$ are included in distribution. The distribution taken at the moment of time $T = 2000$ of laser wavelengths. The Figure is presented for the case of linear polarization.

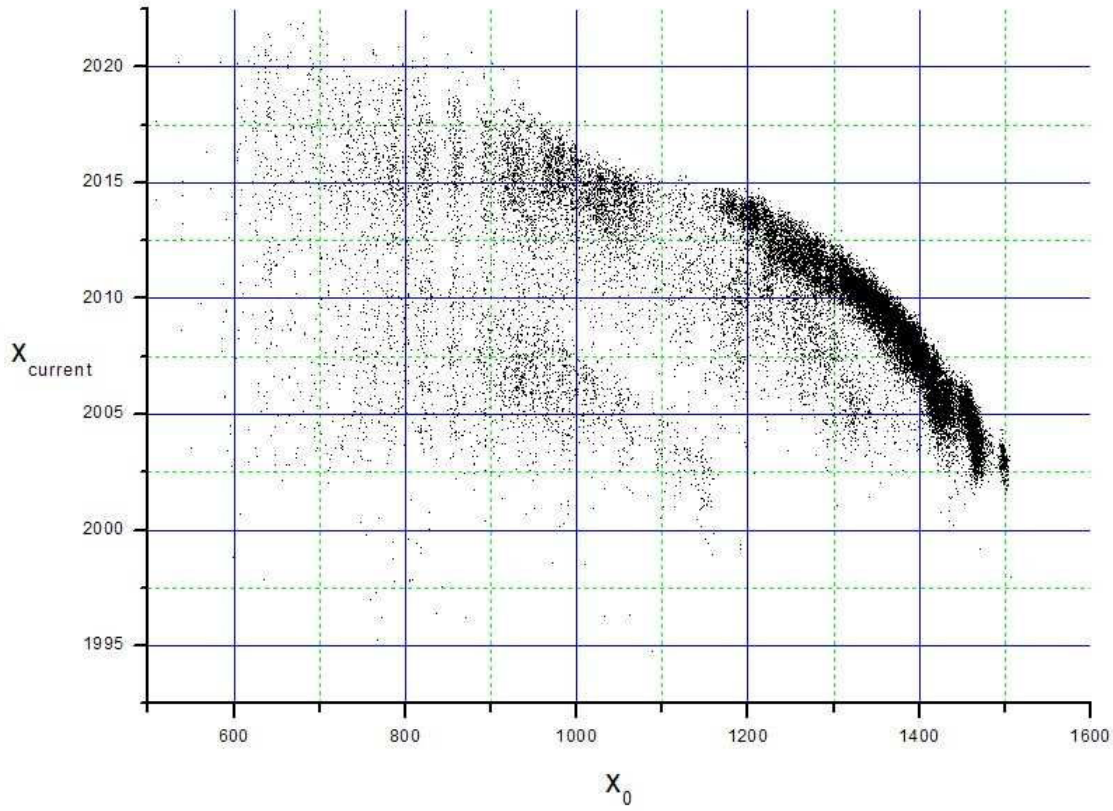

Figure 3.17: The distribution of current x-coorginates of electrons in the bubble in the dependence from the coordinate of the capture. The data were taken at the moment of time $T = 2000$ of laser wavelengths.

the point of capture of a particle. Electrons which were captured at early times, have greater current coordinates. Therefore inside the electron bunch particles are moving from the back part to the front part. The angle of slope of this approximation line shows the velocity of the moving of electrons inside the electron bunch. Also from the Figure we can conclude that by the moment of time $T = 2000$ the majority of electrons which are presented in the electron bunch was captured in the area of the x-axis $(1200 - 1500)$ of laser wavelengths. The electron bunch has approximately size of 15 of laser wavelengths along the x-axis, what corresponds to the Figure (3.7).

The Figure (3.32) represents the dependence of the number of captured electrons from the location of the point of the capture at three different moments of time. Resolution along x-axis is 0.5 of the laser wavelength.

The x-axis was separated on ranges of 0.5 of the laser wavelength. For each of ranges the Figure (3.32) represents the number of electrons which were captured in this range of the x-coordinate.

The distribution shown in the Figure includes only electrons with energy above $150MeV$. Three graphs, shown in the Figure at three different moments of time, are

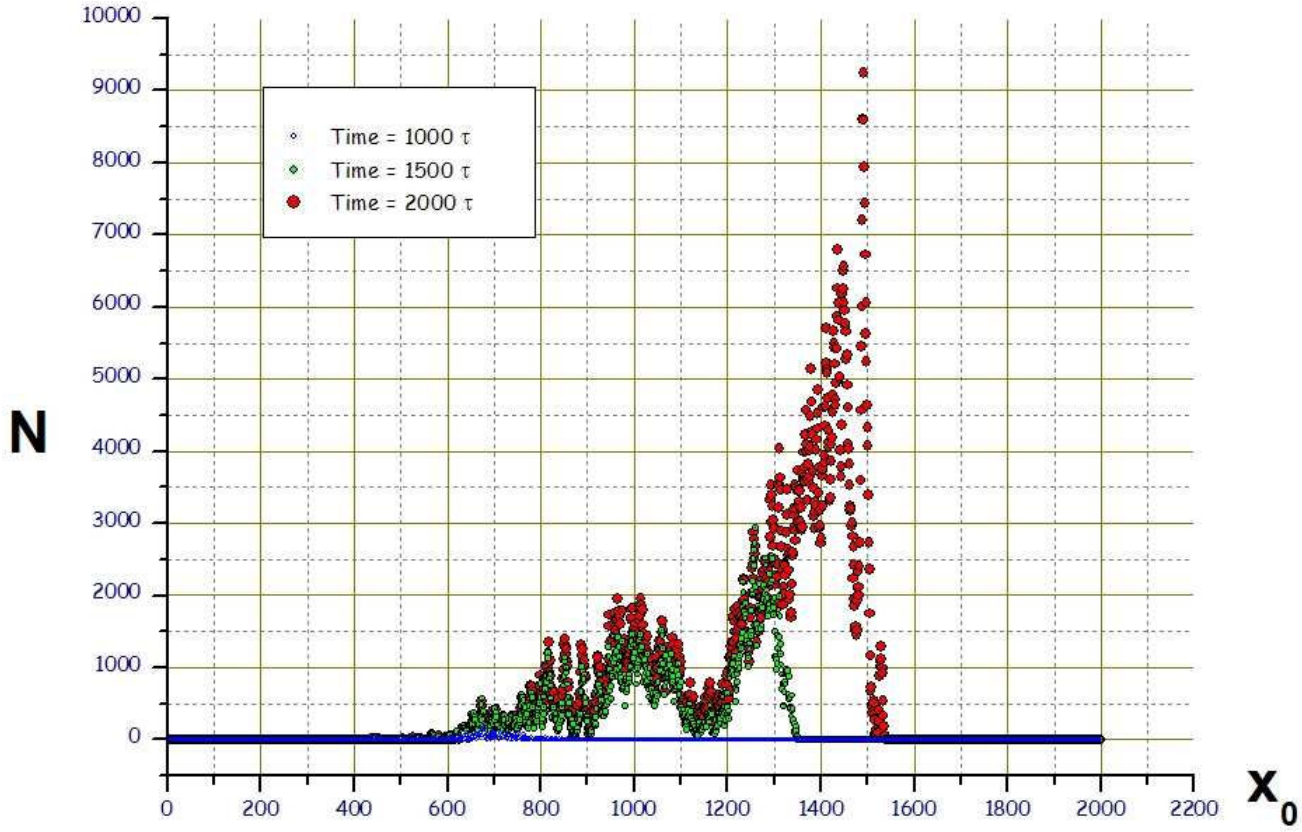

Figure 3.18: The distribution of the number of captured electrons in the dependence from the x-coordinate of the capture. The distribution shown at three different moments of time: $T = 1000$ of laser period (blue), $T = 1500$ of laser periond (green) and $T = 2000$ of laser period (red). The Figure is presented for the case of linear polarization. For each of three cases were taken only those particles which had the energy above $150MeV$ at corresponding moment of time.

not completely identic in the area $(500 - 1300)$ of laser wavelengths. Unsignificant difference in graphs in range of $(500-1300)$ of laser wavelengths is explained by changes in energies of electrons. The Figure demonstrates complicated and unregular dynamics of the process of capture of electrons.

3.3 The case of circular polarization

3.3.1 Trajectories of particles

The additional numerical simulation was performed for the understanding improvement of the evolution of the bubble.

With exception of the kind of polarization all other initial conditions are equal to parameters of the previous simulation. The kind of polarization has been changed from

linear on circular polarization.

The forming and the evolution of the bubble are shown in Figures (3.19)-(3.22). The bubble has similar form in both of two planes $(X-Y)$ and $(X-Z)$. It is seen from Figures that formed bubble has greater sizes along all axis of coordinates. Circularly polarized laser pulse has two times greater energy in comparison with the linearly polarized laser pulse. The size of bubble, how it is seen in the Figure (3.22), has increased on $\sim 30\%$ along each of three dimensions in comparison with the previous case with the linear polarization. Therefore it can be concluded that size of the bubble is proportional to the energy of the laser pulse.

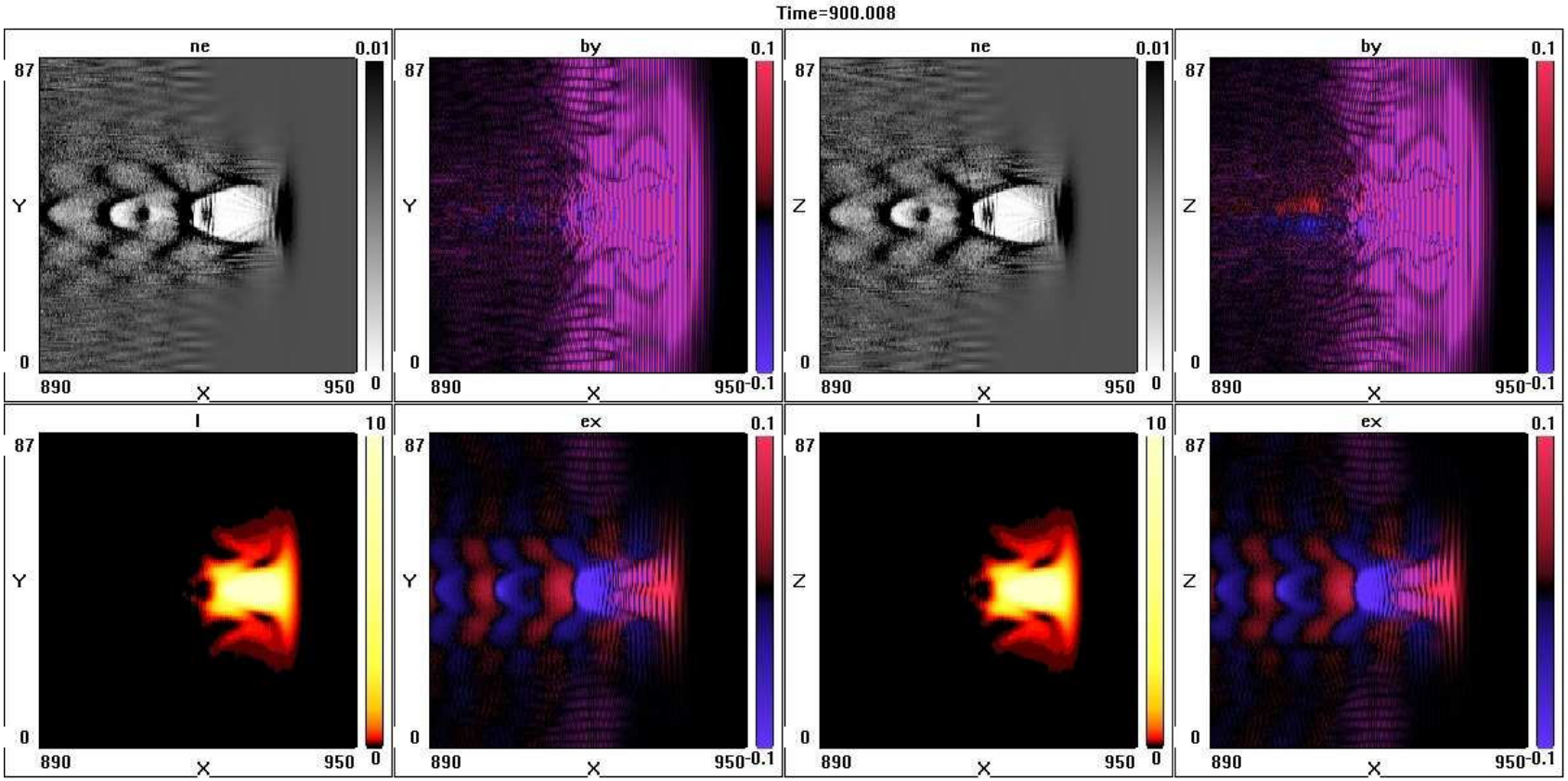

Figure 3.19: Graphical view of numerical simulation at time $T = 900$. The figure shows electron density(ne), intensity of the laser (I), magnetic field in Y-direction(by) and electric field in X-direction(ex) in planes $(X - Y)$ and $(X - Z)$. All coordinates given in the laser wavelengths.

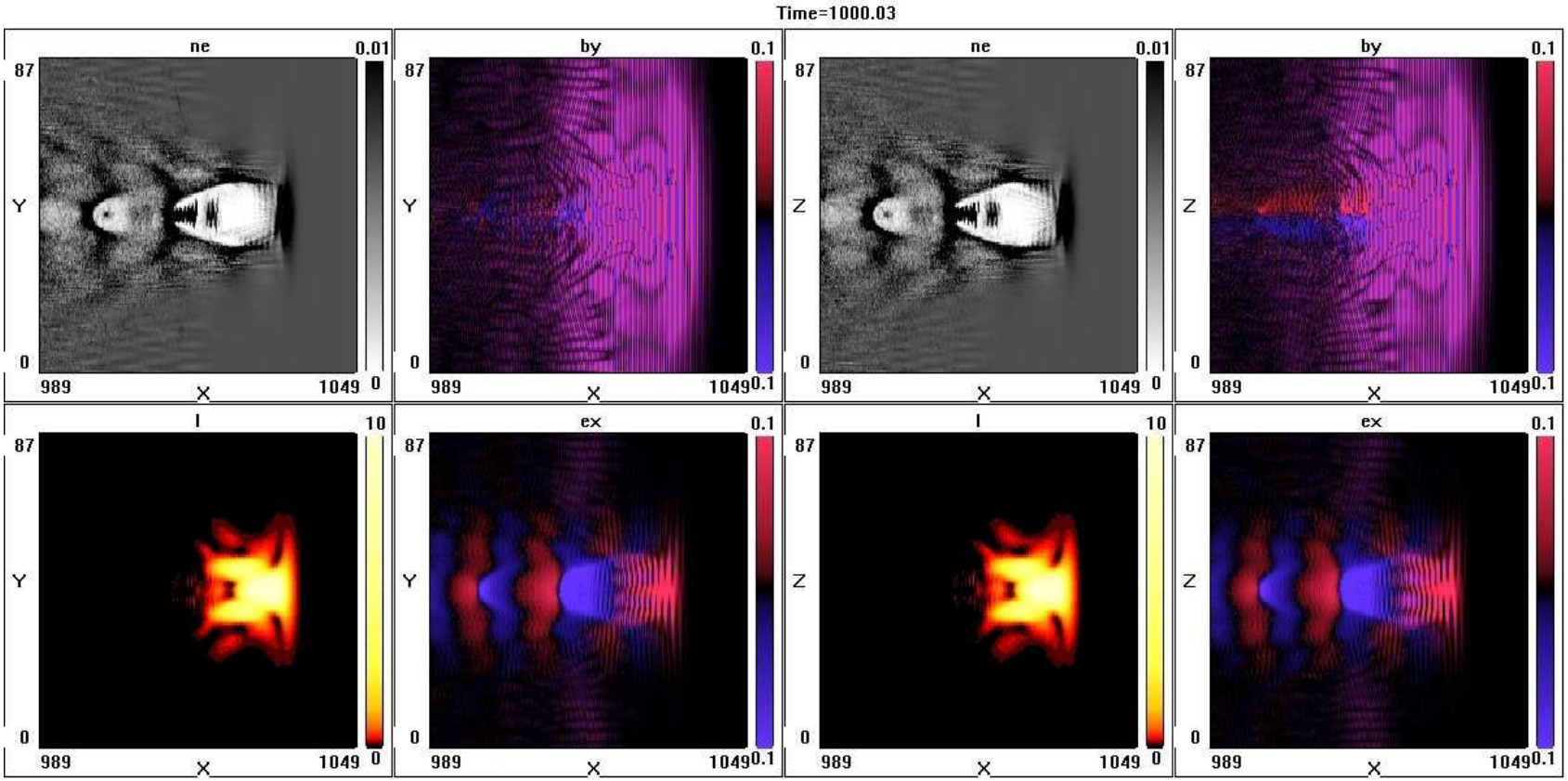

Figure 3.20: Graphical view of numerical simulation at time $T = 1000$. The figure shows electron density(ne), intensity of the laser (I), magnetic field in Y-direction(by) and electric field in X-direction(ex) in planes $(X - Y)$ and $(X - Z)$. All coordinates given in the laser wavelengths.

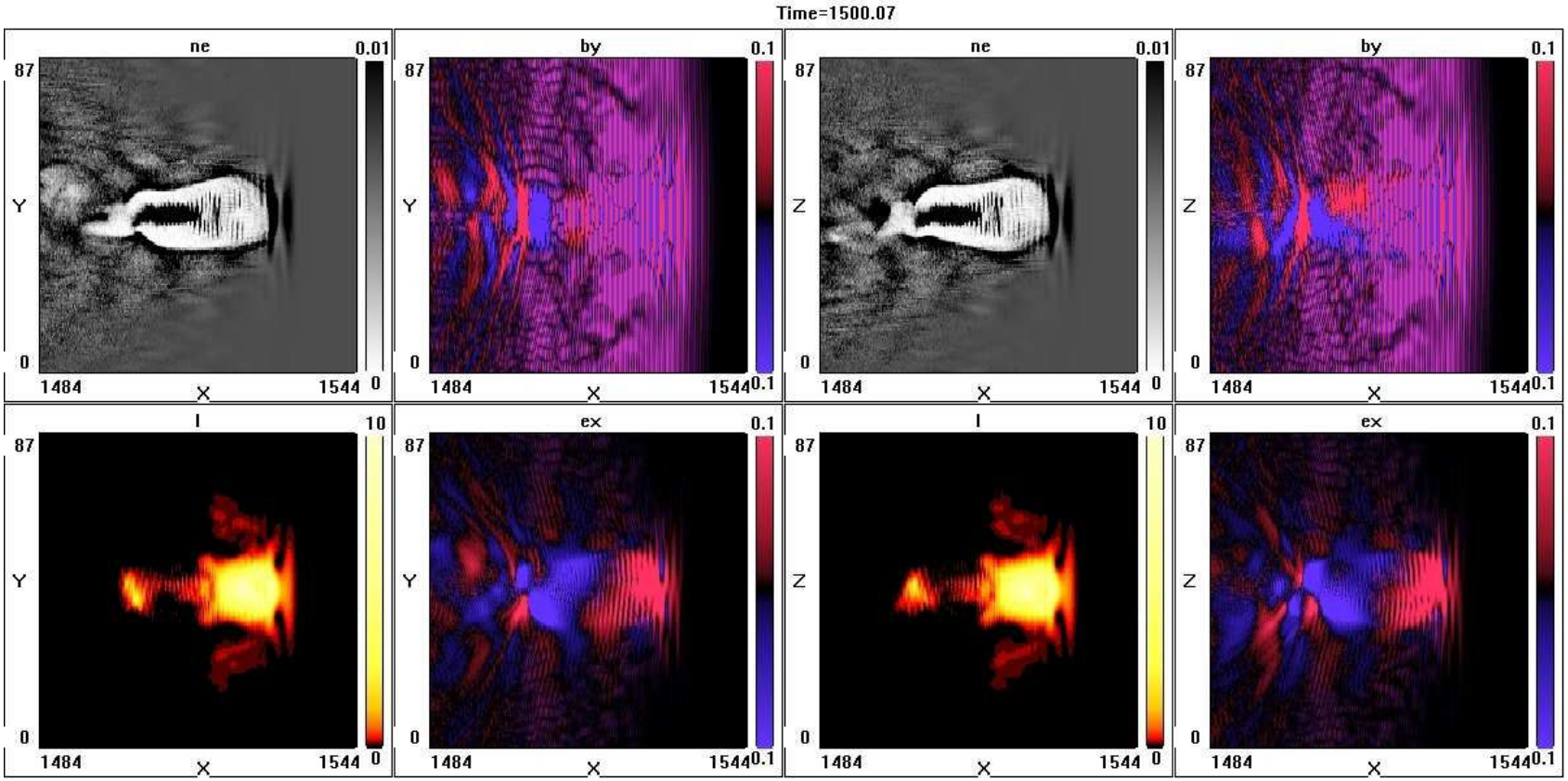

Figure 3.21: Graphical view of numerical simulation at time $T = 1500$. The figure shows electron density(ne), intensity of the laser (I), magnetic field in Y-direction(by) and electric field in X-direction(ex) in planes $(X - Y)$ and $(X - Z)$. All coordinates given in the laser wavelengths.

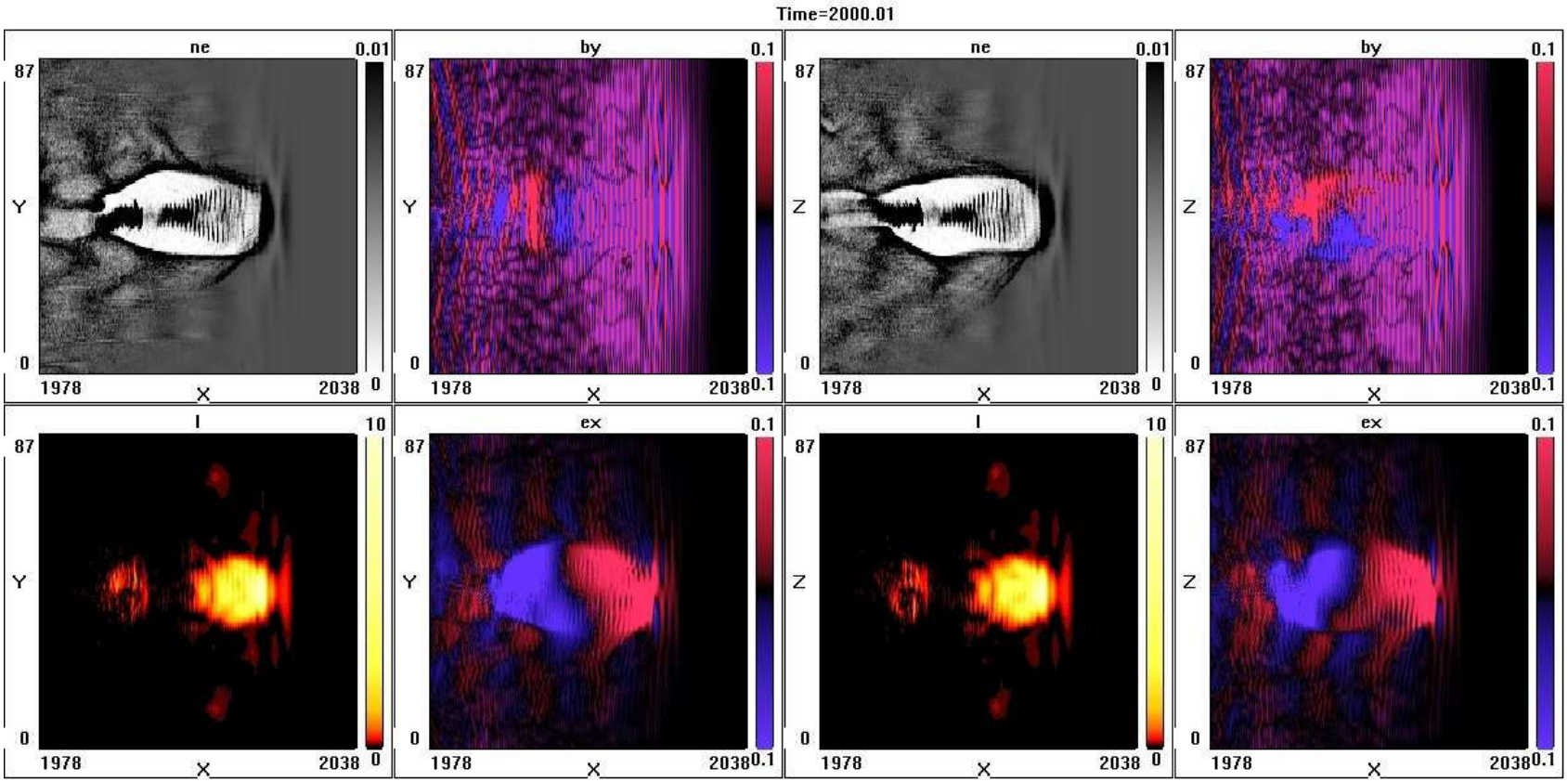

Figure 3.22: Graphical view of numerical simulation at time $T = 2000$. The figure shows electron density(ne), intensity of the laser (I), magnetic field in Y-direction(by) and electric field in X-direction(ex) in planes $(X - Y)$ and $(X - Z)$. All coordinates given in the laser wavelengths.

Figures (3.23)-(3.24) represent trajectories of electrons in the plane $(Y - Z)$. We consider separately the part of the electron bunch which is located behind of the laser pulse. The Figure (3.23) represents trajectories of electrons from the back part of the electron bunch in the plane $(Y-Z)$. The Figure (3.24) represents trajectories of electrons from the front part of the electron bunch, which participate in the betatron resonance. Trajectories shown in the Figure (3.23) have greater sizes in the perpendicular directions. Here trajectories of electrons from the front part of the electron bunch keep the form which is comparable with a circle. It confirms that the kind of the polarization have the main influence on the form of trajectories. The selection of the most energetic electrons was performed at the moment of time $T = 2000$ of laser periods. All coordinates are given in laser wavelengths. In Figures (3.23)-(3.24) the location of the axis of the laser pulse propagation corresponds to the point $(y = 44, z = 44)$.

Figures (3.25)-(3.26) represent trajectories of same electrons in three dimensions. The Figure (3.25) corresponds to the back part of the electron bunch. The Figure (3.26) corresponds to the front part of the electron bunch. Particles from the front part of the electron bunch have energies above $150MeV$ during longer time period in the comparison with electrons from the back part. Trajectories of electrons which are shown on the Figure (3.26) are more unregularly. The selection of the most energetic electrons was performed at the moment of time $T = 2000$ of laser periods. All coordinates are given in laser wavelengths. On Figures the axis in the middle of simulation area located at values of perpendicular coordinates $(x, 44, 44)$.

3.3.2 The capture of electrons in the bubble

The Figure (3.27) represents the picture of the capture of electrons which is analogous to the Figure (3.13). The difference is only in the kind of polarization, the Figure (3.27) corresponds to the circular polarization of the laser pulse. In the Figure are shown only those electrons which were presented at the moment of time $T = 2000$ with the energy above $150MeV$. The area of capture of electrons has greater perpendicular sizes in the correspondence with increased sizes of the bubble. It is seen from the Figure that the area of capture has cylidrical form. In the correspondence with analytical description the capture of electrons occurs in the area of electrons sheath of the bubble. The process of capture has been stoped during ~ 400 of laser wavelengths from $x \simeq 1300$ of laser wavelengths till $x \simeq 1700$ of laser wavelengths. The process of capture occurs only with the condition which we can see in the graphical part of the numerical simulation of the laser pulse propagation. The capture of electrons occurs until the dense electron bunch is not located directly in front of wavebreaking area. Only with the area of free space between the wavebreaking area and the back of the electron bunch the process of capture takes place.

Figures (3.28)-(3.30) represent the distribution of the gamma-factor of captured electrons in the dependence from the x_0-coordinate of capture at three different moments of time. These Figures correspond to times $T = 1000$, $T = 1500$, $T = 2000$ of laser periods. From Figures we can conclude that the capture and acceleration of electrons occur unregularly.

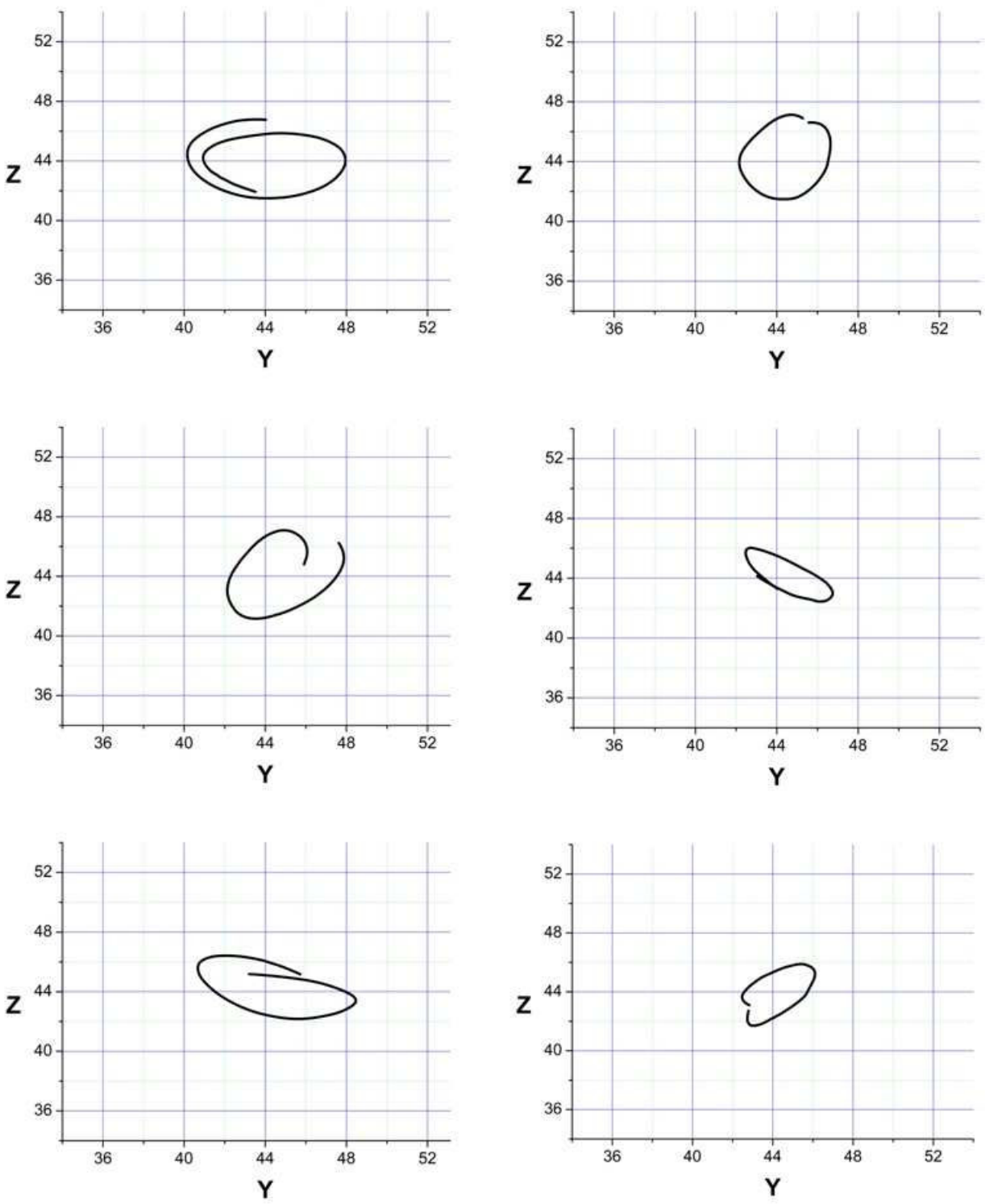

Figure 3.23: Trajectories of some of the most energetic electrons from the back part of the electron bunch.

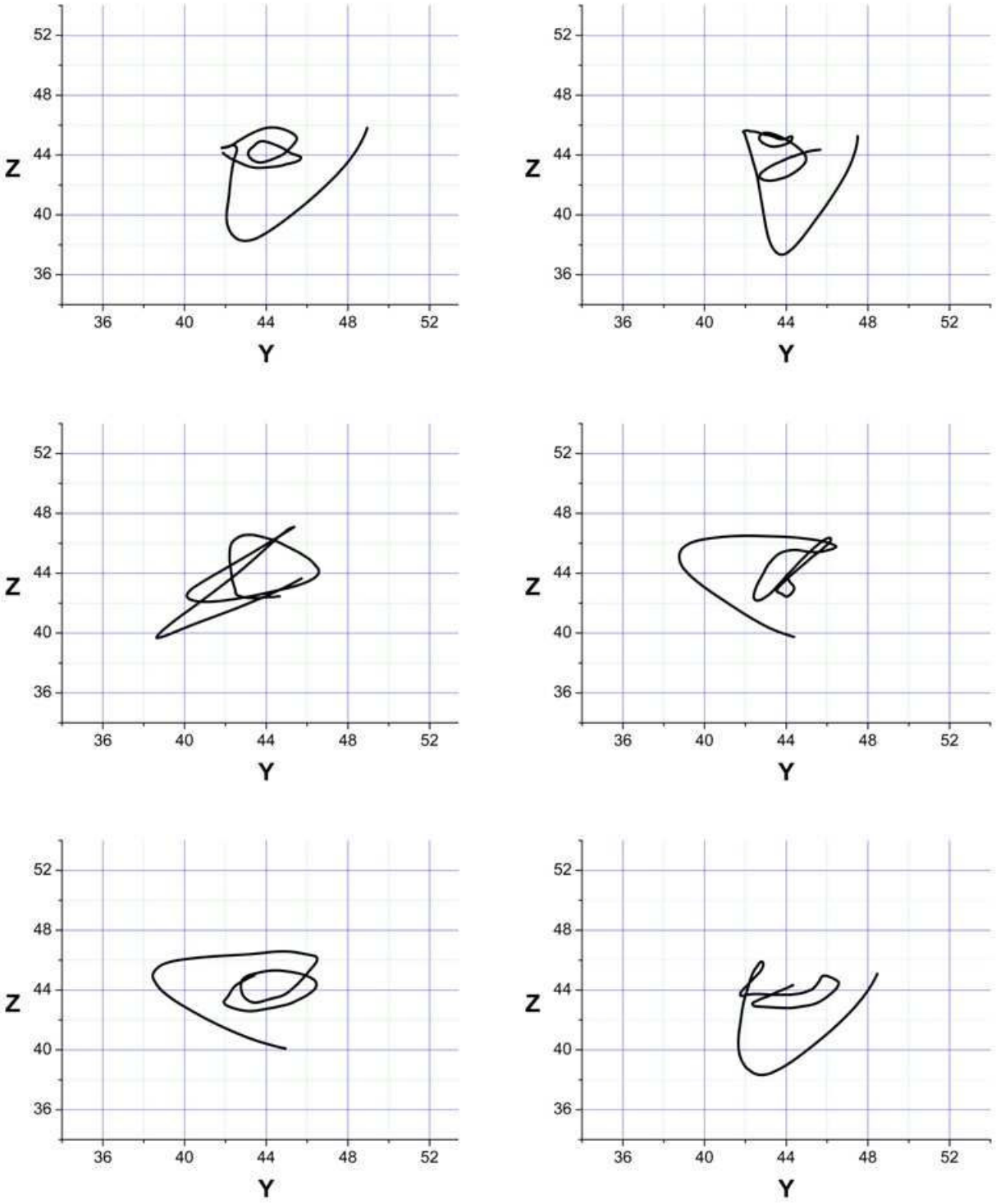

Figure 3.24: Trajectories of some of the most energetic electrons from the front part of the electron bunch.

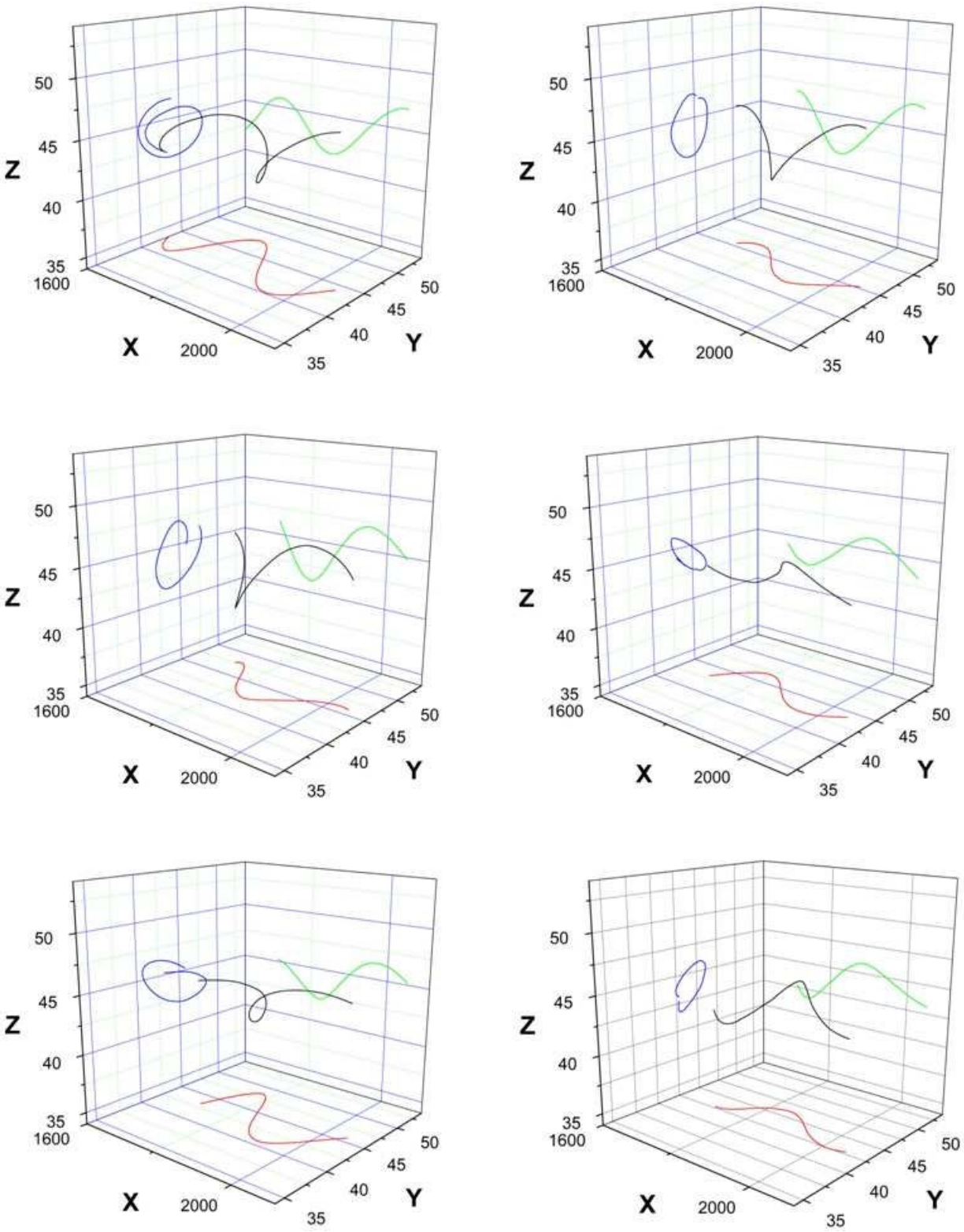

Figure 3.25: Trajectories of some of the most energetic electrons from the back part of the electron bunch.

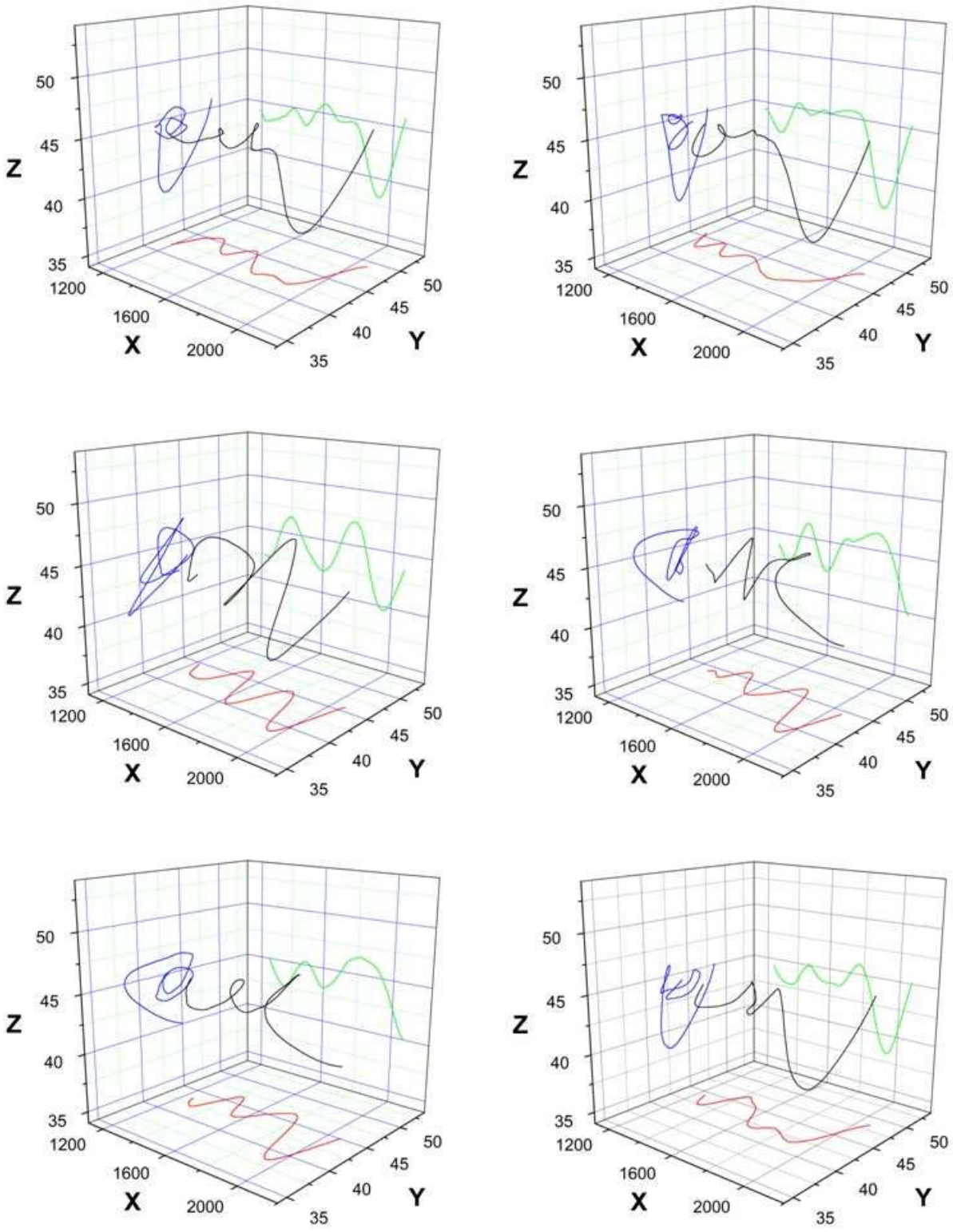

Figure 3.26: Trajectories of some of the most energetic electrons from the front part of the electron bunch.

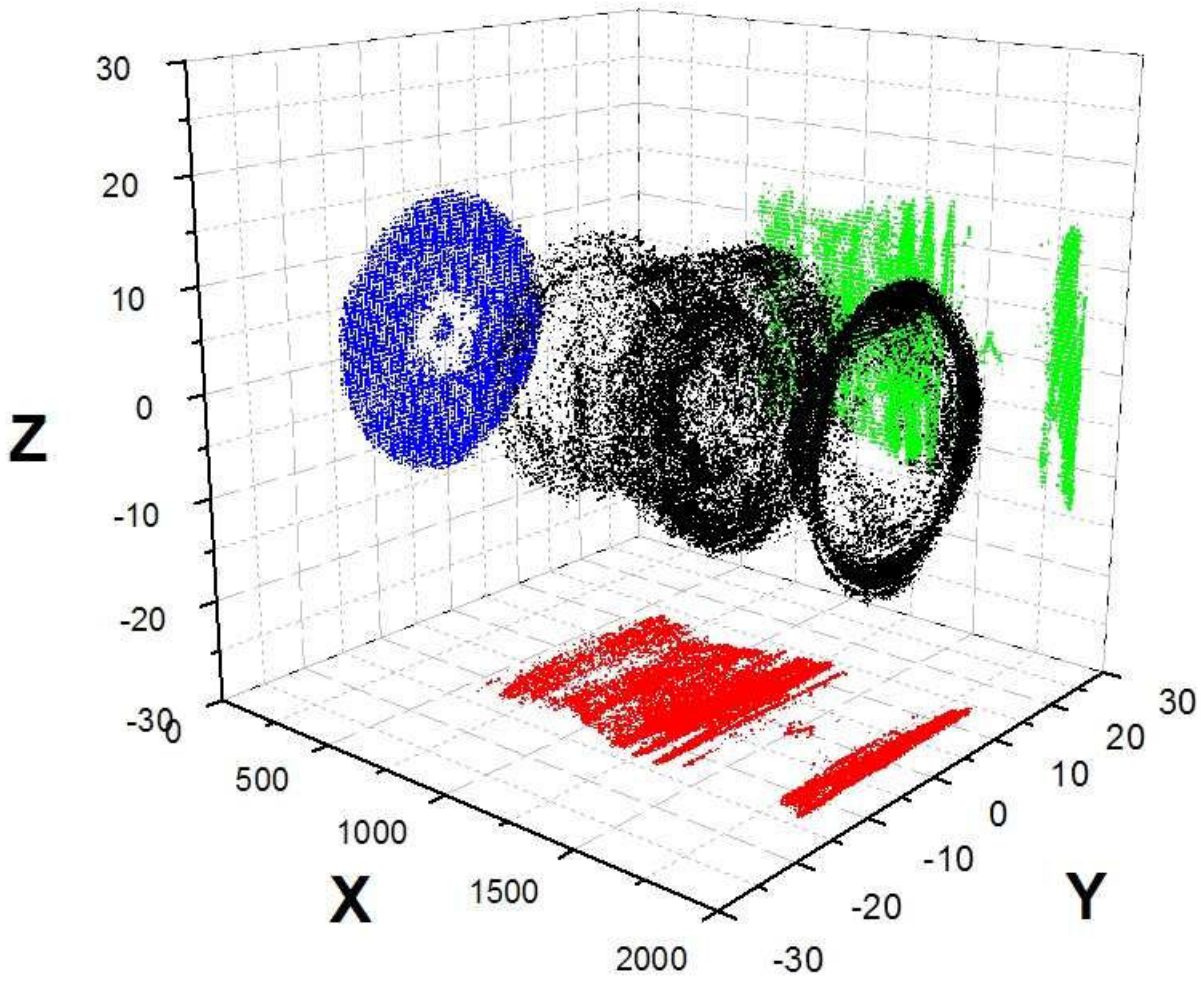

Figure 3.27: The distribution of initial positions of accelerated electrons. The X-axis is the direction of the laser propagation. Zeros of perpendicular coordinates corresponds to the axis of the laser pulse propagation, the middle of the simulation area. On the Figure are shown all electrons which were presented at the moment of time $T = 2000$ with the energy above $150MeV$. The case of the circular polarization.

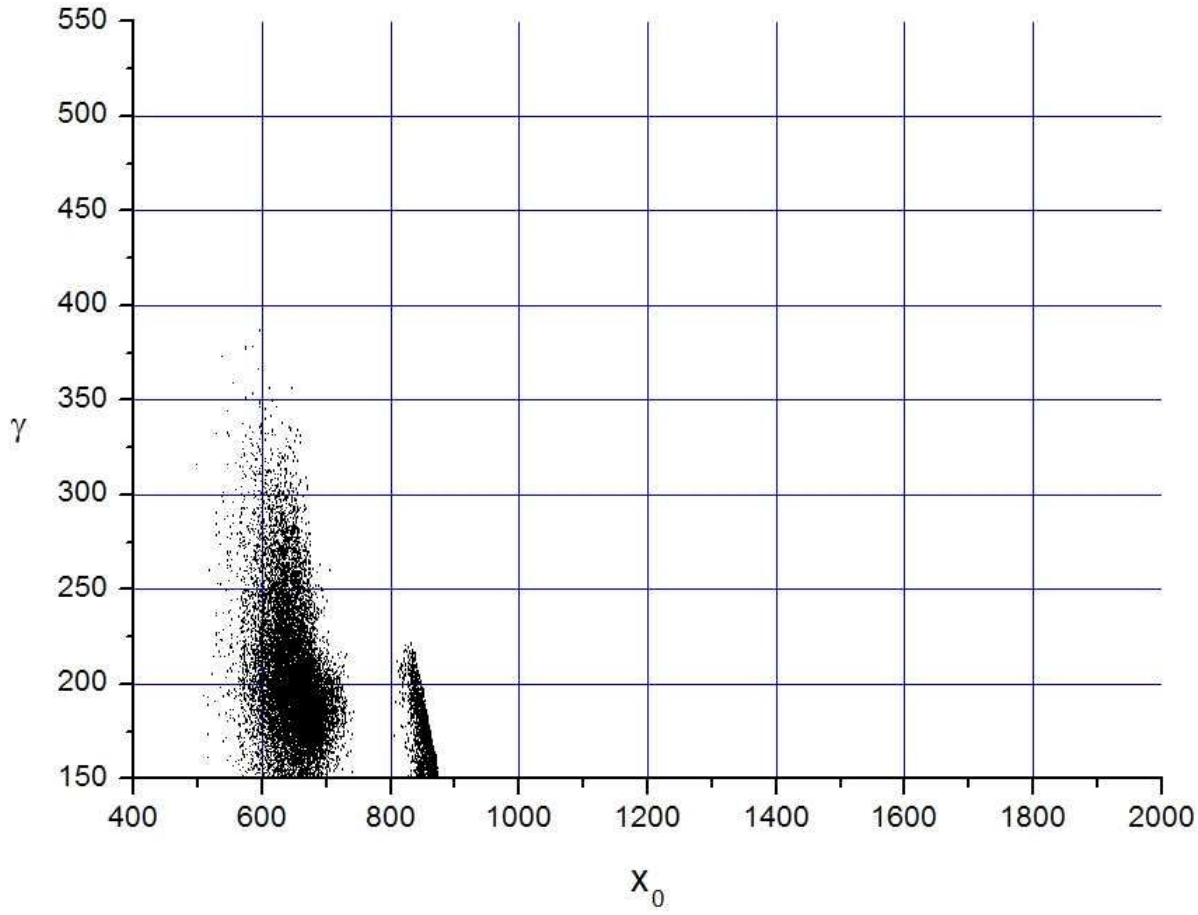

Figure 3.28: The distribution of the gamma-factor of electrons in the dependence from the x_0-coordinate of the capture. Only those particles were included which have the energy above $150MeV$. The distribution was taken at the moment of time $T = 1000$ of laser periods. The case of the circular polarization.

The front of distribution shown on the Figure (3.28) represents that the capture has begun at $x_0 \sim 600$ of laser wavelengths, further has stoped at $x_0 \sim 720$ of laser wavelengths and further has restarted at $x_0 \sim 820$ of laser wavelengths.

To the moment of time $T = 1500$ of laser periods(Figure (3.29)) the picture has changed. The process which has restarted at $x_0 \sim 820$ of laser wavelengths has been reducing intensity till $x_0 \sim 900$ of laser wavelengths and further has begun increasing intensity again, untill $x_0 \sim 1000$ of laser wavelengths. At the moment of time $T = 2000$ of laser periods(Figure (3.30)) the distribution shows that the capture of electrons has stoped at $x_0 \sim 1380$ of laser wavelengths and has started again at $x_0 \sim 1720$ of laser wavelengths. This dynamic of the capture of electrons corresponds to the information from the graphical part of simulation.

The Figure (3.17) represents distribution of current x-coordinates of electrons in dependence from x_0-coordinate of capture at the moment of time $Time = 2000$.

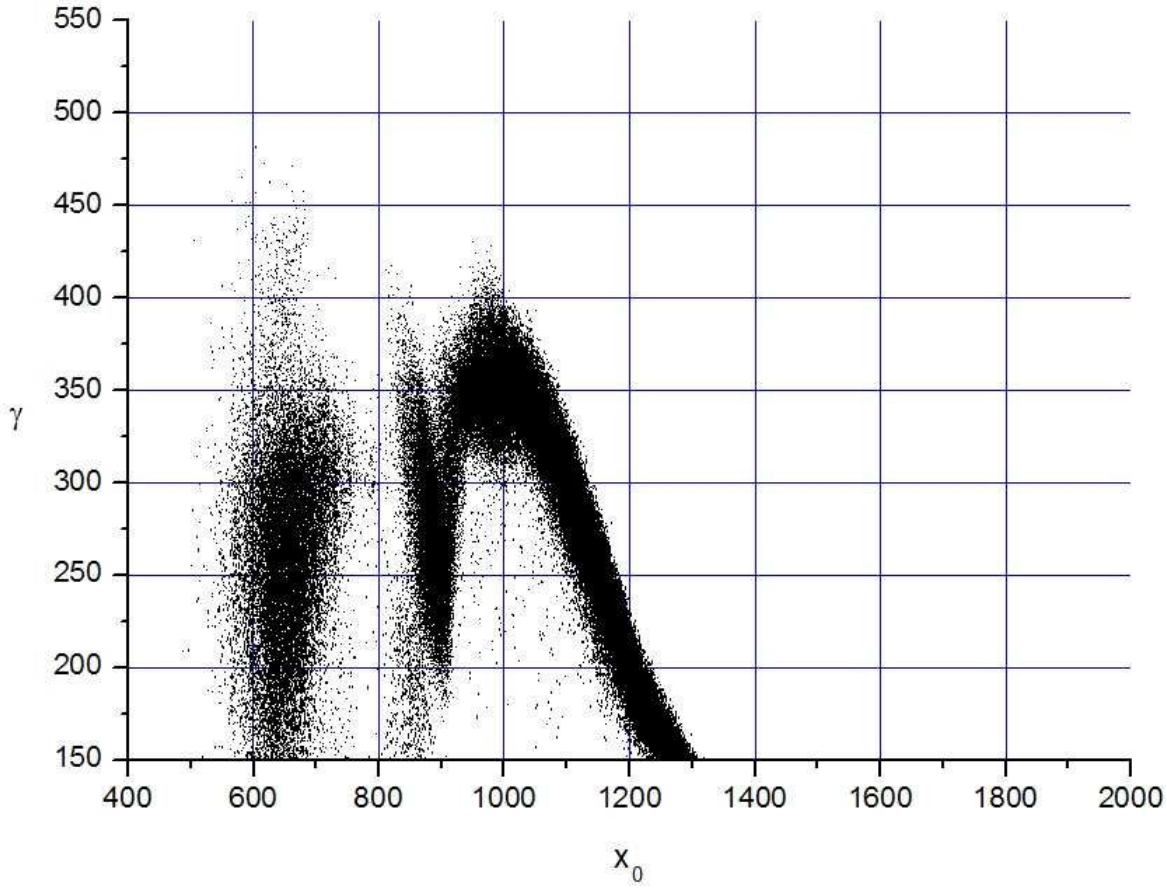

Figure 3.29: The distribution of the gamma-factor of electrons in the dependence from the x_0-coordinate of the capture. Only those particles were included which have the energy above $150MeV$. The distribution was taken at the moment of time $T = 1500$ of laser periods. The case of the circular polarization.

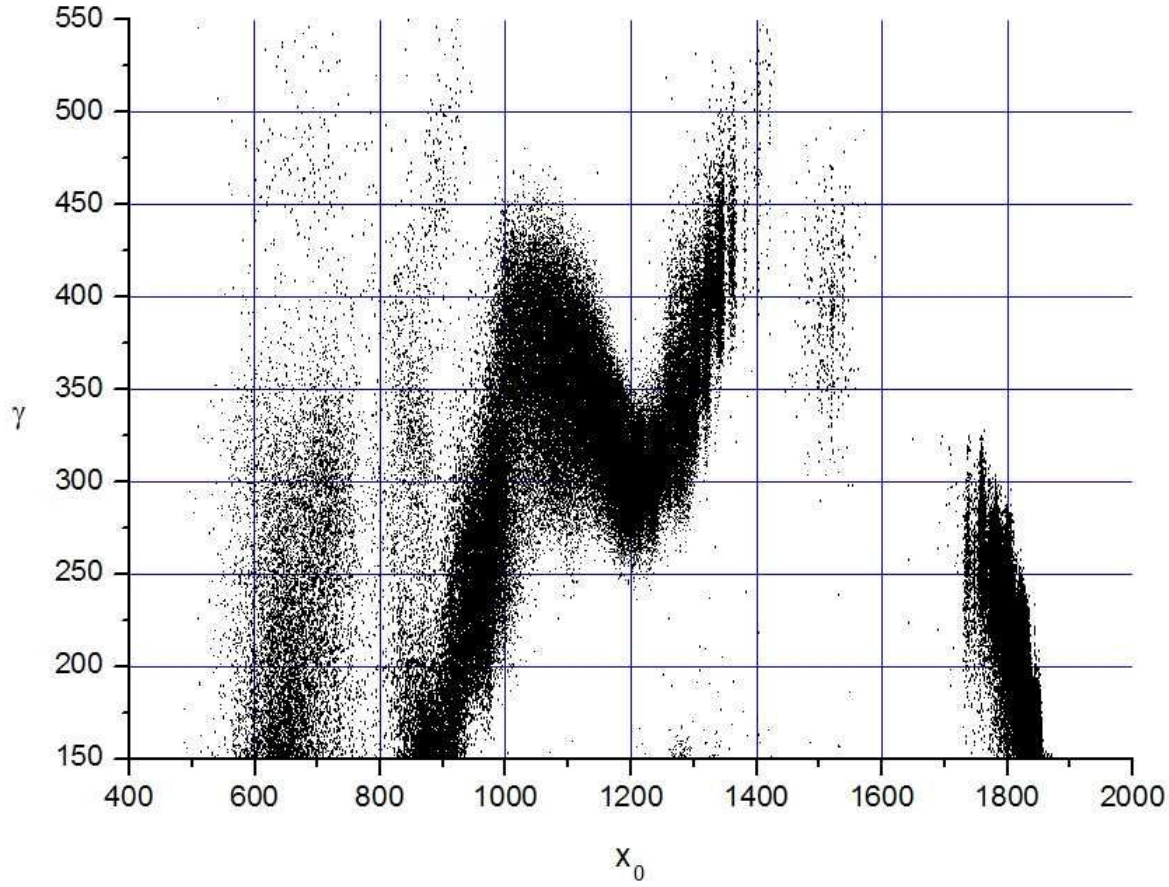

Figure 3.30: The distribution of the gamma-factor of electrons in the dependence from the x_0-coordinate of the capture. Only those particles were included which have the energy above $150MeV$. The distribution was taken at the moment of time $T = 2000$ of laser periods. The case of the circular polarization.

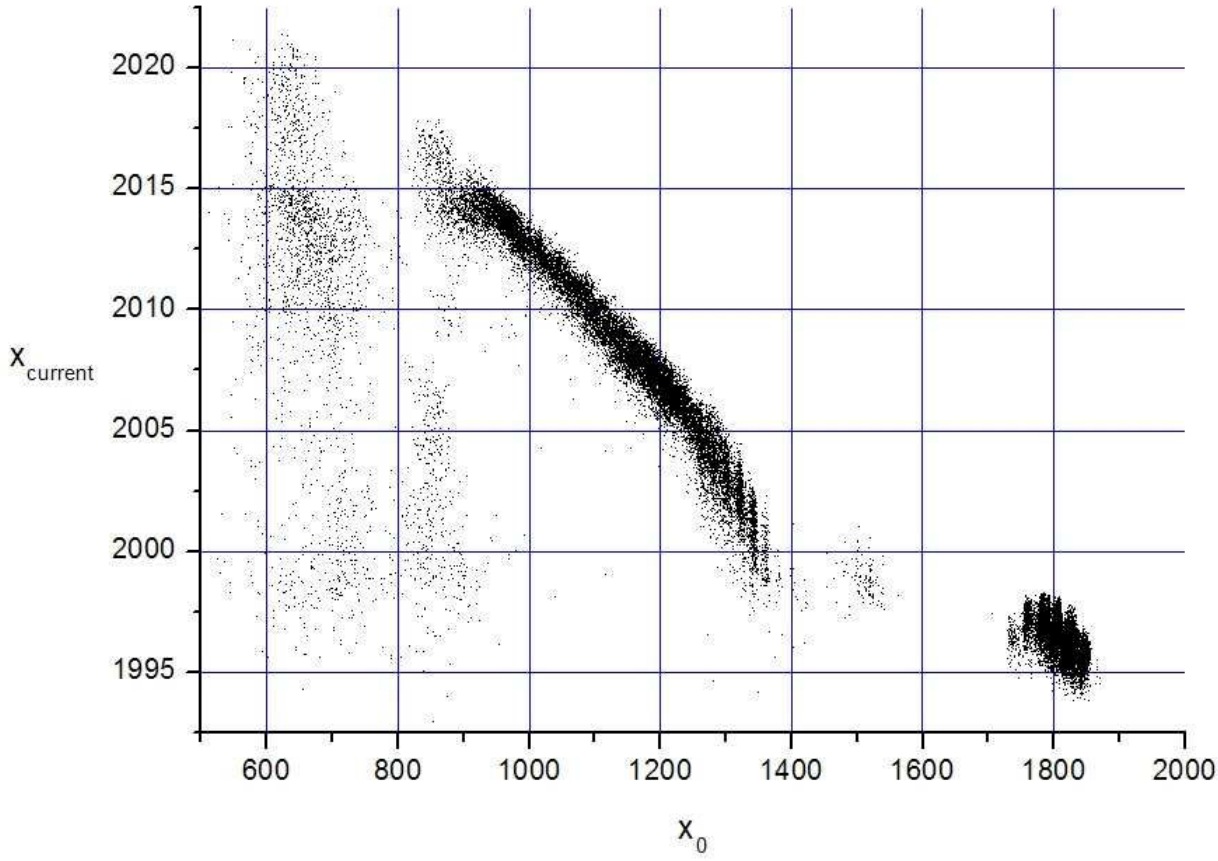

Figure 3.31: The distribution of current x-coorginate of electrons in the bubble in dependence from coordinate of capture. The data were taken at phase $T = 2000$.

It is seen from the Figure that majority of particles is located in area which can be approximated by one line. A line describes defined relation between coordinates and the point of capture of a particle. The electrons which were captured at more early times have greater current coordinate. Therefore the particles inside the electron bunch are moving from back part to the front part. The velocity of moving inside electron bunch is determined by the slope of the approximation line. Also from the Figure we can conclude that by the moment of time $T = 2000$ the majority of electrons which are presented in the electron bunch was captured in area of x-axis $1200 - 1500$ wavelengths. The electron bunch have approximately size 15 wavelengths on x-axis what confirms the graphical information from Figure (3.7).

The Figure (3.32) represents the dependence of the number of captured electrons from location of capture point at three different moments of time. Resolution along x-axis is half laser wavelength. The numbers shown on graphs are quantities of electrons which were captured in one-wavelength area along x around the corresponding x-value. Not complete similarity of the form cross area of the graphics explained by loss of the energy of particle with time. It means for each time shown on the Figure only high

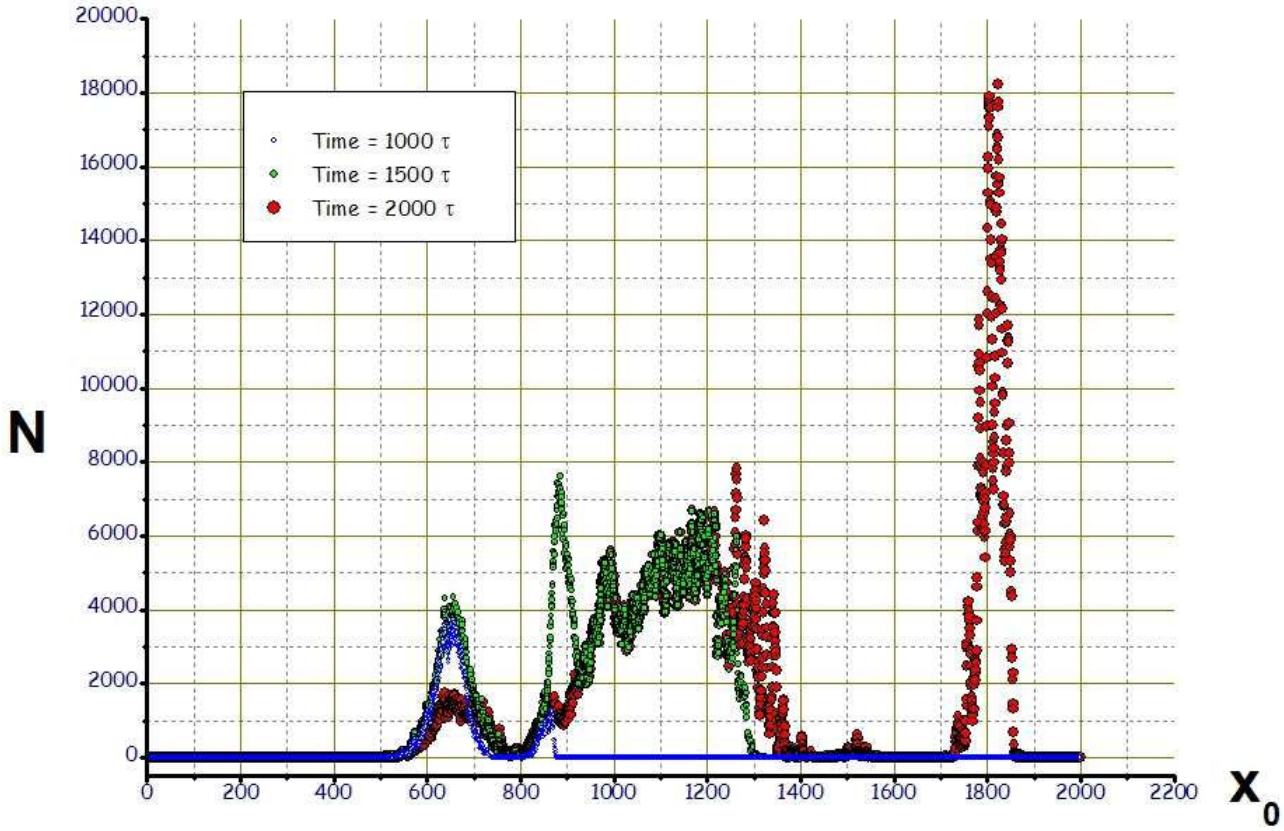

Figure 3.32: The distribution of the number of captured electrons in dependence from the x-coordinate of the capture. Distribution shown at three different moments of time: $T = 1000$ of laser period (blue), $T = 1500$ of laser periond (green) and $T = 2000$ of laser period (red). The laser pulse have circular polarization. For each moment of time were taken only those particles which had the energy greater $150MeV$ at corresponding moment of time.

energetic($\geq 150MeV$) electrons are presented.

Chapter 4

Ultra-short gaussian pulse

4.1 Introduction

Due to rapid advances in the generation of femtosecond laser pulses [61], the study of their spatiotemporal behavior on propagation in free space [62]-[67] and plasma has become a subject of interest. It is novadays well established [68], [69] that the propagation of femtosecond laser pulses cannot be assimilated to that of longer quasimonochromatic pulses, but the spatial and temporal characteristics interact with each other during propagation. In free space, spatiotemporal couplings such as pulse time delay, pulse broadening, and frequency lessening toward the beam periphery have been reported in several papers for different initial conditions.

In this chapter we find a pulsed Gaussian beam using the saddle-point method and some simple physical considerations and show the results of realization of described method in the VLPL3D PIC-code. We consider construction of the electromagnetic field and the propagation of pulsed Gaussian beam in free space and in propagation plasma. Numerical simulations of pulsed Gaussian beam in the plasma with different initial conditions are shown.

4.2 Analytic description

We start with the vector-potential in the form of the integral:

$$\mathbf{a}(t,\mathbf{r}) = \int \exp(-i\omega_0 t + i\mathbf{kr}) \cdot \delta(k_x - \sqrt{\omega_0^2 - k_y^2 - k_z^2}) \cdot f(k_y, k_z) dk_x dk_y dk_z \ , \qquad (4.1)$$

where the first multiplyer under sighn of integral corresponds to the standard wave description, the second multiplyer means that the dispersion relation must be satisfied, and the third multiplyer describes the profile of pulse; $\omega_0 > 0$. To be specific the pulse, we take profile to be Gaussian:

$$f(k_y, k_z) = \exp(-\sigma^2(k_y^2 + k_z^2)/2), \omega_0\sigma \gg 1 \ . \qquad (4.2)$$

Rewriting (4.1) as

$$\mathbf{a}(t,\mathbf{r}) = \exp(i\omega_0 t + i\omega_0 x)\int \exp\left(-i\frac{k_y^2+k_z^2}{2\omega_0} + ik_y y + ik_z z - \frac{\sigma^2(k_y^2+k_z^2)}{2}\right) dk_z dk_y \ . \tag{4.3}$$

The integral (4.3) is Gaussian. It is known that the values of Gaussian integrals can be presented as the value of the integrand at a stationary point of the exponential multiplied by a factor depending on the determinant of the matrix constructed from the second derivatives of the exponential.

In order to find the stationary point of the exponential we write

$$\partial_{k_z} S = \partial_{k_y} S = 0 \ , \tag{4.4}$$

where

$$S = -i\frac{k_y^2+k_z^2}{2\omega_0}x + ik_y y + ik_z z - \frac{\sigma^2(k_y^2+k_z^2)}{2} \ . \tag{4.5}$$

The calculation of (4.3) gives

$$\mathbf{a}(t,\mathbf{r}) = const \cdot \frac{\omega_0}{ix+\omega_0\sigma^2}\exp\left(-i\omega_0 t + i\omega_0 x - \frac{\omega_0 r^2}{2(ix+\omega_0\sigma^2)}\right) \ , \tag{4.6}$$

where $r^2 = y^2 + z^2$. The numerator in Eq. (4.6) describes the propagation of the wave fronts. The denominator is responsible for change the amplitude.

Let us construct the Gaussian wave packet in which the amplitude of each harmonic is proportional to

$$\exp\left(-\frac{1}{2}\left(\frac{\omega_0-\Omega}{\Delta\Omega}\right)^2\right) \ , \tag{4.7}$$

where $\Delta\Omega \sim 1/\tau$; τ is the pulse duration. This means that the integral

$$J = \int \exp\left(-\frac{1}{2}\left(\frac{\omega_0-\Omega}{\Delta\Omega}\right)^2\right)\cdot \mathbf{A} d\omega_0 \ . \tag{4.8}$$

must be calculated.

Notice that the value of $\sigma(\omega_0)$ in Eq. (4.6) can depend on ω_0. We choose $Z = \omega_0\sigma^2(\omega_0) = const$ for all ω_0 in order to simplify calculations. This choice means that the Rayleigh length is the same for all frequences.

For this particular choice of $\sigma(\omega_0)$ we read

$$\mathbf{A} = i\frac{1}{ix+Z}\frac{\partial}{\partial t}\int \exp\left(-\frac{1}{2}\left(\frac{\omega_0-\Omega}{\Delta\Omega}\right)^2\right)\exp\left(-i\omega_0 t + i\omega_0 x - \frac{\omega_0 r^2}{2(ix+Z)}\right) d\omega_0 \ . \tag{4.9}$$

The time derivative in front of the integral in Eq. (4.9) is introduced in order to exclude the factor ω_0 in Eq. (4.6). This is necessary in order to convert the integrand of (4.9)

into a Gaussian integral. From Eq. (4.9) we find

$$\begin{aligned}\mathbf{A} = const \cdot \tfrac{\Omega - i\Delta\Omega^2(t-x) - \Delta\Omega^2 r^2/(2(ix+Z))}{ix+Z} \\ \exp\left(-i\Omega t + i\Omega x - \tfrac{\Omega r^2}{2(ix+Z)}\right) \\ \exp\left(0.5\left(i\Delta\Omega(t-x) + \tfrac{\Delta\Omega r^2}{2(ix+Z)}\right)^2\right) \ .\end{aligned} \tag{4.10}$$

Notice that in the area where the pulse has a significant amplitude the correction

$$i\Delta\Omega^2(t-x) + \Delta\Omega^2 r^2/(2(ix+Z)) = O(\Delta\Omega/\Omega)\Omega \tag{4.11}$$

is not very small for short laser pulses and should be taken into account.

Eq. (4.10) is not valid for large y. In fact it is valid only in area

$$|y| < \sqrt{2}\sqrt{1 + \frac{x^2}{\Omega^2\sigma^4}}\frac{\Omega}{\Delta\Omega}\sigma \ . \tag{4.12}$$

This restriction results from the fact that Eq (4.3) is not valid for $\omega_0 \propto 1/\sigma$. However this frequency domain is present in the spectrum given by Eq. (4.7). The waves in this frequency area are very small. As a result, Eq. (4.10) is valid unless $\mathbf{A}$ is very small. Since the field decays very fast as one goes to large y, this area of very small fields is not far away from the axis.

Using the known perpendicular components of vector-potential we find the longitudial part. For the vector-potential $\vec{A}(\vec{r},t) = A_x\vec{e}_x + A_y\vec{e}_y + A_z\vec{e}_z$ we demand

$$\mathrm{div}\vec{\mathrm{A}} = 0 \ , \tag{4.13}$$

rewriting (4.13)

$$\partial_x A_x + \partial_y A_y + \partial_z A_z = 0 \ . \tag{4.14}$$

we have

$$A_x \ = -\int \frac{\partial A_y}{\partial y}dx + \int \frac{\partial A_z}{\partial z}dx \ . \tag{4.15}$$

Perpendicular parts can be written in form

$$A_y = A_z = e^{i\omega x} \cdot F \ , \tag{4.16}$$

where

$$\begin{aligned}F = const \cdot \tfrac{\Omega - i\Delta\Omega^2(t-x) - \Delta\Omega^2 r^2/(2(ix+Z))}{ix+Z} \\ \exp\left(-i\Omega t - \tfrac{\Omega r^2}{2(ix+Z)}\right) \\ \exp\left(0.5\left(i\Delta\Omega(t-x) + \tfrac{\Delta\Omega r^2}{2(ix+Z)}\right)^2\right) \ .\end{aligned} \tag{4.17}$$

In order to simplify calculations we assume that

$$A_x \ = -\int e^{i\omega x}dx \cdot \frac{\partial F}{\partial y} + \int e^{i\omega x}dx \cdot \frac{\partial F}{\partial z} \ , \tag{4.18}$$

because only $e^{i\omega x}$ gives the largest impact in the growth of functions A_y and A_z.

Further we have to consider the influence of the polarization factor and of relative phase between the fields. The polarization factor appears in each perpendicular vector-potential like usual multiplier. The phase fields appears like an additional item in the argument in exponential function. Finally we can write

$$\begin{aligned} A_z = const \cdot \mathrm{Z_{pol}} & \frac{\omega - \mathrm{i}(\Delta\omega)^2(\mathrm{t-x}) - (\Delta\omega)^2\mathrm{r}^2/(2(\mathrm{ix+Z}))}{\mathrm{ix+Z}} \\ & \exp\left(-i\omega t + i\omega x - \frac{\omega r^2}{2(ix+Z)} + iZ_{phase}\right) \\ & \exp\left(0.5\left(i\Delta\omega(t-x) + \frac{\Delta\omega r^2}{2(ix+Z)}\right)^2\right) , \end{aligned} \tag{4.19}$$

$$\begin{aligned} A_y = const \cdot \mathrm{Y_{pol}} & \frac{\omega - \mathrm{i}(\Delta\omega)^2(\mathrm{t-x}) - (\Delta\omega)^2\mathrm{r}^2/(2(\mathrm{ix+Z}))}{\mathrm{ix+Z}} \\ & \exp\left(-i\omega t + i\omega x - \frac{\omega r^2}{2(ix+Z)} + iY_{phase}\right) \\ & \exp\left(0.5\left(i\Delta\omega(t-x) + \frac{\Delta\omega r^2}{2(ix+Z)}\right)^2\right) , \end{aligned} \tag{4.20}$$

$$A_x = -\frac{1}{i\omega}\left(\frac{\partial A_z}{\partial z} + \frac{\partial A_y}{\partial y}\right) , \tag{4.21}$$

where $r = \sqrt{y^2 + z^2}$, ω is the frequency, $\Delta\omega = \omega/2\pi$ is inversely proportional to the wave packet duration, σ corresponds to the radius of the focal waist and $Z = \omega\sigma^2$.

Using known relations for electromagnetic field

$$E_i = -\frac{1}{c}\frac{\partial A_i}{\partial t} , \tag{4.22}$$

$$B = \mathrm{rot}\vec{\mathrm{A}} = -\begin{vmatrix} i & j & k \\ \partial_x & \partial_y & \partial_z \\ A_x & A_y & A_z \end{vmatrix} , \tag{4.23}$$

we can write

$$E_x = \mathrm{Re}\{-\frac{\partial \mathrm{A_x}}{\partial \mathrm{t}}\} , \tag{4.24}$$

$$E_y = \mathrm{Re}\{-\frac{\partial \mathrm{A_y}}{\partial \mathrm{t}}\} , \tag{4.25}$$

$$E_z = \mathrm{Re}\{-\frac{\partial \mathrm{A_z}}{\partial \mathrm{t}}\} , \tag{4.26}$$

$$B_x = \mathrm{Re}\{\frac{\partial \mathrm{A_z}}{\partial \mathrm{y}} - \frac{\partial \mathrm{A_y}}{\partial \mathrm{z}}\} , \tag{4.27}$$

$$B_y = \mathrm{Re}\{-\frac{\partial \mathrm{A_z}}{\partial \mathrm{x}} + \frac{\partial \mathrm{A_x}}{\partial \mathrm{z}}\} , \tag{4.28}$$

$$B_z = \mathrm{Re}\{\frac{\partial \mathrm{A_y}}{\partial \mathrm{x}} - \frac{\partial \mathrm{A_x}}{\partial \mathrm{y}}\} . \tag{4.29}$$

Using standard mathematical software we obtained the final result for the 6 components of electromagnetic field. The verbatim of field components takes too much place for showing here, but these results were included in the VLPL3D PIC-code in the form of the expressions of fields.

4.3 Realization

In the VLPL3D PIC-code new Gaussian fields were added and few parameters were included in the file with initial configuration of the computer simulation. The parameter $IsDipole = 2$ switches the Gaussian kind of the laser pulse. Also in the configuration file were added the following parameters: $FocusRadius$, $FocusCenter$, $FocusLength$, which correspond to the radius of the focal waist, the position of the focus and the range between the focus point and the point of initialization of Gaussian pulse. By parameters $Ypol$, $Zpol$ we set kind of the polarization of laser pulse. The parameter $Length$ is responsible for the length of the pulse at the focal waist when the kind of pulse is set to be Gaussian. All geometric parameters are measured in wavelengths of the laser pulse.

The Figure (4.1) represents evoluton of the pulsed Gaussian beam in the numerical simulation of laser propagation in vacuum. Fields shown in the Figure were taken at five different moments of time: $T = -18$, $T = -6$, $T = 0$, $T = +6$, $T = +18$. Time is measured in the laser periods. At the zeroth moment of time the pulsed Gaussian beam is at the focal point. Negative values of time correspond to moments of time before the point of the focus. Each column which is shown on the Figure (4.1) represents three different fields of the Gaussian pulse at defined moment of time: E_y, B_z and E_x. The color scale for the fields is shown in the left from each frame. The zero of the perpendicular coordinates along the Y- and the Z-axis corresponds to the axis of the propagation of pulsed Gaussian beam. All coordinates are given in laser wavelengths.

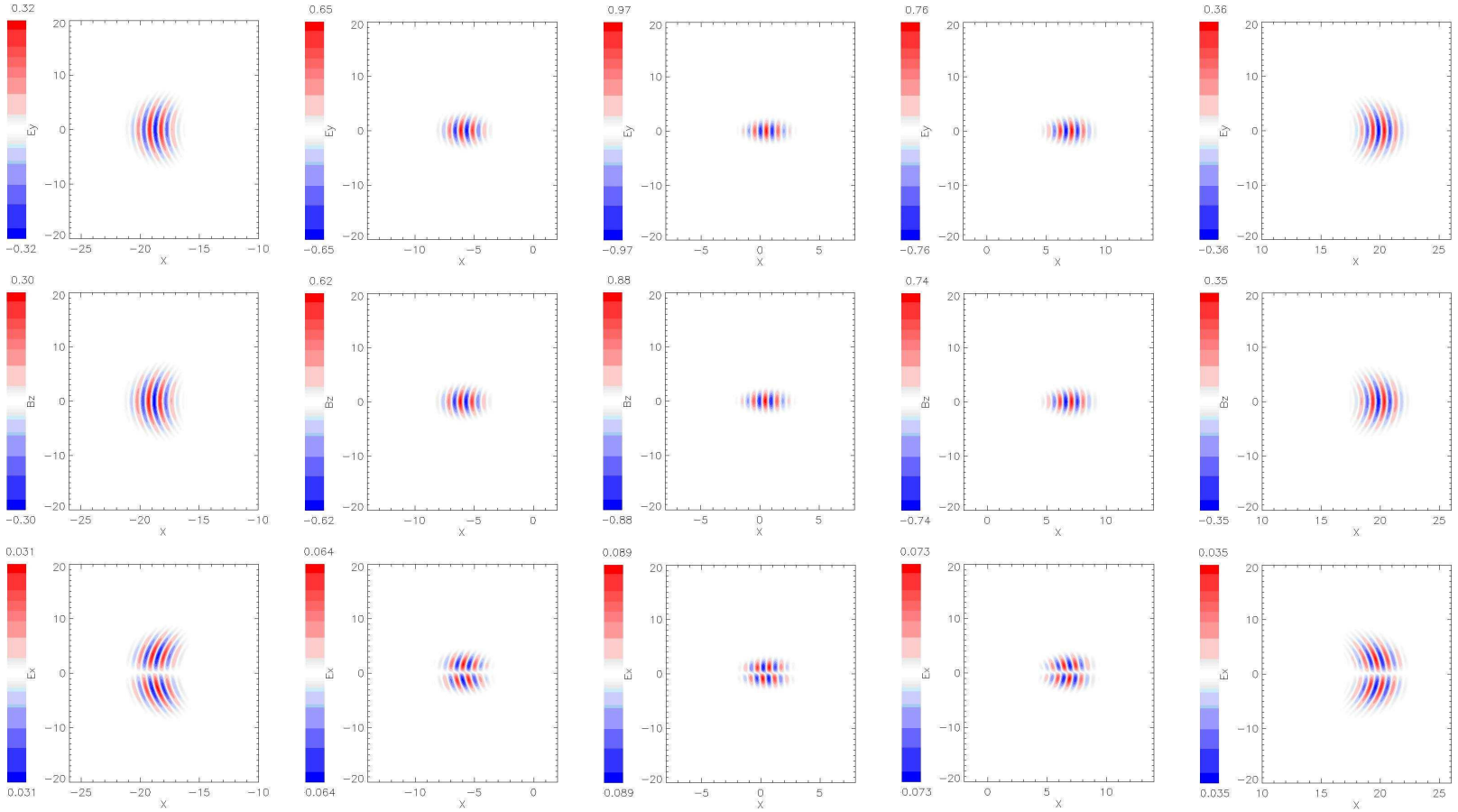

Figure 4.1: The pulsed Gaussian beam in the VLPL3D PIC-code simulation in free space.

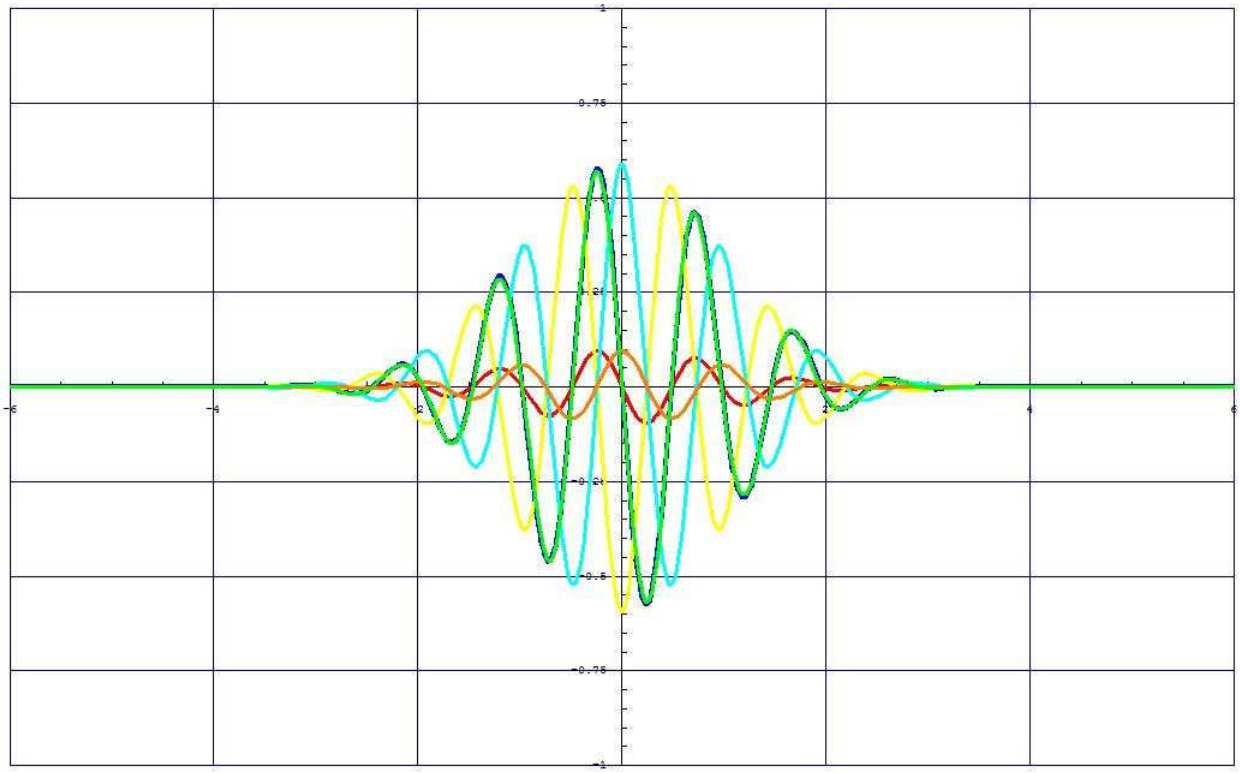

Figure 4.2: Fieds of pulsed Gaussian beam which were taken analytically with conditions $T = 0, y = 0, z = 1$: E_x(red), E_y(blue), E_z(yellow), B_x(green), B_y(light-blue), B_z(orange).

Results of the numerical simulation were compared with the analytical ones. Using mathematical software we made graphics of fieds at different conditions.

The Figure (4.2) represents two-dimensional graph of all six fields of the pulsed Gaussian beam at the moment of time $T = 0$(time of the focus), at coordinates $(y = 0, z = 1)$(z was taken equival to one by the reason that exactly on the axis of propagation longitudial fields are vanish). In the Figure (4.2) shown the difference between amplitudes and phases of different fields.

The Figure (4.3) represenrs three from six fields of the pulsed Gaussian beam(E_y, B_z, E_x) at the moments of time $T = -18, T = -6, T = 0, T = +6, T = +18$ in the $(Y - Z)$ plane which is perpendicular to the propagation direction, X-axis. Each column corresponds to one from moments of time.

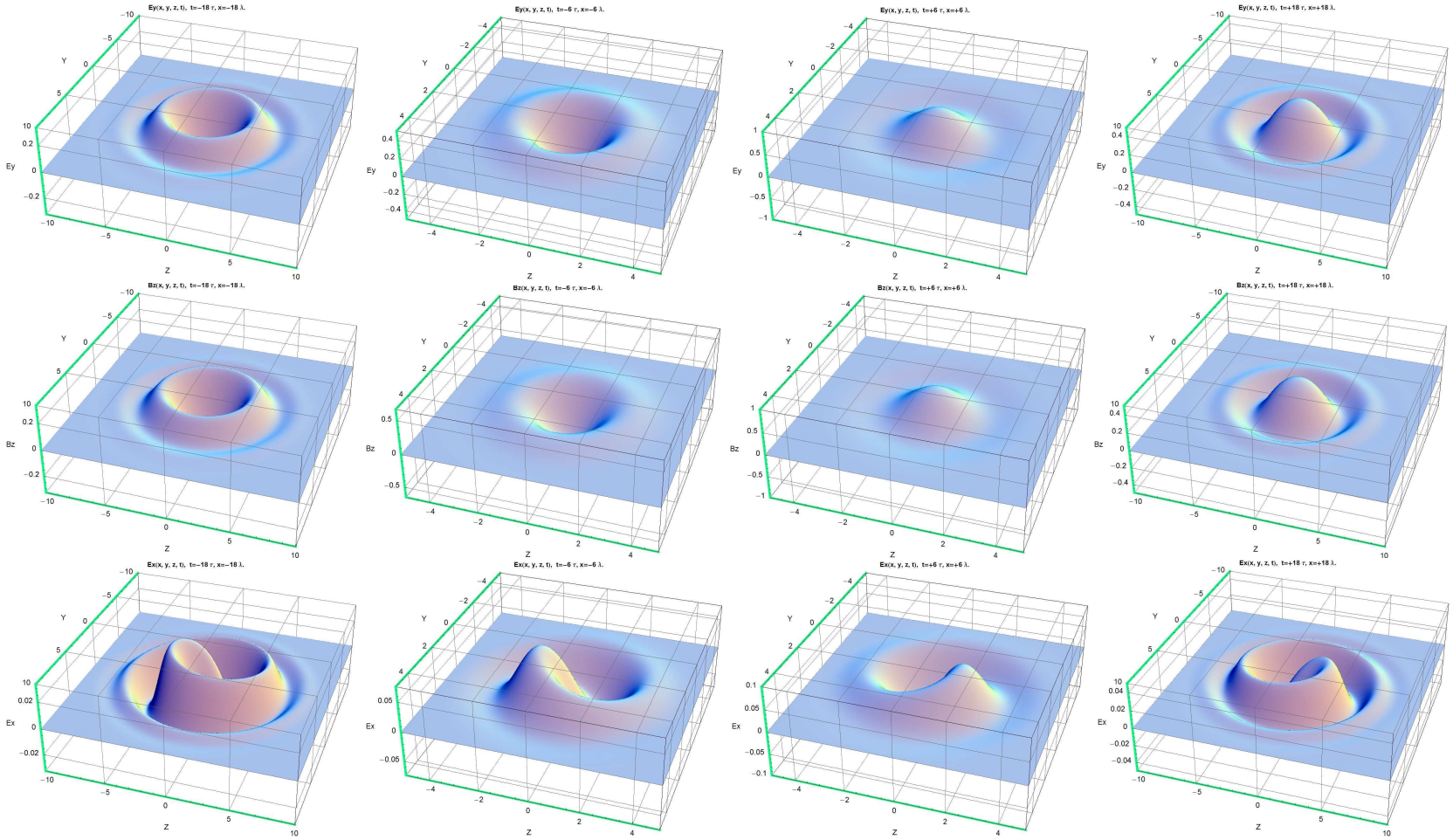

Figure 4.3: The pulsed Gaussian beam expressed in the mathematical software in the $(Y - Z)$ plane.

The Figure (4.4) represents fields of the pulsed Gaussian beam which were taken analytically in the form which is similar with (4.1). Fieds which are shown on the Figure (4.4) were taken at moments of time: $T = -16, T = -6, T = 0, T = +6, T = +18$. One column corresponds to one moment of time, where the fields E_y, B_z and E_x are shown.

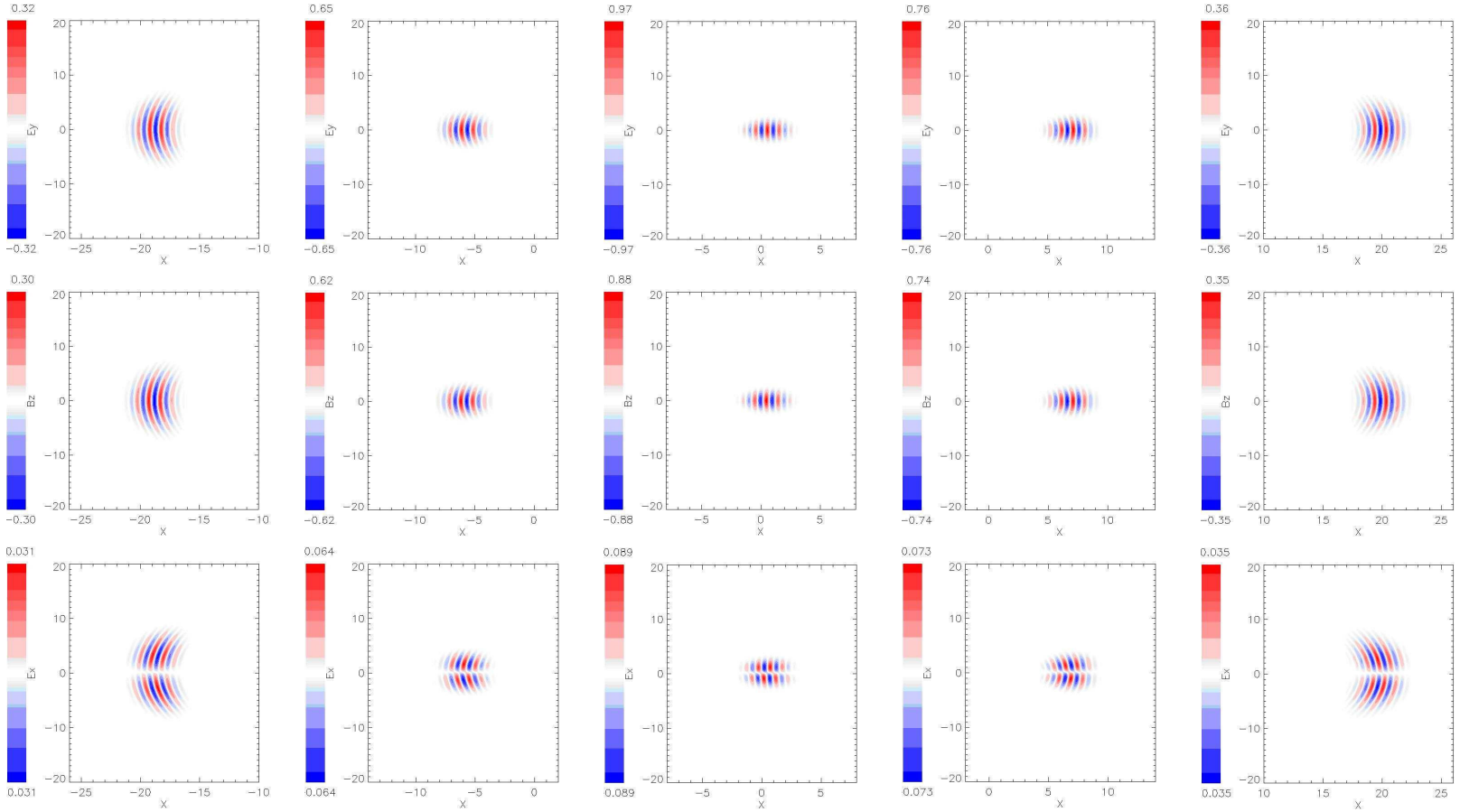

Figure 4.4: The pulsed Gaussian beam expressed in the mathematical software.

The Figure (4.5) represent fields E_y, B_z and E_x at the moment of time $T = 0$ in analytic form and fields which were taken directly from the file of the numerical simulation. It is seen that we have good agreement between the result of computer simulation and the analytic form of fields.

By all Figures which were presented in this section it can be concluded that the pulsed Gaussian beam in the VLPL3D PIC-code have good accordance with the analytic form. In further it can be used for any kind of the numerical simulations of the propagation of pulsed Gaussian beam and interaction of described laser pulse type witch the plasma.

4.4 The influence of the focal position on the electron spectra

A number of computer simulations has been performed with the constructed pulsed Gaussian beam. The laser wavelength was taken $\lambda_0 = 0.82\mu m$. We use a simulation box of dimension $(60 \times 60 \times 60)\lambda$ volume what corresponds to the size $(49 \times 49 \times 49)\mu m$. The number of gridpoints is $800 \times 86 \times 86 = 5.9 \cdot 10^6$. The resolution in the transverse direction is $k_{p_0}\Delta y = 0.36$, the resolution in longitudinal direction is $k_{p_0}\Delta x = 0.04$, where $k_{p_0} = \omega_p/c$, $k_0/k_{p_0} = 11.95$, $\omega_p \equiv 4\pi e^2 n_0/m$. We use two macroparticles / cell. The plasma density is $n_0 = 0.1 \cdot n_{crit} = 1.16 \cdot 10^{19}$. The laser pulse is pulsed Gaussian beam, which is circularly polarized and has the length at focus $Length = 3\lambda$. The pulsed Gausian beam has the focal waist $\sigma = 5$ laser periods. The focal positions were taken at 5 different distances from the plasma front.

The Figure (4.6) represents the electron spectra in computer simulation with the different initial conditions. The position of the focal waist of pulsed Gaussian beam was varied relatively of the plasma beginning. It means the pulsed Gaussian beam was focused at positions of $75\lambda, 50\lambda$ and 25λ before the plasma, and at distances of $25\lambda, 50\lambda$ and 75λ inside the plasma and exactly at the border of the plasma. Using the postprocessing we obtained electrons spectra for each numerical simulation. Resolution along the$x$-axis is $2MeV$, Figure (4.6).

We can conclude that the spectra of electrons has insignificant dependence from the position of the focal waist of the laser pulse relatively of the plasma boundary. In all the cases the spectra have peak around $70MeV$. The dependence from the position of the focal waist occurs only in small part of electrons which has energies in range $(140 - 200)MeV$.

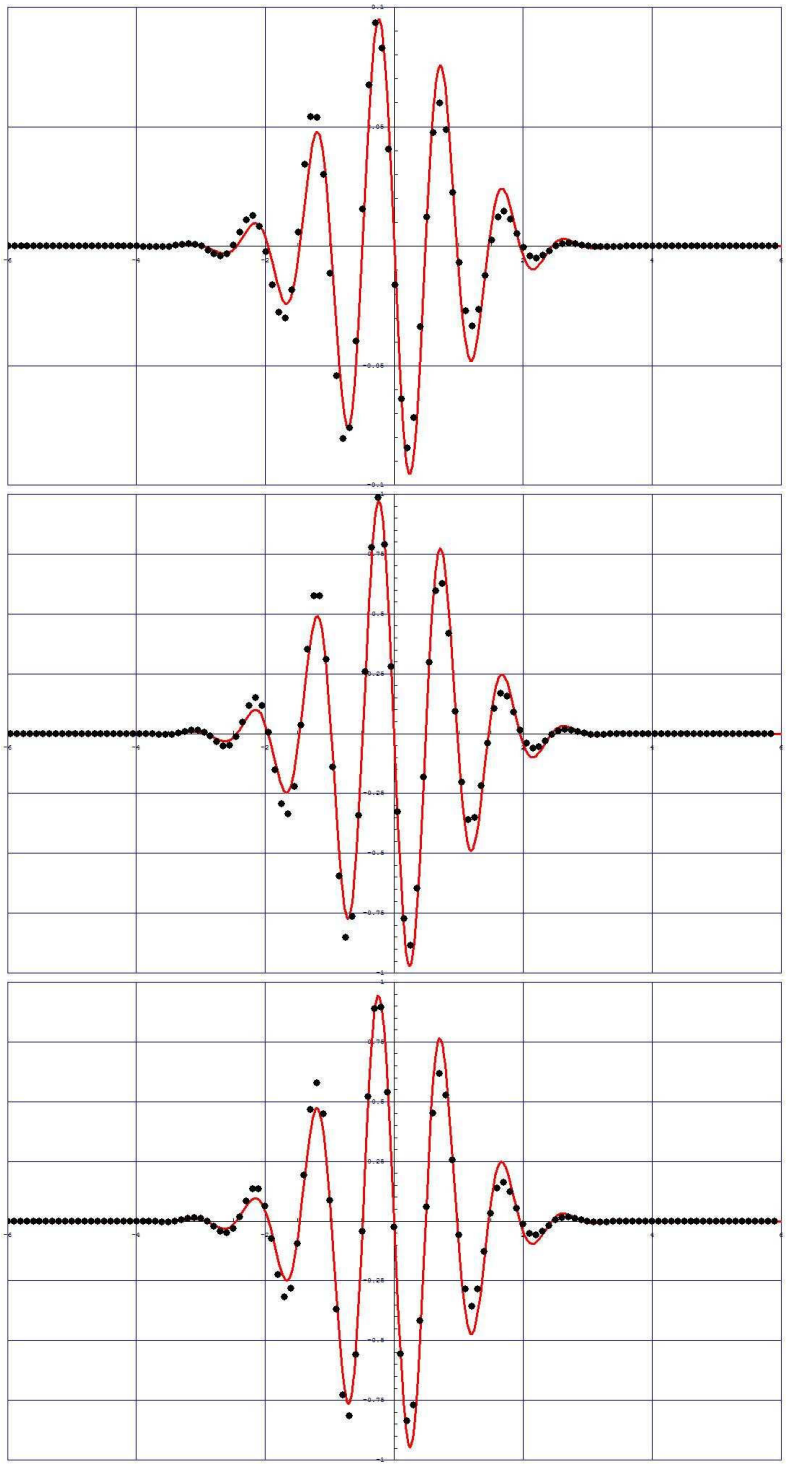

Figure 4.5: Fields E_x, E_y, B_z of the pulsed Gaussian beam at the moment of time $T = 0$. The solid line shows the field which was taken analytically. Points correspond to values of the field which were taken results of computer simulation.

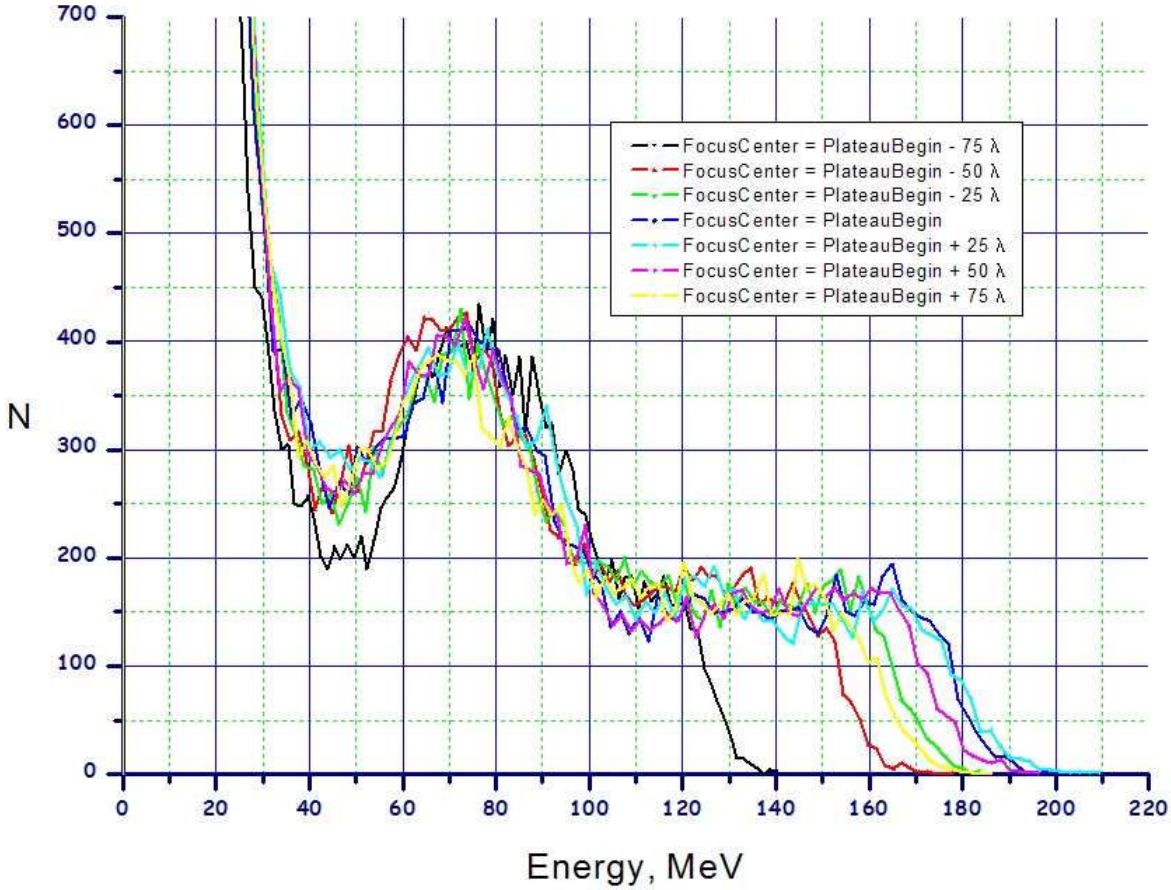

Figure 4.6: The spectra of electrons in the dependence of the position of focal waist relatively of the plasma boundary.

Chapter 5

Conclusions

In Conclusion we have studied in details the electron trapping and acceleration inside the electron bunch in the bubble regime of the laser-plasma interaction. Because of the complex nature of the ultra-relativistic laser-plasma interactions, our analysis contains a phenomenological part. We were able to trace trajectories of single electrons inside dense electron bunch which is generated in the the "bubble" regime. Calculated trajectories are in a good agreement with the theoretically predicted ones. Statistical distributions of particles in the electron bunch are determined by the energy and the polarization of the laser pulse. We have provided the estimation of properties of the electrons acceleration on the grounds of statistical consideration of the groups of particles in different areas of the bubble. Electrons in the generated dense electron bunch in PIC simulations gains the energy up to $450MeV$ with the value of acceleration estimated as $\sim 1MeV/\lambda$.

Using PIC simulations we have demonstrated images of electron trajectories inside the dense electron bunch. The electron trajectories have the form of a helix around the axis of laser pulse propagation. The energy of electrons exceeds the level of $150MeV$ during the time not less than 500 laser periods. We have presented the dynamics of the electron spectra and have described the process of electron captures into the generated electron bunch structure. On the grounds of the performed group of numerical PIC simulations we have concluded that the electrons acceleration occurs unregularly.

The new analytic model for an ultra-short laser beam has been developed. We have included the pulsed Gaussian beam in the PIC simulation with using additional physical parameters of laser pulse. Using the saddle-point method we have considered the algorithm of the pulsed Gaussian beam construction. We have compared the pulsed Gaussian beam in the computer simulation with the analytic form and obtained good agreement between the form and amplitudes of all component fields of the beam in the both cases. We have performed a set of PIC simulations using new pulsed Gaussian beam and determined the influence of the focus position related to the plasma boundary on the electron spectra of formed bubble. The constructed pulsed Gaussian beam is the additional tool for PIC simulation which can be applyed in any further numerical simulations performed with using of the VLPL3D PIC-code.

Appendix A

Size of the Wavebreaking Area

At the beginning of interaction the wavebreaking region is located on the x-axis, where ponderomotive potential is low and can be neglected. Using the one-dimensional cold fluid approximation we estimate the scale of this region. The one-dimensial approach as an estimation can be used here because $p_\perp \approx \partial p_\perp/\partial r_\perp \approx E_\perp \approx \partial E_\perp/\partial r_\perp \approx 0$ at this axis. The hydrodynamic approach fails when the wavebreaking accurs. However we assume thet the structure of the nonlinear plasma wave is not yet strongly destroyed at the beginning of the onteraction. The equation for the potential of the one-dimensional nonlinear plasma wave is [Akhizer and Polovin, 1956, Sprangle et al., 1990, Teychenne et al., 1993]

$$\frac{d^2\Phi}{d\chi^2} = \frac{v_0 - \Phi\sqrt{\Phi^2 - \gamma_0^{-2}}}{v_0(\Phi^2 - \gamma_0^{-2}) + \Phi\sqrt{\Phi^2 - \gamma_0^{-2}}} \ , \tag{A.1}$$

where $p_\perp = p_y = 0$ is assumed.

An analysis of Eq.(A.1) shows that $\Phi_{min} < \Phi < \Phi_{max}$, where $\Phi_{min} \simeq \Phi_{max}^{-1}$ in the limit $\Phi_{max} \gg 1$ [Teychenne et al., 1993]. The singularity appears in the right-hand side of Eq. (A.1) in the limit $\Phi_{max} = \gamma_0$. This means the plasma wavebreaking and the failure of the cold fluid approach [Teychenne et al., 1993, Sprangle et al., 1990]. We assume that the bubble velocity is close to the group velocity of the laser pulse $\gamma_0 \simeq 13$ at the at the beginning of interaction. It follows from Eq. (3.9) that $\Phi_{max} = R^2/4$. The first integral given by Eq. (A.1) in the limit $1 \ll 1/\Phi_{min} \simeq \Phi_{max}$ and $\Phi < 1$, $\gamma_0 \gg 1$ reduces to the form

$$\left(\frac{d\Phi}{d\xi}\right)^2 \simeq \frac{1}{\Phi_{min}} - \frac{1}{\Phi} \ . \tag{A.2}$$

Integrating Eq. (A.1) from 1 to Φ_{min} we find of the wavebreaking region

$$D/2 \simeq \Phi_{max}^{-1/2} \ . \tag{A.3}$$

We get $D \simeq 0.6$ for $R \simeq 7$ from Eq. (A.4) that is about two times smaller than the value of the pattern width observed in the PIC simulation at $l_{int} = 25$. It follows from the Hamiltonian that

$$\gamma \simeq \gamma_0^2 \Phi_{max}^{-1} \left(1 - \sqrt{1 - \Phi_{max}^2 \gamma_0^{-2}}\right) \ . \tag{A.4}$$

Eq. (A.1) gives $\gamma \simeq 7$ that is two times smaller than $\gamma_0 \simeq 13$. To derive a more accurate estimation for D and γ one needs a solution of a three-dimensional nonlinear equation on the plasma wave [Lotov, 1998].

Appendix B

Trajectory Divergence

The potential Φ is almost constant in the electron sheath and we use the equipotential approximation to analyse the electron motion in the sheath. We get from Eq. (3.24)

$$\gamma - v_0 p_x = \Phi \simeq const \ . \tag{B.1}$$

Then, Eqs. (3.19) and (3.21) reduces to the form

$$\frac{dP_x}{dt} \simeq \frac{dp_x}{dt} \simeq -\frac{d\chi}{dt} \ , \tag{B.2}$$

$$\frac{d\chi}{dt} = \frac{p_x}{\Phi + v_0 p_x} - v_0 \simeq -\frac{v_0 \Phi}{\Phi + v_0 p_x} \ , \tag{B.3}$$

where we the Lorentz force is taken in the form (3.18) and $p_x \ll \gamma_0^2$ is assumed. The obtained system of equations has the first integral

$$\frac{\chi^2 - \chi_0^2}{4} \simeq \Phi \ln(\Phi + v_0 p_x) \ , \tag{B.4}$$

where the initial conditions $-\chi = -\chi_0 \gg 1, y = y_0$ and $p_x = 0$ are assumed and Φ is of the order of unity in the electron sheath and outside of the wavebreaking pattern.

Using Eqs. (B.1) and (B.4) we get

$$\gamma \simeq \exp\left(\frac{\chi^2 - \chi_0^2}{4\Phi}\right) \ , p_y \simeq -\sqrt{2\Phi\gamma} \ , \tag{B.5}$$

where $\gamma \gg 1$ is assumed. Eq. (3.22) can be rewritten in the form

$$\frac{dy}{d\chi} = \frac{dy}{dt}\left(\frac{d\chi}{dt}\right)^{-1} = \frac{p_y}{p_x - v_0\gamma} \simeq \sqrt{\frac{2\gamma}{\Phi}} \ . \tag{B.6}$$

Integrating the obtained equation in the limit $|\chi_f - \chi_0| \ll |\chi_0|$ we find the shape of plasma cavity from the point, where the return current is over ($\chi = \chi_0$), to the cavity base ($\chi = \chi_f$) in the limit $\gamma \gg 1$

$$\ln\left[\frac{\chi_0(y - y_0)}{4\sqrt{2\Phi}}\right] \simeq \frac{\chi_0(\chi - \chi_0)}{4\Phi} \ . \tag{B.7}$$

Making use of Eq. (B.7) the distance between between two electrons can be evaluated

$$\delta R \simeq \frac{4\sqrt{2\gamma}}{\chi_0}\left(\frac{1}{2\sqrt{\Phi}} - \frac{\chi_f - \chi_0}{4\Phi^2}\right)\frac{d\Phi}{dy}\delta\rho \ , \tag{B.8}$$

where $\delta\rho \ll 1$ is the initial distance between two electrons. As $\Phi \sim 1$ and $\partial\Phi/\partial y = F \sim -\chi_0$ the trajectory divergence can be estimated as

$$\eta = \left|\frac{\delta R}{\partial\rho}\right| \simeq 4\sqrt{2\gamma}(\ln\sqrt{\gamma} - 1/2) \ . \tag{B.9}$$

Then the trajectory divergence between the point $\chi = \chi_0$ in the electron sheath, where $p_x = 0$, and the wavebreaking pattern ($\chi = \chi_f$) is

$$\eta \simeq 2R\ln\left(\frac{R}{2\sqrt{2}}\right) \ . \tag{B.10}$$

Here we have used $\gamma \simeq \Phi_{max}/2 \simeq R^2/8$. This follows fromEq. (A.4) in the limit $\Phi_{max}^2\gamma_0^2 \ll 1$.

Bibliography

[1] D. Strickland and G. Mourou, "Compression of amplified chirped optical pulses," *Opt. Commun.*, vol. 56, p. 219, 1985.

[2] P. Sprangle, E. Esarey, and J. Krall, "Laser driven electron acceleration in vacuum, gases, and plasmas," *Phys. Plasmas*, vol. 3, p. 2183, 1996.

[3] P. Sprangle, C.-M. Tang, and E. Esarey, "Relativistic self-focusing of short-pulse radiation beams in plasmas" *IEEE Trans Plasma Sci.*, vol. 15, p. 145, 1983.

[4] T. Tajima and J. M. Dawson, "Laser electron accelerator," *Phys. Rev. Lett.*, vol. 43, p. 267, 1979.

[5] A. I. Akhiezer and R. V. Polovin, "Theory of wave motion of an electron plasma," *Sov. Phys. JETP*, vol. 3, p. 696, 1956.

[6] J. M. Dawson, "Nonlinear electron oscillations in a cold plasma," *Phys. Rev.*, vol. 113, p. 383, 1959.

[7] A. Pukhov and J. Meyer-ter-Vehn, "Laser wake field acceleration: the highly non-linear broken-wave regime," *Appl. Phys. B*, vol. 74, p. 355, 2002.

[8] C. Joshi, T. Tajima, J. M. Dawson, H. A. Baldis, and N. A. Ebrahim, "Forward raman instability and electron acceleration," *Phys. Rev. Lett.*, vol. 47, p. 1285, 1981.

[9] J. B. Rosenzweig, D. B. Cline, B. Cole, H. Figueroa, W. Gai, R. Konecny, J. Norem, P. Schoessow, and J. Simpson, "Experimental observation of plasma wake-field acceleration," *Phys. Rev. Lett.*, vol. 61, p. 98, 1988.

[10] A. K. Berezin, Y. B. Fainberg, V. A. Kiselev, A. F. Linnik, V. V. Uskov, V. A. Balakirev, I. N. Onishchenko, G. L. Sidel'nikov, and G. V. Sotnikov, "Wake field excitation in plasma by a relativistic electron pulse with a controlled number of short bunches," *Plasma Phys. Rep.*, vol. 20, p. 596, 1994.

[11] M. Everett, A. Lal, D. Gordon, C. E. Clayton, K. A. Marsh, and C. Joshi, "Trapped electron acceleration by a laser-driven relativistic plasma wave," *Nature*, vol. 368, p. 527, 1994.

[12] K. Nakajima, D. Fisher, T. Kawakubo, H. Nakanishi, A. Ogata, Y. Kato, Y. Kitagawa, R. Kodama, K. Mima, H. Shiraga, K. Suzuki, K. Yamakawa, T. Zhang, Y. Sakawa, T. Shoji, Y. Nishida, N. Yugami, M. Downer, and T. Tajima, "Observation of ultrahigh gradient electron acceleration by a self-modulated intense short laser pulse," *Phys. Rev. Lett.*, vol. 74, p. 4428, 1995.

[13] A. Modena, Z. Najmudin, A. E. Dangor, C. E. Clayton, K. A. Marsh, C. Joshi, V. Malka, C. B. Darrow, C. Danson, D. Neely, and F. N. Walsh, "Electron acceleration from the breaking of relativistic plasma waves," *Nature*, vol. 377, p. 606, 1995.

[14] C. E. Clayton, C. Joshi, C. Darrow, and D. Umstadter, "Relativistic plasma-wave excitation by collinear optical mixing," *Phys. Rev. Lett.*, vol. 54, p. 2343, 1985.

[15] C. E. Clayton, K. A. Marsh, A. Dyson, M. Everett, A. Lal, W. P. Leemans, R. Williams, and C. Joshi, "Ultrahigh-gradient acceleration of injected electrons by laser-excited relativistic electron plasma waves," *Phys. Rev. Lett.*, vol. 70, p. 37, 1993.

[16] Y. Kitagawa, T. Matsumoto, T. Minamihata, K. Sawai, K. Matsuo, K. Mima, K. Nishihara, H. Azechi, K. A. Tanaka, H. Takabe, and S. Nakai, "Beat-wave excitation of plasma wave and observation of accelerated electrons," *Phys. Rev. Lett.*, vol. 68, p. 48, 1992.

[17] J. R. Marquès, J. P. Geindre, F. Amiranoff, P. Audebert, J. C. Gauthier, A. Antonetti, and G. Grillon, "Temporal and spatial measurements of the electron density perturbation produced in the wake of an ultrashort laser pulse," *Phys. Rev. Lett.*, vol. 76, p. 3566, 1996.

[18] C. W. Siders, S. P. L. Blanc, D. Fisher, T. Tajima, M. C. Downer, A. Babine, A. Stepanov, and A. Sergeev, "Laser wakefield excitation and measurement by femtosecond longitudinal interferometry," *Phys. Rev. Lett.*, vol. 76, p. 3570, 1996.

[19] K. Nakajima, T. Kawakubo, H. Nakanishi, A. Ogata, Y. Kato, Y. Kitagawa, R. Kodama, K. Mima, H. Shiraga, K. Suzuki, T. Zhang, Y. Sakawa, T. Shoji, Y. Nishida, N. Yugami, M. Downer, D. Fisher, B. Newberger, and T. Tajima, "A proof-of-principle experiment of laser wakefield acceleration," *Phys. Scripta*, vol. T52, p. 61, 1994.

[20] P. Sprangle, E. Esarey, J. Krall, and G. Joyce, "Propagation and guiding of intense laser pulses in plasmas," *Phys. Rev. Lett.*, vol. 69, p. 2200, 1992.

[21] N. E. Andreev, L. M. Gorbunov, V. I. Kirsanov, A. A. Pogosova, and R. R. Ramazashvili, "Resonant excitation of wakefields by a laser pulse in a plasma," *JETP Lett.*, vol. 55, p. 571, 1992.

[22] T. M. Antonsen Jr. and P. Mora, "Self-focusing and raman scattering of laser pulses in tenuous plasmas," *Phys. Rev. Lett.*, vol. 69, p. 2204, 1992.

[23] E. Esarey, J. Krall, and P. Sprangle, "Envelope analysis of intense laser pulse self-modulation in plasmas," *Phys. Rev. Lett.*, vol. 72, p. 2887, 1994.

[24] C. A. Coverdale, C. B. Darrow, C. D. Decker, W. B. Mori, K.-C. Tzeng, K. A. Marsh, C. E. Clayton, and C. Joshi, "Propagation of intense subpicosecond laser pulses through underdense plasmas," *Phys. Rev. Lett.*, vol. 74, p. 4659, 1995.

[25] D. Gordon, "Observation of electron energies beyond the linear dephasing limit from a laser-excited relativistic plasma wave," *Phys. Rev. Lett.*, vol. 80, p. 2133, 1998.

[26] A. Modena, Z. Najmudin, A. E. Dangor, C. E. Clayton, K. A. Marsh, C. Joshi, V. Malka, C. B. Darrow, C. Danson, D. Neely, and F. N. Walsh, "Electron acceleration from the breaking of relativistic plasma waves," *Nature*, vol. 377, p. 606, 1995.

[27] K. Nakajima, T. Kawakubo, H. Nakanishi, A. Ogata, Y. Kato, Y. Kitagawa, R. Kodama, K. Mima, H. Shiraga, K. Suzuki, T. Zhang, Y. Sakawa, T. Shoji, Y. Nishida, N. Yugami, M. Downer, D. Fisher, B. Newberger, and T. Tajima, "A proof-of-principle experiment of laser wakefield acceleration," *Phys. Scripta*, vol. T52, p. 61, 1994.

[28] P. Woodward, *J. IEEE*, vol. 93, p. 1554, 1947.

[29] J. D. Lawson, "Lasers and accelerators. (talk)," *IEEE Trans. Nucl. Sci.*, vol. NS-26, p. 4217, 1979.

[30] C. I. Moore, J. P. Knauer, and D. D. Meyerhofer, "Observation of the transition from thomson to compton scattering in multiphoton interactions with low-energy electrons," *Phys. Rev. Lett.*, vol. 74, p. 2439, 1995.

[31] W. L. Kruer, *The Physics of Laser-Plasma Interactions.* Reading, MA: Addison-Wesley, New York, 1988.

[32] D. Bauer, P. Mulser, and W.-H. Steeb, "Relativistic ponderomotive force, uphill acceleration, and transition to chaos," *Phys. Rev. Lett.*, vol. 75, p. 4622, 1995.

[33] B. Quesnel and P. Mora, "Theory and simulation of the interaction of ultraintense laser pulses with electrons in vacuum," *Phys. Rev. E*, vol. 58, p. 3719, 1998.

[34] C. D. Decker and W. B. Mori, "Group velocity of large amplitude electromagnetic waves in a plasma," *Phys. Rev. Lett.*, vol. 72, p. 490, 1994.

[35] C. D. Decker and W. B. Mori, "Group velocity of large amplitude electromagnetic waves in a plasma," *Phys. Rev.E*, vol. 51, p. 1364, 1995.

[36] J. F. Drake, P. K. Kaw, Y. C. Lee, G. Schmid, C. S. Liu, and M. N. Rosenbluth, "Parametric instabilities of electromagnetic waves in plasmas," *Phys. Fluids*, vol. 17, p. 778, 1974.

[37] C. E. Max, J. Arons, and A. B. Langdon, "Self-modulation and self-focusing of electromagnetic waves in plasmas," *Phys. Rev. Lett.*, vol. 33, p. 209, 1974.

[38] D. W. Forslund, J. M. Kindel, and E. L. Lindman, "Plasma simulation studies of stimulated scattering processes in laser-irradiated plasmas," *Phys. Fluids*, vol. 18, p. 1017, 1975.

[39] P. Kaw, G. Schmidt, and T. Wilcox, "Filamentation and trapping of electromagnetic radiation in plasmas," *Phys. Fluids*, vol. 16, p. 1522, 1973.

[40] C. E. Max, "Strong self-focusing due to the ponderomotive force in plasmas," *Phys. Fluids*, vol. 19, p. 74, 1976.

[41] R. Bingham and C. N. Lashmore-Davies, "Self-modulation and filamentation of electromagnetic waves in a plasma," *Nuclear Fusion*, vol. 16, p. 67, 1976.

[42] S. C. Wilks, J. M. Dawson, W. B. Mori, T. Katsouleas, and M. E. Jones, "Photon accelerator," *Phys. Rev. Lett.*, vol. 62, p. 2600, 1989.

[43] E. Esarey, A. Ting, and P. Sprangle, "Frequency shifts induced in laser pulses by plasma waves," *Phys. Rev. A*, vol. 42, p. 3526, 1990.

[44] W. B. Mori, "The physics of the nonlinear optics of plasmas at relativistic intensities," *IEEE J. Quantum Electron.*, vol. 33, p. 1942, 1997.

[45] G.-Z. Sun, E. Ott, Y. C. Lee, and P. Guzdar, "Self-focusing of short intense pulses in plasmas," *Phys. Fluids*, vol. 30, p. 526, 1987.

[46] A. B. Borisov, O. B. Shiryaev, A. McPherson, K. Boyer, and C. K. Rhodes, "Stability analysis of relativistic and charge-displacement self-channelling of intense laser pulses in underdense plasmas," *Plasma Physics and Controlled Fusion*, vol. 37, p. 569, 1995.

[47] A. B. Borisov, A. V. Borovskiy, O. B. Shiryaev, V. V. Korobkin, A. M. Prokhorov, J. C. Solem, T. S. Luk, K. Boyer, and C. K. Rhodes,"Relativistic and charge-displacement self-channeling of intense ultrashort laser pulses in plasmas," *Phys. Rev. A*, vol. 45, p. 5830, 1992.

[48] A. B. Borisov, A. V. Borovskiy, O. B. Shiryaev, V. V. Korobkin, A. M. Prokhorov, J. C. Solem, T. S. Luk, K. Boyer, and C. K. Rhodes,"Observation of relativistic and charge-displacement self-channeling of intense intense subpicosecond ultraviolet (248 nm) radiation in plasmas," *Phys. Rev. Lett.*, vol. 68, p. 2309, 1992.

[49] P. Monot, T. Auguste, P. Gibbon, F. Jacober, G. Mainfray, A. Dulieu, M. Louis-Jacquet, G. Malka, and J. L. Miquel, "Experimental demonstration of relativistic self-channeling of a multiteravatt laser pulse in an underdense plasma," *Phys. Rev. Lett.*, vol. 74, p. 2953, 1995.

[50] G. A. Askar'yan, S. V. Bulanov, F. Pegoraro, and A. M. Pukhov, "Magnetic interaction of self-focusing channels and fluxes of electromagnetic radiation: their coalescence, the accumulation of energy, and the effect of external magnetic fields on them," *JETP Lett.*, vol. 60, p. 251, 1994.

[51] A. Pukhov and J. Meyer-ter-Vehn, "Relativistic magnetic self-channeling of light in near-critical plasma: Three-dimensional particle-in-cell simulation," *Phys. Rev. Lett.*, vol. 76, p. 3975, 1996.

[52] Dattoli, G., Renieri, A., and Torre, A., 1993, "Lectures on the free electron lasers and related topics", *World Science Publisher, Sinapore*, p.289-342.

[53] Bulanov, S.V., Kirsanov, V.I., and Sakharov, A.S., 1989, *JETP Lett.* vol.50, 198.

[54] Jackson, J.D., 1975, "Classical Electrodynamics", Wiley, New York, 2nd edition, p.552

[55] Esarey, E., and Pilloff, M., 1995, Physics of Plasmas 2 (5), 1432-1436.

[56] Davidson, R., (2001). Physics of Nonneutral Plasmas. London: Imperial Colledge Press

[57] Quesnel, B., and Mora, P., (1998). Physical Review E (Statical Physics, Plasmas, Fluids, and Related Interdisciplinary Topics) 58(3), 3719-3732.

[58] Whittum, D. H. (1992). Physics of Fluids B: Plasma Physics 4 (3), 730-739.

[59] Bauer, D., Mulser, P., and Steeb, W.-H. (1995). Physical Review Letters 75 (25), 4622-4625.

[60] Kim, T.P., Fitour, R., Kim, D.E., Pukhov, A., Seredov, V., Kostyuokov, I., Tafzi, A., Garl, T., Artemiev, N., Shah, A., Felicie, A., Boschetto, D., and Rousse, A., 2007, sent to PRL.

[61] Nisoli, M., De Silvestri, S., and Svelto, O., Opt. Lett. 22, 522 (1997)

[62] Wang, Z., Zhang, Z., Xu, Z.,and Lin, Q.,IEEE J. Quantum Electron. 33, 566 (1997)

[63] Wang, Z., Xu, Z., and Zhang, Z., Q.,Opt. Lett. 22, 354 (1997)

[64] Marathay, A. S., Appl. Opt. 33, 3139 (1994)

[65] Ziolkowsky, R. W., and Judkins, J. P., J. Opt. Soc. Am. A 9, 2021 (1992)

[66] Belenov, E. M., and Nazarkin A. V., Pis'ma Zh. Eksp. Teor. Fiz. 53, 188 (1991) [JETP Lett. 53, 200 (1991)]

[67] Christof, I. P., Opt. Commun. 53, 364 (1985)

[68] Shvartsburg, A. B., "Time-Domain Optics of Ultrashort Waveforms"(Oxford University Press, Oxford 1996)

[69] Akhmanov, S. A., Vysloukh V. A., and Chirkin, A. S., "Optics of Femtosecond Laser Pulses" (AIP, New York, 1992)

Acknowledgements

I would like to thank in first place my supervisor Prof. Dr. Alexander Pukhov, who supported and advised me during this scientific work. This work would be impossible without his help and very wide knowledge in physics and computational methods.

I thank Dr. Serguei Gordienko for help in theoretical techniques. His advices in choice of mathematical methods and his comments were very useful for me. I thank Dr. Igor Kostyukov, whose erudition in plasma physics helps me so much. A large part of my work during PhD-study has be done in collaboration with Prof. Dr. Alexander Pukhov, Dr. S. Gordienko and Dr. I. Kostyukov.

I am grateful to Prof. Dr. Georg Pretzler for providing support to my work during last three years.

My special thanks Serguei Kiselev for help with programming techniques and software.

I would like to thank my colleagues from the Institut für Theoretische Physik I of Duesseldorf University: Akad. Direktor Dr. Herbert Wenk for help with computer network, Eckhard Zügge for technical support and help with hardware problems, Elvira Gröters for help with organizational problems, Dr. Ernst Wolfgang Laedke, Dr. Jan Alexander Posth, Dr. Sylvie Rijkers Defrasne, Dr. Christoph Karle, Anuman Karmakar, Götz Lehmann, Marcus Neuer, Teodora Baeva for interesting discussions and friendly work atmosphere.

Erklärung

Mit meiner Unterschrift versichere ich an Eidesstatt, dass ich die vorgelegte Dissertation selbst und ohne unerlaubte Hilfe angefertigt habe und dass ich diese in der jetzigen oder einer ähnlichen Form noch keiner anderen Fakultät eingereicht habe.
Ich erkläre ferner, dass die Dissertation noch nicht veröffentlicht wurde (Veröffentlichungen nach §4(3) der Promotionsordnung bleiben hiervon ausgenommen).

Die Promotionsordnung ist mir bekannt.

Düsseldorf, im May 2008